DYNAMICS OF LOCALIZED STRUCTURES IN SPATIALLY EXTENDED AND COUPLED SYSTEMS WITH DELAYED FEEDBACK

DISSERTATION

ZUR ERLANGUNG DES AKADEMISCHEN GRADES
DOCTOR RERUM NATURALIUM
(DR. RER. NAT.)

IM FACH MATHEMATIK

EINGEREICHT AN DER MATHEMATISCH-NATURWISSENSCHAFTLICHEN FAKULTÄT DER
HUMBOLDT-UNIVERSITÄT ZU BERLIN

VON
MAGISTER FÜR ANGEWANDTE MATHEMATIK UND PHYSIK

DMITRY PUZYREV

PRÄSIDENTIN DER HUMBOLDT-UNIVERSITÄT ZU BERLIN
PROF. DR.-ING. DR. SABINE KUNST

DEKAN DER MATHEMATISCH-NATURWISSENSCHAFTLICHEN FAKULTÄT
PROF. DR. ELMAR KULKE

GUTACHTER/INNEN:

1. PROF. DR. ALEXANDER MIELKE
2. PD DR. SVETLANA GUREVICH
3. PROF. DR. SERHIY YANCHUK

TAG DER MÜNDLICHEN PRÜFUNG: 11.07.2018

Acknowledgements

To my grandfather,
Prof. N.B. Kolokolov

This Thesis was completed in the Junior Research group "Applied Analysis" in Humboldt University and under the Collaborative Research Center (SFB) 910, Project A3 in Weierstrass Institute for Applied Analysis and Stochastics and Technical University of Berlin.

I would like to thank first and foremost my scientific advisers Prof. Dr. Serhiy Yanchuk, Dr. Sc. Andrei Vladimirov; collaborators in research (Dr. Svetlana Gurevich, Dr. Alexander Pimenov, Dr. Mustapha Tlidi, Prof. Dr. Krassimir Panajotov) and development (Dr. Leonhardt Luecken and Marcus Kantner).

I would like to thank all members of the work groups in Humboldt University of Berlin, Weierstrass Institute, Technical University of Berlin; especially Stefan Ruschel, Dr. Jan-Philipp Pade and Dr. Shalva Amiranashvili for special support; all members of SFB 910 and especially Project Group A3: Dr. Matthias Wolfrum and Sebastian Eydam.

I want to thank my colleagues and friends Dr. Ivan Yamschikov, Dr. Dmitry Zhelezov, Dr. Nikita Begun; cities of Berlin, Prague and St. Petersburg; I cannot emphasize enough how thankful I am to my great family.

The work would not be possible without the financial support by Erasmus-Mundus TRIPLE I program and German Research Foundation (DFG) in the framework of the Collaborative Research Center 910.

A special dedication to S.T., the funniest person I ever knew.

Finally, I would like to thank every reader and reviewer of this work!

Thank you!

Abstract

Systems with time-delay are ubiquitous in nature and attract significant interest in the field of nonlinear dynamics. Addition of the delayed feedback to spatially extended nonlinear systems or inclusion of coupling of the delay systems give birth to rich and intriguing dynamical phenomena, when various solutions can be modified or controlled with the change of the feedback or coupling parameters. The scope of this Thesis is the spatiotemporal dynamics in spatially extended nonlinear systems with time-delay, with a focus on the dynamics of localized structures. The systems under consideration are described by partial differential equations with delayed feedback and coupled systems of delay differential equations.

For the partial differential equations, the existence and stability of plane wave solutions as well as localized structures are investigated in one-dimensional complex cubic and cubic-quintic Ginzburg-Landau equation with delayed feedback. The choice of Ginzburg-Landau equation is motivated by its role as an amplitude equation in spatially extended systems. The first result of this Thesis is the complete description of the set of plane wave solutions and their stability in the limit of large delay time. Due to the symmetry of Ginzburg-Landau equation, this set forms a one-dimensional family which leads to the appearance of the "tube" in parameter coordinates which is filled densely with plane wave solutions with the increase of the delay time. The same description is applied to the case of localized structures in the broad-area laser with a saturable absorber.

The second novel result is the description of modulational instability of localized structures in spatially extended systems with time-delay which can lead to periodic and chaotic zigzagging movement of the solution.

The third result is the description of bound pulse trains in coupled delay systems depicting an array of mode-locked lasers. In this regime mode-locked pulses in different lasers interact locally via the balance of their repulsion and attraction. As a result, clusters of pulses emerge which can not exist in a solitary mode-locked laser. All of the aforementioned phenomena were described analytically and the results are supported by path continuation methods as well as direct numerical simulations with a specially designed software tool.

Zusammenfassung

Systeme mit Zeitverzögerung sind von großem Interesse in Nichtlinearer Dynamik und allgegenwärtig in den Naturwissenschaften. In räumlich ausgedehnten Systemen führt die zeitverzögerte Rückkopplung zu vielfältigen dynamischen Phänomenen, die durch Variieren der dem System inherenten Parameter kontrollierbar werden. Gegenstand dieser Doktorarbeit ist die raumzeitliche Dynamik räumlich-ausgedehnter, nichtlinearer Systeme mit Zeitverzögerung, mit besonderem Augenmerk auf deren lokalisierte Lösungen. Die betrachteten Systeme werden beschrieben durch partielle Differentialgleichungen mit verzögerter Rückkopplung und gekoppelte Systeme von gewöhnlichen Differentialgleichungen mit verzögerter Rückkopplung.

Hinsichtlich der partiellen Differentialgleichungen untersucht diese Arbeit die Existenz und Stabilität der ebenen Wellenlösungen ebenso, wie die Existenz und Stabilität der lokalisierten Lösungen der eindimensionalen, komplexen, kubischen und kubisch-quintischen Ginzburg-Landau Gleichung mit verzögerter, optischer Rückkopplung. Die Ginzburg-Landau Gleichung ist prototypisch für oszillatorische Destabilisierungen nahe einer Hopf Bifurkation in räumlich ausgedehnten Systemen und beschreibt die Zeitevolution der Amplitude nahe der Destabilisierung. Das erste Ergebnis dieser Arbeit ist die vollständige Beschreibung der Menge der ebenen Wellenlösungen und ihre Stabilität für lange Verzögerungszeiten. Aufgrund der Symmetrie der Ginzburg-Landau Gleichung bildet diese Menge eine eindimensionale Familie, die zum Auftreten einer „Tube“ in Parameter-Koordinaten führt. Diese “Tube” wird unter Verlängerung der Verzögerungszeit dicht mit ebenen Wellenlösungen gefüllt. Eine analoge „Tube“ erscheint im Fall der lokalisierten Lösungen eines Breitbandlasers mit saturierendem Absorber.

Das zweite, neuartige Ergebnis ist die Beschreibung der Modulationsinstabilität dieser lokalisierten Strukturen. Diese Instabilität kann zu einer periodischen und chaotischen Zickzackbewegung der Lösung führen.

Das dritte Resultat ist die Charakterisierung gebundener Impulsfolgen in einem System von gekoppelten gewöhnlichen Differentialgleichungen mit Zeitverzögerung, das zur Beschreibung einer Anordnung von modengekoppelten Lasers herangezogen wird. In diesem Regime interagieren die modengekoppelten Impulse in verschiedenen Lasern lokal über die Balance von Abstoßung und Anziehung. Resultierend daraus entstehen Cluster von Impulsen, die in einzelnen modengekoppelten Lasern nicht möglich sind. Sämtliche genannte Phänomene wurden analytisch und numerisch behandelt. Die Ergebnisse werden durch Fortsetzungsmethoden sowie durch direkte numerische Simulationen mit einem speziell entwickelten Softwaretool gestützt.

Contents

CHAPTER 1

Introduction

The opening Chapter outlines the scope and motivation of this Thesis. First, a brief overview of spatially extended and coupled systems which are considered in this work is given. The systems with delay are introduced. The physical aspects of systems of interest as well as the way they are described from the mathematical point of view are discussed. Then, we pose the specific problems and questions which are addressed in this work and linked to respective main Chapters of the Thesis. The choice of general scientific approach to the problem of the Thesis is briefly discussed as well. In the end of the Introduction chapter, the short guide to the structure of the Thesis is given.

1.1. Overview of spatially extended and coupled systems with delay

The last century in mathematics and physics truly marks the onset of study and understanding of nonlinear systems, which, as we understand now, encompass mostly everything which exists in the Universe [1]. For historical reasons, the initial subject of interests naturally approached by nonlinear science is the complex behavior of nonlinear systems in time. The educational courses and textbooks of nonlinear dynamics always begin and are quite often limited to the study of temporal behavior of various systems. We are surrounded, however, by a great vastness of self-organized *spatiotemporal* patterns, strikingly varied but at the same time resembling each other across different types of systems, from star constellations to vegetation patterns to human brain [1, 2, 3]. They are either already fixed as a result of development or appearing in an ongoing process of evolution in time and space. The common point of the self-organized structures and patterns is that they are born in the systems outside of thermodynamic equilibrium, which are also called dissipative systems. When the time evolution is amplified by another variable in some form, be it either spatial distribution or coupling of many systems in one, the nonlinear system gives birth to the full richness of dynamical regimes.

The study of pattern formation in spatially extended systems outside of equilibrium dates back to the classical works of Turing [4] and Prigogine and Lefever [5]. A multitude of solutions can be present in spatially extended dissipative systems: from homogeneous steady states, hexagon and stripe patterns, to localized structures, spirals, targets and various types of spatiotemporal chaos, rogue waves, etc. It was observed that many spatially extended systems of different origin possess the similar structures and patterns. This implies the existence of some universal

laws and led to the creation of several established models to describe the pattern formation outside of equilibrium.

From the mathematical point of view, nonlinear partial differential equations (PDEs) [6, 7, 8, 9] are used to simulate the behavior of spatially extended systems outside of equilibrium. Their independent variables are time t and one or more dimensional variable x, which usually represents position in space but may also represent relative DNA content, size of cells, or their maturation level, or other values. The solutions (dependent variables) of partial differential equations may represent electric field, temperature, voltage, or concentrations or densities of various particles, for example cells, bacteria, chemicals, animals.

One of the important phenomena which appear in extended systems is the existence of localized structures (LS). The localization in nonlinear systems in form of solitary wave (soliton) was first observed by Russell in 1834-1844 [10] and then explained by derivation of Korteweg-de Vries (KdV) equation [11] and its solutions. Since then, great amount of investigations of nonlinear phenomena are associated with study of localized solutions: bounding and clustering of solitons, interaction with solitons with each other and with different types of solutions, and so on.

In spatially extended dissipative systems, self-organized localized solitary patterns have been found in very different areas of research and turned out to be of particular interest for fundamental studies as well as for applications (see, e.g., [12, 13, 14, 15] and references thereafter). While in the Hamiltonian systems the origin of solitons lies in the balance between the dispersion (or diffraction) and nonlinearity, in the dissipative systems localized structures should satisfy the balance between energy dissipation and gain in the first place. In spatially extended dissipative systems, they are often referred to as dissipative solitons [12, 13, 14, 15]; other frequently used terminology includes autosolitons [16], oscillons [17], as well as spots, pulses, and spikes [18]. The localization can be temporal as well, in this case the localized structures are usually observed as short pulses [19].

Another class of systems that allows to obtain different types of dynamical regimes are *coupled dynamical systems*. Important property of coupled systems is possibility of the synchronization, i.e. adjustment of rhythms of self-sustained periodic oscillators due to their interaction. The effect of synchronization of coupled systems was discovered first by Huygens back in year 1693 [20] and explained in the beginning of 20th century (for the ongoing work on the investigation of the original Huygens experiments, see, e.g [21, 22]). Since then, a great amount of work was invested in study of synchronization in the systems of coupled nonlinear oscillators [23]. Along with the fully synchronized solutions and semi-synchronized solutions, splay-states of different kinds, chimera states with coexistence of coherence and incoherence [24, 25] can exist. While spatially extended systems are described by PDEs, the coupled systems are usually described by high-dimensional systems of ordinary differential equations (ODEs). There is a strong connection

between the aforementioned types of dynamical systems: spatially extended systems frequently are the continuous limit case of the coupled systems, and many coupled systems are the discretized versions of continuous systems.

In addition to space distribution, many physical systems possess another important feature: the current state of the system can depend on what happened to the system at an earlier time. Such systems are called the delay systems. The interest in the delay systems started more than two centuries ago (see the overview [26] dating back to 1911) and gained much momentum and spread to the multitude of topics in the middle of the 20th century [27] after considerable improvement of engineering and control systems as well as a mathematical base for the theoretical treatment of delay equations [28, 29].

In many physical systems, delay appears naturally, and in other systems, delay feedback control can be artificially introduced in order to change the dynamical properties of the system [30]. The essential feature of delay systems is that the inclusion of a single retarded variable in the system can greatly sophisticate its dynamical behavior by making it infinite dimensional. It should be noted, that sometimes the spatially extended systems described by PDEs are reformulated as the delay dynamical systems [31, 32, 33], as well as in the opposite way. In many cases, however, both spatial coordinates and the delay are present in the system.

Due to its significant influence on the dynamics of the system, the introduction of delayed variables has gathered a large amount of attention [29, 34, 35, 36, 37]. Delay differential equations are used to describe dynamics of systems of various origin, from nuclear reactors [38], to lasers [39, 40] and population dynamics [41]. The models which introduce delay to neural dynamics are being developed [39, 42]. Delay is also introduced to the economical models, e.g. to Black-Scholes formula for options pricing [43]. One of developing areas which benefits of the delay is reservoir computing, see [44, 45], where it is demonstrated that a single nonlinear node with delayed feedback can perform efficient information processing.

It was already mentioned that inclusion of the delay can be used to control the dynamics in nonlinear systems. Time delayed feedback control has been originally used for the systems with few degrees of freedom [46, 47, 48, 49, 50], but has proved to be effective in spatially extended systems as well. Delayed feedback serves as one of efficient control methods, allowing to stabilize or switch spatiotemporal regimes [51, 52]. The particular type of control, namely noninvasive Pyragas control [53] (also known as time-delay autosynchronization) was successfully applied both theoretically and experimentally in [54, 52]. Aside from stabilization of the solutions, the inclusion of delayed feedback can lead to the appearance of new regimes, e.g. generate rogue waves or extreme events in the form of giant pulses [55]. In coupled systems, interplay of delayed feedback and coupling leads to switching of the dynamical regimes and appearance of new patterns [51, 56, 57]. Influence of delayed feedback on the chimera states of coupled systems was investigated in, e.g. [58, 59]. Up to now, the influence of delayed

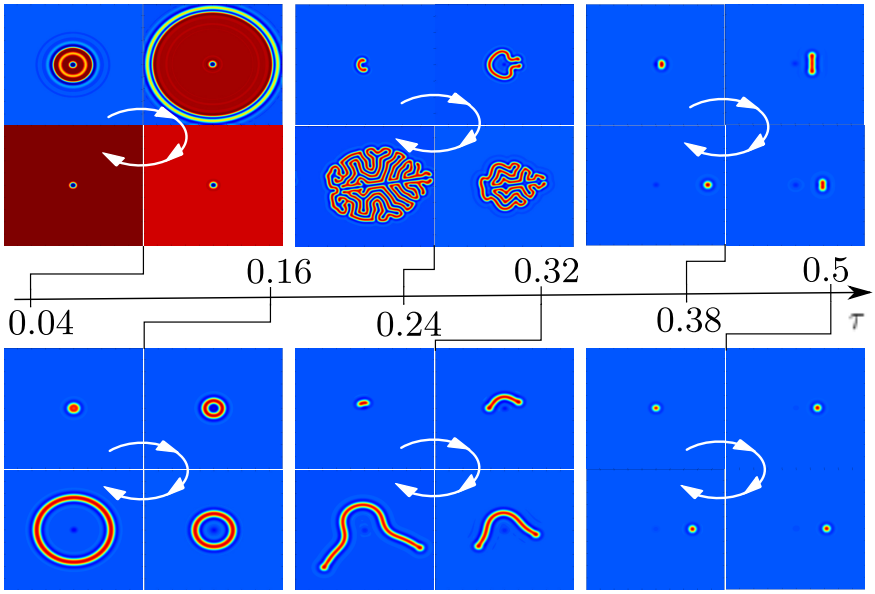

FIGURE 1.1.1. Numerical solutions of delayed Swift-Hohenberg equation, obtained for fixed product of feedback strength and delay time and different values of the delay time τ. White arrows indicate the time evolution direction. Taken from [60] with permission of the author.

feedback on the dynamics of complex spatially extended and coupled systems has not been understood to a large degree.

The intriguingly complex spatiotemporal behavior appearing in the spatially extended systems with feedback can be illustrated by the example shown in Fig. 1.1.1, taken from [60] with kind permission of the author. It shows different solutions of delayed Swift-Hohenberg equation, obtained numerically for the fixed product of feedback strength and delay time and different values of the delay time τ. White arrows indicate the time evolution direction. Here, varying the delay time τ allows for the appearance of solutions of increasingly complex structure. For a small delay (see Fig. 1.1.1 for $\tau = 0.04$) a stationary bright LS transforms into a breathing dark LS. If τ is increased, a soliton ring ($\tau = 0.16$) or a labyrinth ($\tau = 0.24$) is formed. With further increase in τ, a moving wave segment emerges. Finally, a motion with a constant velocity is observed as shown in Fig. 1.1.1 for $\tau = 0.5$. In short, such complicated dynamics appear due to the combinations of destabilization of different internal modes of solutions due to the delayed feedback. The focus of this Thesis lies in the understanding of how the *interplay of the spatial distribution and delay* affects the dynamical properties of the systems, altering the existing solutions and their stability and bifurcation properties. The particular emphasis is paid to the dynamics of the aforementioned localized structures.

The particular area of investigation of this Thesis is the delay-induced dynamics in the optical systems. Out of many types of dynamical systems, the optical

systems are a natural example of the case where the coupling (optical routing of light) and delayed feedback (the simplest example of which is the common mirror) can be implemented elegantly. The optical systems, in particular the lasers of different types, since their creation have served as the sandbox for the study of nonlinear phenomena [61], given the multitude of dynamical regimes available in them. The intrinsic time scales of laser systems are exceptionally small, giving the opportunity to quickly gather experimental data on the dynamics of the system, separating stable regimes from transitional states. The coupling and the delay can be realized in lasers in an efficient way. The broad-area lasers, also known as vertical cavity surface emitting lasers (VCSELs), also give the possibility to add a transverse spatial coordinate to the system, giving birth to aforementioned localized structures [62, 63].

The scope of this work is to study how the combination and interplay of the delay and spatial distribution affects the dynamics of two types of dynamical systems: *1.) Spatially extended systems with delayed feedback* and *2.) Coupled pulse generators*. The theoretical aspects which are essential to investigate the aforementioned systems are discussed in **Chapter 2** of the Thesis. The first type of the *spatially extended optical system* in the form of broad-area laser with delayed feedback is addressed in **Chapters 3** and **4** of the Thesis. The second type of coupled pulse generators is represented in **Chapter 5** of the Thesis by the array of mode-locked lasers.

Speaking from the mathematical point of view, in **Chapters 3** and **4** of this thesis, the systems of our interest are described by delay partial differential equations (DPDE). DPDE is a partial differential equation in which the behavior of the system depends not only on the solution at a present time but also on the solution at some past time. The overview of application of DPDEs to the modelling of systems of various origin, including the population ecology, gene repression, control theory etc., is given in, e.g., [64].

Since delay partial differential equations operate in the space of the unknown functions on some time interval, they are a part of a wider class of functional partial differential equations (FPDEs). The book [64] gives extensive insight into theoretical aspects for functional partial differential equations.

In **Chapter 5** of the Thesis, the model equations are the system of coupled delay differential equations (DDEs), which in turn belong to the wider class of functional differential equations. The overview on the theory of bifurcations in functional differential equations is given in, e.g., [34, 65].

A special focus of this Thesis is the complex Ginzburg-Landau equation (CGLE), which is universal for many types of dynamical systems since it is a normal form of solution near the onset of Andronov-Hopf bifurcation. In other words, in this case it serves as an amplitude equation [66, 67]. The role of complex Ginzburg-Landau equation as an amplitude equation was extensively described in the work [67]. In the Thesis, we have investigated a more classical case of the cubic CGLE as well as a specific cubic-quintic CGLE, where the quintic term is introduced to allow for the existence of stable localized solutions [68].

This Thesis also deals with the problem of numerical treatment of the complex systems with delay. **Appendix A** of the Thesis contains the description of the package ODDTool that was developed for the simulation of spatially extended and coupled systems with delay. From the numerical point of view, the treatment of DPDEs and systems of coupled DDEs is directly connected due to the process of space discretization which is necessary for the simulation of DPDEs. Indeed, after the discretization of the spatial variable or the application of discrete Fourier transform, DPDE is represented as a large system of DDEs and the simulation of such system is similar to that of many coupled ODEs with delay. The package which was developed and used for the numerical computations in this Thesis can be applied to the simulation of the delay PDEs systems as well as coupled DDEs, including the cases of large delay times.

1.2. Problem statement and approach

Summing up the overview given in the previous section, one can get an impression of the abundance of open questions in physical, mathematical and numerical treatment of extended and coupled systems with time-delays. The delayed feedback can have an ambivalent impact on those systems, stabilizing, destabilizing and switching various patterns and dynamical regimes, and while some of the phenomena are already described in a general way, there are numerous open paths to follow. This Thesis is focused on the dynamics of particular localized states of extended and coupled dynamical systems with delay and the following questions and problems are posed:

- **Chapters 3** and **4** of the Thesis are devoted to the study of spatially extended dynamical systems of Ginzburg-Landau type with delayed feedback, with a particular emphasis on the dynamics of localized structures. Here, the following questions are asked and answered: *How does the addition of delayed feedback alter the existing solutions in the system? Does the delayed feedback with the various strength and phase lead to the change of the existing solutions or appearance of new solutions via some previously undescribed bifurcations? What happens in the limit of a large feedback time?*
- In **Chapter 5** of the Thesis, the dynamical regimes in the system of coupled pulse oscillators in the form of a ring of the mode-locked lasers are investigated. Here, the interplay between the delay-induced dynamics in each solitary laser and coupling of the lasers is responsible for the emergence of bound pulse trains as well as various synchronized regimes. This part of the Thesis is aimed at answering the question: *How is the strength and phase of coupling between pulse oscillators responsible for the creation and bifurcations of synchronized and asynchronous dynamical regimes?*

The important methodological feature of this work is the combination of state-of-the-art methods available to the nonlinear science, particularly in the fields of pattern formation and delay equations. Over the course of the Thesis, both

analytical methods (such as multiscale analysis and bifurcation theory) and numerical approaches (direct simulation as well as path continuation) are used to thoroughly study the delay and delay-free equations of interest.

The nature of the problems itself demands the relatively high computational power (as the inclusion of the delay into the system adds numerical complexity); however, they pose theoretical challenges as well. This could sound counter-intuitive, given the fact that the investigated equations usually do not have analytical closed representation of the solutions of interest (e.g. the stable localized structures). Naturally, for the problems addressed in this Thesis, the use of numerical methods cannot be avoided at some point. For each problem, the Thesis contains derived analytical expressions in form of some combinations of original equation coefficients and scalar products of eigenfunctions which should be calculated numerically. The analytical approaches provide the following advantages: a.) They give the possibility to understand the underlying mechanisms of dynamical behavior, b.) Drastically reduce the computational time by predicting the parameter values for bifurcation thresholds etc., c.) Give the insight into the possible application of the equations and methods to other types of physical systems which demonstrate the similar dynamical behavior. Application of bifurcation theory supported by the numerical path continuation methods allows to predict the emergence of the solutions with certain properties. The analytical treatment of each problem in this Thesis is followed by a numerical simulation of the systems to validate and illustrate the described phenomena.

1.3. A short guide to the thesis

This Thesis is organized as follows:

- After the **Introduction,** the essential mathematical definitions and theorems are given in **Chapter 2**.
- **Chapter 3** of the Thesis contains the investigation of the existence and stability of plane wave solutions in cubic and cubic-quintic complex Ginzburg-Landau equation.
- **Chapter 4** is dedicated to the study of stability and bifurcations of localized solutions in laser with saturable absorber. Newly found results on the delay-induced instability are also extended for a localized solutions in Lugiato-Lefever equation as well as complex cubic-quintic Ginzburg-Landau equation.
- **Chapter 5** of the Thesis contains the study of synchronized solutions and newly discovered bound pulse train regimes in the system of coupled mode-locked lasers.
- The **Summary and Outlook** of this work are given in the final **Chapter 6** of the Thesis.
- The **Appendix A** describes the openly accessible package ODDTool for simulation of ODEs and PDEs with large delay which was developed, in particular, for the purpose of this work. The **Appendix B** contains some additional theorems used in the Thesis.

CHAPTER 2

Elements of theory

This preliminary chapter will introduce some elements of theory of delay differential equations, especially for the delay PDEs which are relatively modern and less widespread in the literature. In the main Chapters of the Thesis which follow, the approach is significantly more applied. However, the results are based on the application of several fundamental results which are formulated in this Chapter. The following theoretical aspects are of particular importance for this Thesis:

- The results for the existence, uniqueness and linearized stability principle of the solutions of the delay partial differential equations.
- The large delay approximation which is instrumental for the first two main chapters of the Thesis.
- The Fredholm alternative and bilinear form for delay partial differential equations.

2.1. Delay partial differential equations and their stability

2.1.1. Delay partial differential equations: existence and uniqueness of solution

In the course of the Thesis we are generally investigating the systems which are described by delay partial differential equations in the form

$$\begin{cases} \frac{\partial u}{\partial t}(x,t) = (d+i)\Delta u(x,t) + f\left(u(x,t), u(x,t-\tau)\right), t > 0, x \in \Omega \\ u(x,t) = 0 \text{ or } \frac{\partial u}{\partial n}(x,t) = 0, t > 0, x \in \partial\Omega \\ u(x,t) = \phi(x,t), t = [-\tau, 0], x \in \Omega \end{cases} \tag{2.1.1}$$

where $u(x,t)$ is a complex-valued function, τ is a given constant delay time, Δ is Laplacian operator, d is non-negative diffusion coefficient, i is an imaginary unit, nonlinearity f is continuously differentiable, and Ω is a bounded domain in $\mathbb{R}^N$ with a smooth boundary $\partial\Omega$ ($\frac{\partial}{\partial n}$ denotes the differentiation in the direction of the outward normal).

More precisely, this Thesis is focussed on one-dimensional spatially extended systems with a single space variable x. Note that in numerical computations for the plane wave solutions of CGLE in Chapter 3, the periodic boundary conditions are used:

$$\left[u(\Gamma_1,t) = u(\Gamma_2,t), \frac{\partial u}{\partial x}(\Gamma_1,t) = \frac{\partial u}{\partial x}(\Gamma_2,t)\right].$$

For the localized solutions on zero background which are investigated in Chapter 4, the computations with different boundary conditions were performed yielding similar results for sufficiently large intervals in x.

Note that system (2.1.1) is equivalent to two coupled real-valued reaction-diffusion type equations with delay. Here, the results on existence and uniqueness for such systems are provided. The full theory is extensively formulated in [64] following [69] and other works on the theory of functional PDEs.

The approach used for the proof of the existence and uniqueness is to reformulate the problem (2.1.1) as a member of wider class of semilinear abstract functional differential equations. Let X be a Banach space over the field $\mathbb{R}$ or $\mathbb{C}$ and $C = C([-\tau, 0]; X)$ denote the Banach space of continuous X-valued functions with the supremum norm $\|\cdot\|$. The essential step in reformulating the equation (2.1.1) is to introduce $u_t(s) = u(x, t + s), -\tau \leq s \leq 0$. Then, u_t is an element of function space $C([-\tau, 0]; X)$. One can look at u_t as a segment of u on the interval $[t-\tau, t]$ translated back to the initial interval $[-\tau, 0]$.

Then Eq. (2.1.1) can be rewritten in a more general form as an abstract semilinear functional differential equation

$$\begin{cases} \dot{u}(t) = Lu(t) + F\left(u_t\right), t > 0, x \in \Omega \\ u_0 = \phi \in C, \end{cases} \tag{2.1.2}$$

where the linear operator L is a closure of L_0 in $C(\bar{\Omega})$, which is defined by

$$L_0 y = (d + i)\Delta y,$$

$$y \in \mathrm{Dom}(L_0) = \left\{ y \in C^1\left(\bar{\Omega}\right) \cap C^2\left(\Omega\right); y = 0 \text{ or } \frac{\partial y}{\partial n} = 0 \text{ on } \partial\Omega \right\}.$$

Here, we assume the following conditions:

C1 Let $\{T(t)\}_{t\geq 0}$ be the analytic compact semigroup generated by L (i.e. $Lu = \lim\limits_{x\to 0+}[T(t)u - u]/t$). Analytic semigroups are a particular kind of strongly continuous semigroups. The concept of strongly continuous semigroups can be seen as a generalization of exponential function in Banach spaces, cf. $T(t) = e^{At} := \sum_{k=0}^{\infty} \frac{A^k}{k!} t^k$ for any bounded linear operator A.

C2 Let us introduce $F(\phi)(x) := f(x, \phi(x, \cdot))$ and assume F and its derivatives with respect to ϕ and t be globally Lipschitz continuous.

One can now look at the abstract integral equation and relate its solution to the solution of the functional differential equation (2.1.2).

THEOREM 1. *(Existence and uniqueness.) Assume that conditions **C1** and **C2** hold. Then, for a given $\phi \in C$, there exists a unique function u which solves the*

initial value problem for the abstract integral equation

$$\begin{cases} u(t) = T(t)\phi(\cdot,0) + \int_0^t T(t-s)F\left(u_s\right) ds, t \geq 0 \\ u_0 = \phi \end{cases} \tag{2.1.3}$$

The solution u depends continuously on the initial function ϕ.
Under the additional assumptions on the initial function ϕ that $\phi(0) \in \mathrm{Dom}(L)$, $\dot{\phi} \in C$ and $\dot{\phi}(0^-) = L\phi(0) + F\left(0, \phi\right)$, the solution $u : [0, \infty] \to X$ of integral equation (2.1.3) is continuously differentiable and satisfies the differential equation (2.1.2).

The full proof of Theorem 1 for the given assumptions **C1** and **C2** on L and f is provided in [64] following the fundamental results from [70, 71]. The global Lipschitz continuity condition **C2** can be relaxed in the case when L generates a compact semigroup and F is completely continuous, which is satisfied for the Ginzburg-Landau type delay PDEs which are under consideration in this Thesis. Moreover, the equations under consideration guarantee the existence of global solutions, i.e. solutions which are defined for all $t \geq -\tau$. Note, that there are results on the existence and uniqueness of solution for various other combinations of assumptions on L and f which are discussed in, e.g., [72].

Remark 2. The solution of (2.1.3) is called *mild* solution of (2.1.1) [73]. It should be noted that in principle the integrated problem (2.1.3) is more general than differential equation (2.1.1) and In some cases, system (2.1.3) allows for existence of solution which can be non-differentiable [73, 64] or not belong to $\mathrm{Dom}(L)$ and coincide with the classical solution of (2.1.1) only locally on some time interval.

2.1.2. Principle of linearized stability

While the existence and uniqueness theorems provide us with the theoretical basis to search for the solutions, another important task is the analysis of the stability of the discovered solutions. The stable solutions are often of special interest as they correspond to desirable stable regimes of operation in e.g. lasers.

To find the stability properties of some solution in nonlinear equation, one can use the principle of linearized stability:

Theorem 3. *(Linearized stability.) Let solution $\hat{u}$ be an equilibrium of the abstract nonlinear functional differential equation*

$$\dot{u}(t) = Lu(t) + F\left(u_t\right)$$

*with the same assumptions **C1** and **C2** on L and F as in Theorem 1. We further assume that there exists $\delta > 0$ such that $F : B_\delta\left(\hat{u}\right) \to X$ has Fréchet derivative at $\hat{u}$ defined by $DF(\hat{u}) = \int_{-\tau}^{0} d\eta(\theta)\phi(\theta)$, $\phi \in C$ for $\eta : [-\tau, 0] \to B(X, X)$ of bounded variation and Fréchet derivative is locally Lipschitz continuous, where $B_\delta\left(\hat{u}\right) = \{\phi \in C; \|\phi - \hat{u}\| < \delta\}$.*
Then, if all $\lambda \in \mathbb{C}$ for which exists $y \in \mathrm{Dom}\left(L\right) \setminus \{0\}$ such that

$$\chi(\lambda)y = Ly - \lambda y + DF(\hat{u})\left(e^{\lambda \cdot} y\right) = 0 \tag{2.1.4}$$

have non-positive real part $\operatorname{Re}\lambda \leq 0$*, the equilibrium* $\hat{u}$ *is locally exponentially stable. In the opposite case, if there exists at least one* λ *with positive real part,* $\hat{u}$ *is unstable. Here,* $\left(e^{\lambda \cdot} y\right)(\theta) = e^{\lambda\theta}, \theta \in [-\tau, 0]$*. Equation (2.1.4) is called a characteristic equation, all* λ *are called its eigenvalues and* y *the corresponding eigenfunctions. The geometric multiplicity of a given eigenvalue* λ *is given by* $\dim \operatorname{Ker} \chi(\lambda) y$*.*

In the case of single fixed delay τ, the characteristic equation (2.1.4) takes a form of transcendental eigenvalue problem

$$\chi(\lambda)y := -\lambda y + Ay + Be^{-\lambda\tau}y = 0, \tag{2.1.5}$$

where A and B are the linearizations of the instantaneous and delayed parts of dynamics correspondingly. The investigation of characteristic equation (2.1.5) will be an instrumental tool for identifying the stability of solutions of interest over the course of the Thesis.

Remark 4. Chapter 5 of the Thesis deals with the systems described by the coupled systems of ODEs with delay, which are a subclass of functional differential equations. Naturally, the theorems for the existence, uniqueness and stability of the solutions in this case are formulated in similar way as in the case of delay PDEs. The theoretical backgrounds for the delay ODEs are significantly more widespread in the literature than those for delay PDEs and are provided in, e.g., [34, 65].

2.2. Large delay approximation

As demonstrated in [64, 74, 75], the fundamental results on existence, uniqueness and stability properties of the solutions given can be extended to equations with the infinite delay. This limit case is important in this Thesis, since it allows the so-called *large delay approximation* to be used to calculate the approximate spectrum of delay differential equation for large values of delay. The interest in large delay is motivated by the fact that in optical systems of my interest delay time can greatly exceed the internal time scales. The method was first developed for the systems of delay ODEs. The precise formulation of this method and the proofs are given in [76, 77, 78]. In what follows, the essentials of the method which are instrumental to the problems of this Thesis are presented.

To find out if some solution u of nonlinear DDE is stable, one can apply the principle of the linearized stability. Let us write down the linearized delay differential equation in form:

$$\dot{u}(t) = A(t)u(t) + B(t)u(t-\tau), u \in \mathbb{R}^N, \tag{2.2.1}$$

where matrices $A(t)$ and $B(t)$ should be considered as the Jacobians with respect to the instantaneous and the delayed variables for a given stationary, periodic, or chaotic solution $\hat{u}$ of a nonlinear DDE.

For a stationary solution $\hat{u}$, the stability is then defined by characteristic equation, which reads

$$h(\lambda, e^{-\lambda\tau}) := \det(-\lambda I + A + Be^{-\lambda\tau}) = 0. \tag{2.2.2}$$

It was proven in [78, 79], that the solutions λ of characteristic equation in the limit of large delay $\tau \to \infty$ split into two sets with different scaling properties:

DEFINITION 5. (Instantaneous and strongly unstable spectrum) The *instantaneous spectrum* is the set $\Sigma_{\mathcal{A}} = \{\lambda \in \mathbb{C}, h(\lambda, 0) = 0\}$.

In other words, $\Sigma_{\mathcal{A}}$ coincides with the spectrum of the instantaneous part of the equation, i.e., the equation (2.2.1) without delayed feedback $dx/dt = Ax$, and satisfies

$$\det(A\text{-}\lambda I) = 0. \tag{2.2.3}$$

The subset $\mathcal{A}_+ = \{\lambda \in \Sigma_{\mathcal{A}}, Re(\lambda) > 0\}$ is called the *strongly unstable* asymptotic spectrum. In the limit of large delay strongly unstable spectrum does not depend on the exact values of delay time τ.

DEFINITION 6. (Asymptotic continuous spectrum) The *asymptotic continuous spectrum* $\mathcal{A}_c$ is the set of complex numbers $\gamma + i\xi \in \mathbb{C}$ such that $h(i\xi, e^{-\gamma - i\Theta}) = 0$ for some $\Theta \in \mathbb{R}$.

Here, we are looking for the eigenvalues $\lambda \in \mathbb{C}$ which scale in the limit of $\tau \to \infty$ as

$$\lambda = \frac{\gamma}{\tau} + i\xi, \tag{2.2.4}$$

with the real parameters γ and ξ. Inserting this ansatz into Eq. (2.2.2), one obtains in leading order the equation

$$\det\left(-i\xi I + A + Be^{-\gamma}e^{-i\Theta}\right) = 0, \tag{2.2.5}$$

where $\Theta = -\xi\tau$. One can note that for large values of τ the term $e^{i\Theta}$ is rapidly oscillating in ξ. The motivation behind the name *asymptotic continuous spectrum* then is clear: if we have $\gamma_0 + i\xi_0 \in \mathcal{A}_c$ and the corresponding value of Θ_0, and $\partial_2 h(i\xi_0, e^{-\gamma_0 - i\Theta_0}) \neq 0$ (which is generally the case), then a whole curve $\gamma(\xi) + i\Theta(\xi)$ satisfies $h(i\xi, e^{-\gamma(\xi) - i\Theta(\xi)}) = 0$ for $\xi \approx \xi_0$. Therefore, Θ can be considered as an artificial phase parameter and determine the solutions to Eq. (2.2.5) along the curve in the (γ, ξ)-plane that is parametrized by Θ and not dependent on the exact delay time τ.

Then, the following Theorem [78, 77] applies:

THEOREM 7. *(Stability/Instability for large delay). The stationary solution $\hat{u}$ of equation (2.2.1) is exponentially stable for all sufficiently large τ if all of the following conditions hold:*

S-1 (No strong instability) *all elements of the instantaneous spectrum $\Sigma_{\mathcal{A}}$ have negative real part (this implies in particular that the strongly unstable spectrum $\mathcal{A}_+$ is empty), and*

S-2 (Weak stability) *The asymptotic continuous spectrum $\mathcal{A}_c$ is contained in $\{z \in \mathbb{C} : \mathrm{Re}\, z < 0\}$.*

The solution $\hat{u}$ is exponentially unstable for all sufficiently large delay times τ if one of the following conditions holds:

U-1 (Strong instability) *the strongly unstable spectrum $\mathcal{A}_+$ is non-empty, or* ***U-2 (Weak instability)*** *a non-empty subset of the asymptotic continuous spectrum $\mathcal{A}_c$ has positive real part.*

Note that in [78], Theorem 7 is formulated and proven for periodic solutions and can be extended to the case of the stationary solutions. Following e.g. [76], the Theorem 7 can be reformulated in the following practical way which is suitable to application for the tasks of this Thesis.

In short, the spectrum which defines the instability of solution in the equation with large delay can be decomposed into two parts with different scaling properties with respect to τ: asymptotic continuous spectrum, which scales as $Re(\lambda) \sim 1/\tau$, and strongly unstable spectrum, which scales as $Re(\lambda) \sim 1$ for large τ. Both parts of asymptotic spectrum do not depend on particular value of τ and lead to different destabilization scenarios.

The calculation of strongly unstable spectrum simply follows from Eq. (2.2.3). As for the calculation of asymptotic continuous spectrum, one can introduce $Y(\xi) = e^{-\gamma}e^{-i\Theta}$ and rewrite Eq. (2.2.5) as

$$\det\left(-i\xi I + A + BY\right) = 0. \tag{2.2.6}$$

Then, the equation (2.2.6) can be solved for a range of ξ and the real parts of the elements of asymptotic continuous spectrum can be found as

$$\gamma(\xi) = -\ln|Y(\xi)|.$$

The calculation of these curves is extremely simplified with respect to the original problem and moreover is independent of the delay time parameter τ. To recover the location of the eigenvalues one has to regard the scaling ansatz (2.2.4). Additionally, one needs some information about the actual positions of the eigenvalues along this curve. It is sufficient to notice that, to leading order, the distance of eigenvalues along the curves behaves like $2\pi k/\tau$ (for more details, see [76, 77, 78]). This shows that, using the scaling (2.2.4), in the limit of large τ the eigenvalues accumulate along the curves given by Eq. (2.2.5), while their distance tends to zero. This is the reason why the set of eigenvalues behaving in this way is called asymptotic continuous spectrum. Later in the Thesis, it will be demonstrated by the numerical calculations of the exact spectrum for the specific solutions of delay ODEs and PDEs that the distance between eigenvalues scales inversely proportional to the delay time.

Remark 8. When $\gamma(\xi)$ becomes positive for certain intervals of ξ, different destabilization scenarios appear, which depend on the way how the pseudo-continuous spectral curve $\gamma(\xi)$ crosses the imaginary axis. The corresponding classification for the case of ODEs with large delay was reported in [76].

In this Thesis, the large delay approximation is used to study the stability properties of spatially extended systems described by PDEs with large delay. In this case, instead of the characteristic equation (2.2.2), one should look at the transcendental eigenvalue problem (2.1.5) and then apply the same steps as in the delay ODE case. In a similar fashion to Eq. (2.2.6), one can introduce $Y = e^{-\gamma}e^{-i\Theta}$

and instead of the computationally cumbersome equation (2.1.5), has to solve a series of the generalized eigenvalue problems for eigenpairs $(Y = e^{-\gamma}e^{-i\Theta}, \Psi)$ with different values of ξ:

$$-(i\xi + A)\Psi = -BY\Psi.$$

The asymptotic continuous spectral curves which approximate the exact eigenvalues for large delays are then given by $\gamma(\xi) = -\ln|Y(\xi)|$.

In contrary to the ODE case, for PDEs the alternative approach to solution of transcendental problem which involves the calculation of Lambert W functions [80] is generally not applicable, that means the reduction of the computational time needed for computation of the spectrum by the large delay approximation is even more substantial.

To our knowledge, this is the first case of application of the large delay approximation to delay PDEs. The classification of the instabilities then follows the aforementioned one for ODEs [76]. The feasibility and correctness of approach will be demonstrated in Chapter 4 of the Thesis by comparison of the strongly unstable spectrum and asymptotic continuous spectrum curves with exact eigenvalues numerically calculated for large delay time.

2.3. Fredholm alternative and bilinear form for delay partial differential equations

In the course of the analytical investigations in this Thesis the following mathematical problem is encountered several times: after the application of multiscale analysis method to the model equations, one arrives to the non-homogenous equation for the first order correction to the solution. This implies the application of the Fredholm alternative (also known as the alternative theorem [64]). It is well-known that in the case of delay ordinary differential equations, the Fredholm alternative is a powerful tool for the investigation of boundary-value problems [34]. It was successfully applied to study analytically the localized solutions in spatially extended systems [81, 82] and coupled systems with delay [83]. Here, the Fredholm alternative for the particular cases of delay (functional) partial differential equations treated in this Thesis is formulated.

Let us consider the abstract non-homogenous linear functional differential equation

$$\dot{u}(t) - Lu(t) - F(u_t) = \psi \tag{2.3.1}$$

where $u_t, \psi \in C([-\tau, 0]; X)$, $L : X \to X$ and linear operator $F : C([0, \tau]; X) \to X$ is given by

$$F(\phi) = \int_{-\tau}^{0} d\eta(\theta)\phi(\theta),$$

where $\eta : [-\tau, 0] \to B(X, X)$ is of bounded variation.

We are looking for the solution of system (2.3.1) $\phi \in C([-\tau, 0]; X)$ as the solution of non-homogeneous equation $A\phi = \psi$, where $A : C \to C$ is defined by

$$\begin{aligned} \mathrm{Dom}(A) = \{\phi \in C; \dot{\phi} \in C, \phi(0) \in \mathrm{Dom}(L) \text{ and} \\ \dot{\phi}^{-}(0) = L\phi(0) + \int_{-\tau}^{0} d\eta(\theta)\phi(\theta)\}, \\ (A\phi)(\theta) = \dot{\phi}(\theta), \quad -\tau \leq \theta \leq 0. \end{aligned} \tag{2.3.2}$$

It is proven in [64], that A is the infinitesimal generator of the semigroup generated by the homogenous system

$$\dot{u}(t) = Lu(t) + F\left(u_t\right). \tag{2.3.3}$$

Let X' be the dual space of X and $C' = C([0, \tau]; X')$. In what follows, $L' : X' \to X'$ and $\eta' : [-\tau, 0] \to B(X', X')$ are the dual operators to L and η, η' is of bounded variation [64].

Let us then introduce the operator $A' : C' \to C'$ defined by:

$$\begin{aligned} \mathrm{Dom}(A') = \{\alpha \in C; \dot{\alpha} \in C, \alpha(0) \in \mathrm{Dom}(L') \text{ and} \\ -\dot{\alpha}(0) = L'\alpha(0) + \int_{-\tau}^{0} d\eta'(\theta)\alpha(\text{-}\theta)\}, \\ (-A'\alpha)(s) = -\dot{\alpha}(s), \quad 0 \leq s \leq \tau. \end{aligned} \tag{2.3.4}$$

The system generated by the operator A' (2.3.4) is called adjoint to the system (2.3.3), see the detailed discussion of adjoint systems in case of FDEs in e.g. [34].

Finally, we introduce the bilinear form $\langle \cdot, \cdot \rangle$ from $C \times C'$ to the scalar field, which is defined as follows:

$$\langle \phi, \alpha \rangle = (\phi(0), \alpha(0)) - \int_{-\tau}^{0} \int_{0}^{\theta} (d\eta(\theta)\phi(\xi), \alpha(\xi - \theta))\, d\xi, \tag{2.3.5}$$

where $(x, x') = x'(x)$ for $x \in C$ and $x' \in C'$. It is proven in [64], that for the bilinear form (2.3.5) operator $A^{'}$ satisfies the equality $\langle A\phi, \alpha \rangle = \left\langle \phi, A^{'}\alpha \right\rangle$.

Note, that non-zero eigenfunctions $y \in \mathrm{Ker}(A - \lambda I)$ have the form $y(t) = y(0)e^{\lambda t}$ [64], where $y(0)$ can be found by solving characteristic equation

$$\Delta(\lambda)y(0) = \left[L - \lambda I + \int_{-\tau}^{0} d\eta(\theta)e^{\lambda\theta}\right] y(0) = 0,$$

and, similarly, $0 \neq \alpha \in \mathrm{Ker}(A^{'} - \lambda I)$ have the form $\alpha(t) = \alpha(0)e^{-\lambda t}$, where $\alpha(0)$ is obtained by solving characteristic equation for the adjoint problem

$$\Delta(\lambda)\alpha = \left[L' - \lambda I + \int_{-\tau}^{0} d\eta^{'}(\theta)e^{\lambda\theta}\right] \alpha(0) = 0.$$

Now, the Fredholm alternative for system (2.3.1) can be formulated:

THEOREM 9. *(Fredholm alternative [Alternative theorem [64]] for FPDE.) Suppose $\Delta(\lambda)$ has closed range and $\psi \in C$. A non-homogeneous equation $(A - \lambda I)\phi = \psi$ has a nontrivial solution ϕ if and only if $\langle \psi, \alpha \rangle = 0$ for all $\alpha \in \mathrm{Ker}(A^{'} - \lambda I)$.*

One can refer once again for the proof of Theorem 9 to [64]. The proof follows from the application of *Closed Range Theorem* [84, 85], see the Appendix B.

Note that in the case of equation with single delay τ and delayed linear operator B, the bilinear form (2.3.5) reads as follows:

$$\langle \phi, \alpha \rangle = (\phi(0), \alpha(0)) - \int_{-\tau}^{0} (B\phi(\xi), \alpha(\xi + \tau))\, d\xi.$$

For the case of DDEs, see [34, 28, 65], where the Fredholm alternative is formulated with corresponding bilinear form introduced in the similar manner. In Chapter 5 of the Thesis we use a special kind of the solvability condition (Fredholm alternative) for the case of the DDE with the periodic coefficients [28, 34], see the Appendix B.

CHAPTER 3

Complex Ginzburg-Landau equation with delayed feedback

3.1. Introduction

The complex Ginzburg-Landau equation (CGLE) plays an important role in modelling of various natural phenomena including nonlinear optical waves, second-order phase transitions, Rayleigh-Bénard convection, and superconductivity [86, 87]. It is an amplitude equation describing the onset of instability near an Andronov-Hopf bifurcation in spatially extended dynamical systems [66]. In nonlinear optics, equations of CGLE type are widely used to describe such phenomena as mode-locking in lasers [88, 89, 90], short pulse propagation in optical transmission lines [91], dynamics of multimode lasers, and transverse pattern formation in nonlinear optical media [92, 93]. While classical cubic CGLE describes a supercritical bifurcation, in the case of subcritical instability this equation is augmented with the fifth-order terms to allow the existence of stable pulselike solutions [94, 95].

In this Thesis we focus on one-dimensional delayed cubic-quintic CGLE for the complex amplitude $A(x,t)$

(3.1.1)
$$\partial_t A = \left(\beta + \frac{i}{2}\right)\partial_{xx}A + \delta A + (\epsilon + i)\,|A|^2 A + (\mu + i\nu)\,|A|^4 A + \eta e^{i\varphi} A(x, t-\tau).$$

The parameter $\beta > 0$ is the diffusion coefficient, second-order dispersion (diffraction) is scaled to $1/2$, and δ describes the linear loss or gain. Parameters ϵ, μ, and ν determine the shape of the nonlinearity. In particular, there are two qualitatively different cases: $\epsilon > 0$ and $\epsilon < 0$ corresponding to destabilizing and stabilizing role of the cubic nonlinearity. Equivalently, this leads to either subcritical or supercritical destabilization mechanisms for the homogeneous steady state $A = 0$. In this work, we take the values $\varepsilon < 0$, $\mu = \nu = 0$ for the supercritical case (cubic CGLE), and $\varepsilon > 0$, $\mu < 0$ for the subcritical case. Parameters η and φ determine the feedback rate and phase, respectively, whereas τ is the delay time. Model equation (3.1.1) can describe, for instance, a broad area optical system with delayed optical feedback [96, 60]. Notice that in the absence of delayed feedback term, $\eta = 0$, Eq. (3.1.1) becomes the classical cubic-quintic CGLE [86, 97]. On the other hand, without spatial derivative $\partial_{xx}A = 0$, Eq. (3.1.1) reduces to the normal form of the Hopf bifurcation with delayed feedback, which was studied recently in [53, 49, 98, 99, 100, 101] mainly in relation to the problem of the control of periodic solutions.

Although CGLE possesses a variety of different solutions [68, 102, 87, 67], in this part of the Thesis the focus is on the simplest plane waves of the form $A = a_0 e^{iqx+i\omega t}$. The stability of the trivial homogeneous solution $A = 0$ is studied as well. The localized solutions (cavity solitons) in the Ginzburg-Landau type equations (with the extension to the original delayed cubic-quintic CGLE (3.1.1)) are the subject of next chapter of the Thesis.

Criteria of the stability of plane wave solutions in the quintic CGLE without delay were briefly described in [97]. The stabilization of plane waves in one-dimensional and two-dimensional cubic CGLE by a combination of spatially shifted and temporally delayed non-invasive feedback was investigated in [103, 104] for the case when delay time and space shift are in the resonance with plane wave spatial and temporal wavenumbers. In this Chapter of he Thesis, we study cubic-quintic CGLE (as well as cubic CGLE as a special case) with arbitrary delay time and phase of the feedback, including the long delay limit case. For small delay times, there appears a single plane wave for every allowed spatial wavenumber q. The local stability of such solutions can be studied by calculating a dispersion relation for a given plane wave solution [97]. As time delay becomes comparable or longer than the characteristic time scale in the system, the number of plane waves for each admissible wavenumber grows linearly with τ. Moreover, the stability of each plane wave is no longer determined by a single classical dispersion relation, but a set of dispersion relations, which correspond to various "delay-induced modes". This set of dispersion relations is conveniently described using the methods from [76, 105, 77, 78, 32] by adding an additional dimension to the dispersion relation and studying a so-called "hybrid dispersion relation", which is a function of two arguments. Performing such a stability analysis, one can identify a large set of emerging asymptotically stable plane waves. Another contribution of this part of the Thesis is that we present a way how one can conveniently describe and visualize the whole set of plane waves (or other solutions) and their stability in system (3.1.1). As an interesting observation, one can find out that the branches of plane waves exhibit a snaking behavior as the linear gain parameter δ is changed.

This Chapter is organized as follows: Section 2 starts with the stability analysis of the homogeneous solution $A = 0$. In addition, in this section the first time in this Thesis the large delay approximation is introduced. This approximation technique will be used in a technically more elaborated way in Section 3 of this Chapter, where the existence and stability of the plane wave solutions $A = a_0 e^{iqx+i\omega t}$ are studied, and then later in the Thesis. Finally, the discussion on the results of this Chapter is given in Section 4.

3.2. Stability analysis of the homogeneous solution

3.2.1. The case without delayed feedback

This section starts with the stability analysis of the trivial homogeneous steady state solution $A(x,t) = 0$. Let me briefly recall the case when the feedback is absent, i.e. $\eta = 0$ [97, 103]. By substituting the perturbations of the form $e^{iqx+\lambda t}$

in the linearized equation, one obtains the characteristic equation

$$\chi(\lambda) = \lambda - \delta + \left(\beta + \frac{i}{2}\right) q^2 = 0. \tag{3.2.1}$$

Here q is a spatial wavenumber of the perturbation and λ determines the growth rate. The corresponding dispersion relation reads

$$\lambda(q) = \delta - \left(\beta + \frac{i}{2}\right) q^2.$$

When all the eigenvalues $\lambda(q)$ have negative real parts, the homogeneous solution is asymptotically stable. Since β is positive, one can conclude that the trivial solution is unstable for $\delta > 0$ and stable if $\delta < 0$. The most unstable wavenumber is $q = 0$.

3.2.2. The case of delay τ

For nonzero feedback rate the characteristic equation for the homogeneous solution becomes

$$\chi_1(\lambda) = \lambda - \delta - \eta e^{i\varphi} e^{-\lambda\tau} + \left(\beta + \frac{i}{2}\right) q^2 = 0. \tag{3.2.2}$$

The Andronov-Hopf bifurcation curves in the parameter plane (η, δ) can be found in a parametric form. To this end one can substitute $\lambda = i\omega$ into characteristic equation (3.2.2)

$$i\omega - \delta - \eta e^{i\varphi} e^{-i\omega\tau} + \left(\beta + \frac{i}{2}\right) q^2 = 0. \tag{3.2.3}$$

By separating real and imaginary parts of equation (3.2.3), two relations are obtained

$$\eta(\omega) = \frac{\frac{q^2}{2} + \omega}{\sin(\varphi - \omega\tau)}, \quad \delta(\omega) = \beta q^2 - \frac{\cos(\varphi - \omega\tau)\left(\frac{q^2}{2} + \omega\right)}{\sin(\varphi - \omega\tau)} \tag{3.2.4}$$

defining the Andronov-Hopf bifurcation curves with the imaginary part of the critical eigenvalue ω being a free parameter. Figure 3.2.1 shows these bifurcation curves in the plane of two parameters, linear gain δ and feedback rate η. The stability region of the trivial solution where real parts of all the eigenvalues $\lambda(q)$ are negative is shown in gray. A destabilization with respect to a given wavenumber q takes place when crossing the boundary of this region from inside. Figures 3.2.1(a,b) present the Andronov-Hopf bifurcation curves for the wavevector $q = 0$ at different values of the feedback phase, see also [106, 103]. For non-zero values of q, the instability region shifts to higher values of δ, as shown in Fig. 3.2.1(c). Therefore, the destabilization of the trivial homogeneous steady state first occurs at the most unstable wavenumber $q = 0$. For larger delay times the set of bifurcation curves becomes more dense, as it is seen from Fig. 3.2.1(d).

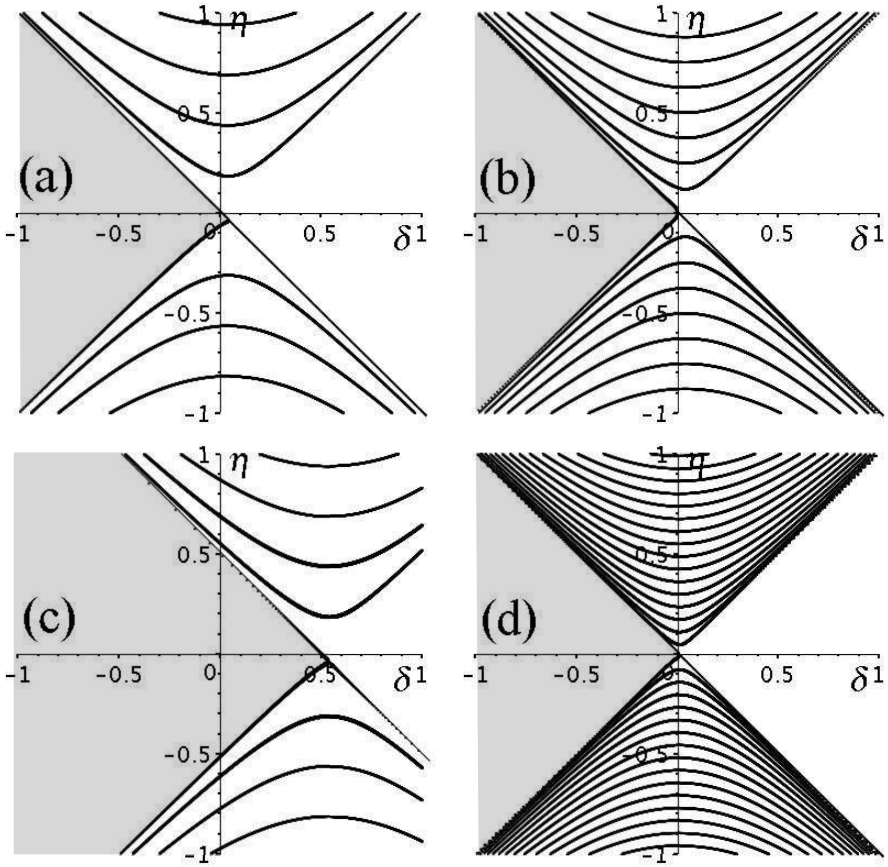

FIGURE 3.2.1. Andronov-Hopf bifurcation curves for the trivial homogeneous solution $A = 0$ of Eq. (3.1.1) in (δ, η) plane. The curves are given in a parametric form (3.2.4). Stability region of the solution $A = 0$ where the real part of the eigenvalue corresponding to the most unstable mode $q = 0$ is negative is shown in gray. Parameter values: (a) $\tau = 25$, $q = 0$, $\varphi = 0$, (b) $\tau = 25$, $q = 0$, $\varphi = \pi/2$, (c) $\tau = 25$, $q = 1$, $\varphi = 0$, (d) $\tau = 100$, $q = 0$, $\varphi = 0$. In all figures $\beta = 0.5$.

3.2.3. The case of large delay

Delay time τ for optical systems can exceed the internal time scales of the system by several orders of magnitude [40, 50, 58, 107]. To study this case, one can use the asymptotic technique of large delay approximation [76, 105, 77, 78] described in Chapter 2. As seen before, there are two types of delay-induced instabilities: strong instability and weak instability. Strong instability appears when there exists an eigenvalue (or Lyapunov exponent, for the periodic or chaotic case), which tends to some constant value $\lambda(\tau) \to \lambda_0$ with $\mathrm{Re}[\lambda_0] > 0$ as time delay increases. In this case, the contribution of the term $e^{-\lambda\tau}$ in the characteristic equation (3.2.2) can be neglected and we arrive to the following condition for the

strong instability of the mode with the wavenumber q

$$\lambda_0 = \delta + \left(\beta + \frac{i}{2}\right) q^2 > 0.$$

This instability condition coincides, in fact, with that for the feedback-free case. The most unstable mode $q = 0$ gives the condition for the strong instability of the solution $A = 0$:

$$\delta > 0. \tag{3.2.5}$$

Another type of instability, the weak one, can be described by a pseudo-continuous spectrum of eigenvalues, which scales as

$$\lambda = \frac{\gamma(\xi)}{\tau} + i\xi, \tag{3.2.6}$$

in the limit $\tau \to \infty$. More specifically, it was proved in [77, 78] that this spectrum is converging to a set of continuous curves (3.2.6) parametrized by ξ. Moreover, the leading terms of the real parts $\gamma(\xi)$ can be found explicitly by substituting (3.2.6) into the characteristic equation (3.2.2) and neglecting small terms of order $1/\tau$. In our case, one obtains the equation

$$i\xi - \delta - \eta e^{i\varphi} e^{-\gamma} e^{-i\xi\tau} + \left(\beta + \frac{i}{2}\right) q^2 = 0, \tag{3.2.7}$$

which is solved explicitly with respect to γ:

$$\gamma(\xi, q) = -\frac{1}{2} \ln \frac{\left(\delta - \beta q^2\right)^2 + \left(\xi + \frac{1}{2} q^2\right)^2}{\eta^2}. \tag{3.2.8}$$

In Eq. (3.2.8), we write an additional argument q, which indicates the dependence of the real part (rescaled by $1/\tau$) of the eigenvalues on the wavenumber. The function γ of two arguments extends naturally the dispersion relation, which is used [1] for partial differential equations without delayed feedback. Indeed, for a fixed ξ, the relation (3.2.8) determines the stability of the homogeneous state with respect to the perturbations with the wavenumber q, i.e. it is the dispersion relation. The new variable ξ stands for the delay induced modes, which appear additionally due to the delay. The homogeneous solution is locally asymptotically stable when $\gamma(\xi, q) < 0$.

Figure 3.2.2 shows the surfaces of $\gamma(\xi, q)$ calculated for different parameters. The red curve shows the level line $\gamma = 0$ given by the relation

$$\left(\delta - \beta q^2\right)^2 + \left(\frac{q^2}{2} + \xi\right)^2 = \eta^2. \tag{3.2.9}$$

Equation (3.2.9) defines an ellipse in ξ and q^2 coordinates. The trivial solution $A = 0$ is unstable if at least part of the ellipse lies in the half-plane $q^2 > 0$. Simple calculations show that, for $\beta > 0$, this is equivalent to the condition

$$\delta > -|\eta|. \tag{3.2.10}$$

Hence, the inequality (3.2.10) gives the weak instability condition for the solution $A = 0$, see Fig. 3.2.3. The corresponding critical wave numbers ξ_c and q_c correspond to the maximum of the quantity $\gamma(\xi, q)$. For $\delta \leq 0$, one has $q_c = 0$ and $\xi_c = 0$. Under the condition

$$\delta > |\eta| \tag{3.2.11}$$

there are two separated regions of unstable wavenumbers ξ and q, for which $\gamma(\xi, q) > 0$, see Fig. 3.2.2(a). These regions are symmetric with respect to the ξ-axis, $q = 0$. Otherwise, when only first of the two inequalities, (3.2.10) and (3.2.11), is satisfied, there is a single symmetric region of unstable wavenumbers, see Fig. 3.2.2(b). The boundary defined by the inequality (3.2.11) is shown in Fig. 3.2.3 by a dashed line. Figure 3.2.2(c) illustrates the case when the eigenvalue spectrum is located in the left half-plane of the complex plane, $\gamma(\xi, q) < 0$, and the homogeneous state $A = 0$ is stable.

The complete bifurcation diagram for the homogeneous state in the case of long delay is summarized in Fig. 3.2.3, where the regions of strong and weak instability are shown. It is instructive to compare this bifurcation diagram obtained in the limit $\tau \to 0$ with the exact bifurcation curves for different values of τ shown at Figs. 3.2.1(a,b,d).

3.3. Plane wave solutions

This Section proceeds with the study of existence and stability of plane wave solutions $A = a_0 e^{iqx+i\omega t}$ of Eq. (3.1.1). As for the homogeneous solution, we start with the case without delayed feedback in Sec. 3.3.1, and then consider the case with finite delay in Sec. 3.3.2. Further, in Sec. 3.3.3 the limit of a large delay time τ is investigated analytically, which allows for a deeper insight into the stability properties of plane wave solutions as compared to the arbitrary τ case. Finally, in Sec. 3.3.4 the results of numerical simulations are presented.

3.3.1. The case without delayed feedback

Substituting $A = a_0 e^{iqx+i\omega t}$ into Eq. (3.1.1), we obtain the relation between the unknown amplitude a_0, wavenumber q, and frequency ω of the plane wave solution:

$$i\omega = -\left(\beta + \frac{i}{2}\right) q^2 + \delta + (\epsilon + i)\, a_0^2 + (\mu + i\nu)\, a_0^4. \tag{3.3.1}$$

Due to the symmetry property of the CGLE $A \to -A$, this equation is symmetric under the reflection $a_0 \to -a_0$. Hence, one can restrict the analysis to the case $a_0 \geq 0$. The real and imaginary parts of Eq. (3.3.1) give the expressions for the amplitude $a_0^2(q)$ and the frequency $\omega(q)$ at a given wavenumber q:

$$a_0^2(q) = \frac{-\epsilon \pm \sqrt{\epsilon^2 - 4\mu(\delta - \beta q^2)}}{2\mu}, \quad \omega(q) = -\frac{q^2}{2} + a_0^2(q) + \nu a_0^4(q). \tag{3.3.2}$$

In particular, for the cubic CGLE (supercritical case with $\mu = \nu = 0$) one obtains

$$a_0^2(q) = \sqrt{\frac{\beta q^2 - \delta}{\epsilon}}, \quad \omega(q) = -\frac{q^2}{2} + \frac{\beta q^2 - \delta}{\epsilon}. \tag{3.3.3}$$

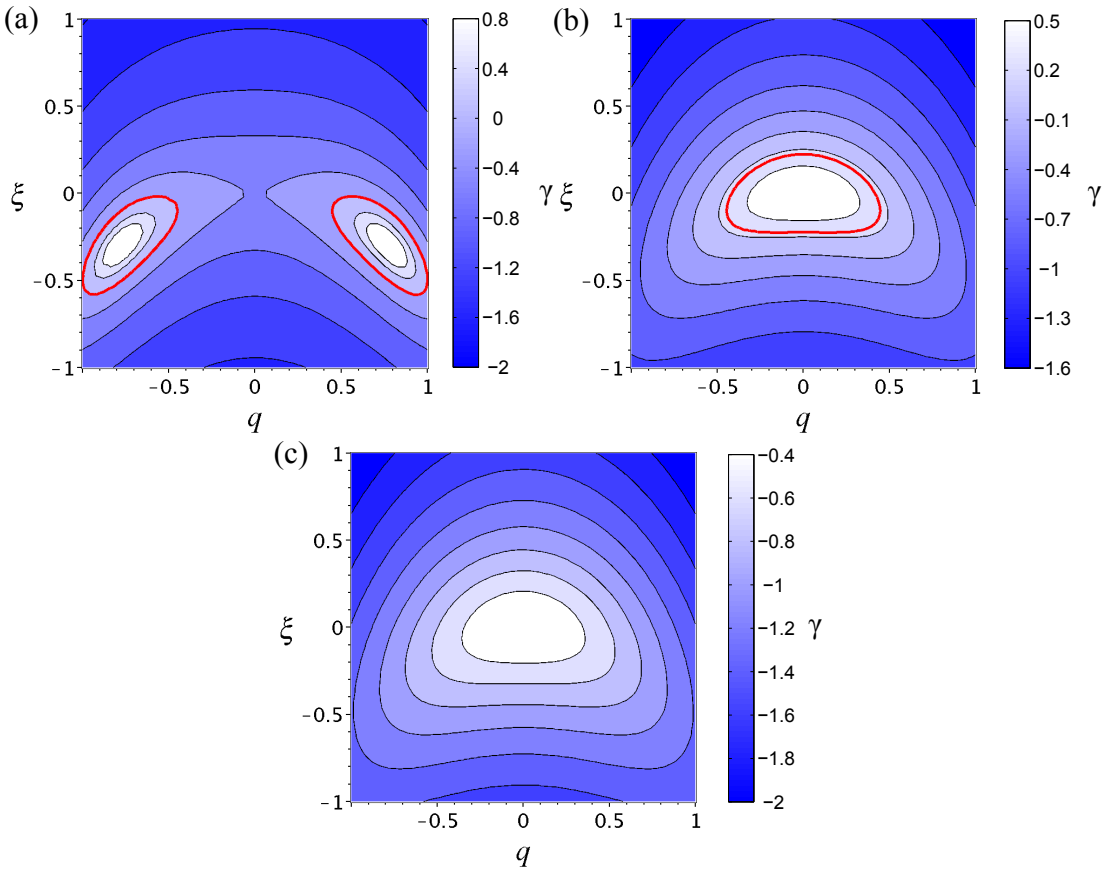

FIGURE 3.2.2. Contour plots of dispersion relation $\gamma(\xi, q)$, given by Eq. (3.2.8) for the homogeneous state $A = 0$ at large τ. Here ξ and q stand for the delay induced and the spatial wavenumber of the perturbations. If $\gamma < 0$ for all ξ and q and no strong instability occurs, the homogeneous state is stable. Parameter values: (a) unstable case with two regions of unstable wavenumbers: $\delta = 0.3$, $\eta = 0.2$, (b) unstable case with one unstable region: $\delta = -0.2$, $\eta = 0.3$, (c) stable case: $\delta = -0.3$, $\eta = 0.2$. Red curve shows the level lines $\gamma = 0$. In all figures $\beta = 0.5$.

Figures 3.3.1 (a) and (b) show the amplitude of the plane wave $a_0(\delta)$ as a function of the gain parameter δ for the supercritical and subcritical case, respectively. The branch of plane wave solutions with a given q emerges from the homogeneous state via Hopf bifurcation at $\delta = \beta q^2$. For the parameter values of Fig. 3.3.1(b) corresponding to the quintic CGLE, it bifurcates subcritically from $A = 0$ and undergoes a fold bifurcation at $\delta = \frac{\epsilon^2}{4\mu} + \beta q^2$.

Note that plane wave solutions of the CGLE without delay in supercritical case show the classical Benjamin-Feir scenario [97, 87]. Let us shortly discuss the stability of plane waves in the subcritical case of the quintic CGLE. Although the main ideas of this analysis are known from e.g. [97], there are still some details, which are not explained in [97], but are important for our further analysis. The

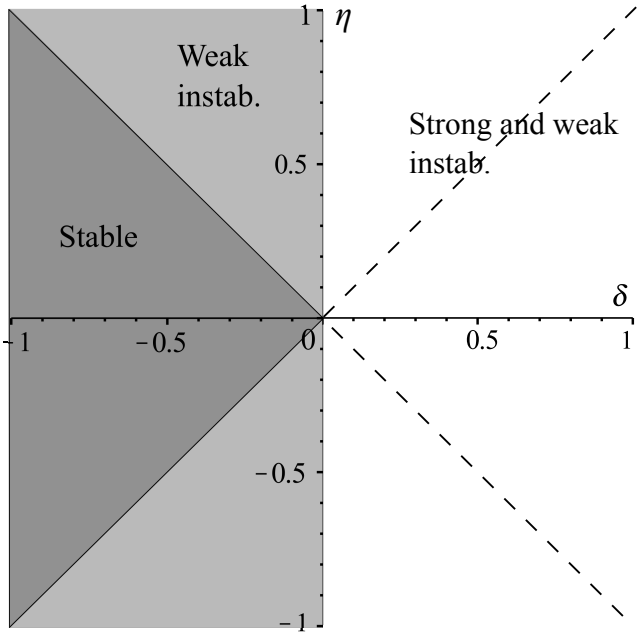

FIGURE 3.2.3. Bifurcation diagram of the homogeneous solution $A = 0$ in the parameter plane (δ, η) for large delay times. The diagram shows the region of stability (gray), weak and strong instability (light gray and white, respectively).

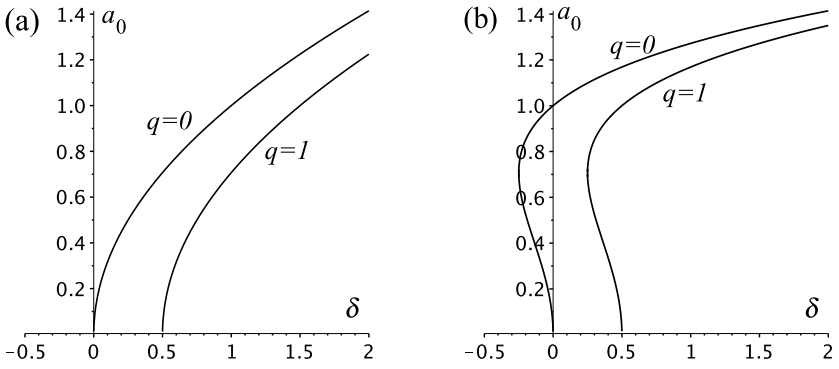

FIGURE 3.3.1. Amplitude of plane wave solutions $a_0(\delta)$ versus parameter δ in the absence of the delay, given by Eqs. (3.3.3) and (3.3.2), for different spatial wavenumbers q. (a) Supercritical case, $\epsilon = -1$, $\mu = \nu = 0$. (b) Subcritical case, $\epsilon = 1$, $\mu = -1$, $\nu = -0.1$. In all plots $\beta = 0.5$.

perturbed plane wave solutions have the form

$$A(x,t) = (a_0 + a_p)e^{iqx+i\omega t}, \tag{3.3.4}$$

where

$$a_p = a_+ e^{ikx+\lambda t} + \bar{a}_- e^{-ikx+\bar{\lambda}t} \tag{3.3.5}$$

is a small perturbation term with a growth rate λ. Here $\bar{\lambda}$ and $\bar{a}$ denote complex conjugation, and k stands for different perturbation modes. Substitution of (3.3.4) into CGLE (3.1.1) with $\eta = 0$ and linearization in a_p yields

$$\begin{aligned}\partial_t a_p + i\omega\,(a_0 + a_p) = \left(\beta + \frac{i}{2}\right)\left(\partial_{xx} a_p + 2iq\partial_x a_p - q^2(a_0 + a_p)\right) + \delta\,(a_0 + a_p) + \\ + (\epsilon + i)\left(a_0^3 + 2a_0^2 a_p + a_0^2\overline{a_p}\right) + (\mu + i\nu)\left(a_0^5 + 3a_0^2 a_p + 2a_0^2\overline{a_p}\right).\end{aligned} \tag{3.3.6}$$

After substituting (3.3.5) into (3.3.6) and using Eq. (3.3.1) one obtains an equation involving two linearly independent functions $e^{ikx+\lambda t}$ and $e^{-ikx+\bar{\lambda}t}$. Requiring that the coefficients at these functions are zero, one arrives at a system of linear equations for the unknowns a_- and a_+:

$$M \begin{pmatrix} a_+ \\ a_- \end{pmatrix} = 0$$

with

$$M = \begin{bmatrix} \lambda + \left(\beta + \frac{i}{2}\right)\left(k^2 + 2kq\right) - & -(\epsilon + i)\,a_0^2 - 2\,(\mu + i\nu)\,a_0^4 \\ -(\epsilon + i)\,a_0^2 - 2\,(\mu + i\nu)\,a_0^4 & \\ & \lambda + \left(\beta - \frac{i}{2}\right)\left(k^2 - 2kq\right) - \\ -(\epsilon - i)\,a_0^2 - 2\,(\mu - i\nu)\,a_0^4 & -(\epsilon - i)\,a_0^2 - (\mu - i\nu)\,a_0^4 \end{bmatrix}. \tag{3.3.7}$$

Since one is interested in non-trivial solutions (a_+, a_-), the characteristic equation for the perturbation growth rate $\lambda(k)$ is obtained by setting $\det M = 0$:

$$\begin{aligned}\lambda^2 + 2\left(ikq + \beta k^2 - \epsilon a_0^2 - 2\mu a_0^4\right)\lambda - 2\left((\nu + 2\mu\beta)\,k^2 + 2\,(\mu - 2\nu\beta)\,ikq\right)a_0^4 + \\ - \left((1 + 2\epsilon\beta)\,k^2 + 2\,(\epsilon - 2\beta)\,ikq\right)a_0^2 + \left(4\beta^2 + 1\right)\left(k^4/4 + k^2 q^2\right) = 0.\end{aligned} \tag{3.3.8}$$

Solutions $\lambda(k)$ can now be found explicitly and the maximum of their real parts determines the stability of plane waves. As it is seen from Fig. 3.3.2 the plane waves are stable for larger values of δ and become modulationally unstable with the decrease of δ. This instability appears when the real part of the derivative $\partial_{kk}\lambda(0)$ changes its sign from negative to positive, see insets (a) and (b) in Fig. 3.3.2.

The threshold of the modulational instability is given by the condition $\Re[\partial_{kk}\lambda(0)] = 0$. For small k (long-wavelength limit) the Taylor expansion of $\lambda(k)$ reads

$$\lambda(k) = \left(-\frac{C_3}{C_1} - q\right)ik + \left(-\frac{C_3^2}{128C_1^3} - \frac{C_2^2}{C_1} - \beta\right)k^2 + \mathcal{O}(k^3), \tag{3.3.9}$$

where $C_1 = \epsilon a_0^2 + 2\mu a_0^4$, $C_2 = 16\beta^2 q^2 + 4a_0^2 + 8\nu a_0^4$ and $C_3 = 64\beta^3 q^3 - 4\beta q C_2$. In particular, the stability boundary $\partial_{kk}\lambda(0) = 0$ is given by

$$\frac{C_3^2}{128C_1^3} + \frac{C_2^2}{C_1} + \beta = 0. \tag{3.3.10}$$

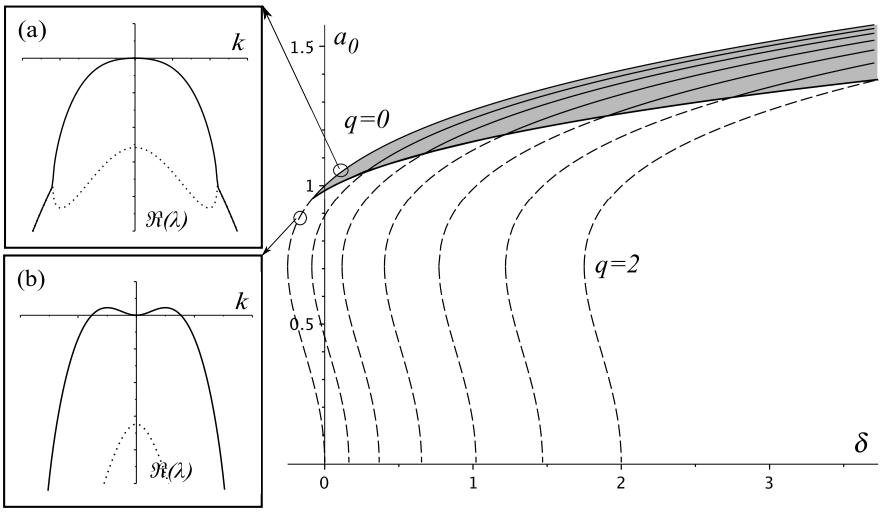

FIGURE 3.3.2. Amplitude of plane wave solutions $a_0(\delta)$ in quintic CGLE (3.1.1) in the absence of the delay for different spatial wavenumbers q. Stability domain is shown in gray. Insets show the real part of the growth rate $\lambda(k)$ for selected plane waves (solid and dotted lines correspond to upper and lower branches of solutions, respectively). (a) $\delta = 0.1$, $q = 0$, $a_0 \simeq 1.04$, stable case, (b) $\delta = -0.2$, $q = 0$, $a_0 \simeq 0.85$, unstable case. Other parameters: $\beta = 0.5$, $\epsilon = 1$, $\mu = -1$, and $\nu = -0.1$.

Figure 3.3.2 shows the amplitude a_0 of plane wave solutions versus δ for different wavenumbers q along with the examples of $\Re[\lambda(k)]$ for stable an unstable cases respectively. Stable solutions are depicted by solid lines and the stable domain is shown in gray. The first zero wavenumber plane wave solution $A = a_0 e^{i\omega t}$ with $q = 0$, $a_0^2 = [-\epsilon \pm \sqrt{\epsilon^2 - 4\mu\delta}]/2\mu$, and $\omega = a_0^2 + \nu a_0^4$ is stable for

$$\delta > \frac{4\beta\epsilon\,(\beta\epsilon + 2\beta\mu + \nu + 1) + 2(2\beta\mu + \nu + 1)}{4(2\beta\mu + \nu)^2}. \tag{3.3.11}$$

With the further increase of δ, stable plane wave solutions with $q^2 > 0$ appear.

3.3.2. Case of delay τ

Description of the set of plane wave solutions

Substituting $A = a_0 e^{iqx + i\omega t}$ into CGLE with delayed feedback (3.1.1) one obtains the equation connecting the amplitude a_0, frequency ω, and wavenumber q of the plane waves

$$i\omega = -\left(\beta + \frac{i}{2}\right) q^2 + \delta + (\epsilon + i)\, a_0^2 + (\mu + i\nu)\, a_0^4 + \eta e^{i\varphi} e^{-i\omega\tau}. \tag{3.3.12}$$

After separating real and imaginary parts of (3.3.12), one obtains

$$0 = -\beta q^2 + \delta + \epsilon a_0^2 + \mu a_0^4 + \eta\cos(\omega\tau - \varphi), \tag{3.3.13}$$

$$\omega = -\frac{q^2}{2} + a_0^2 + \nu a_0^4 - \eta\sin(\omega\tau - \varphi). \tag{3.3.14}$$

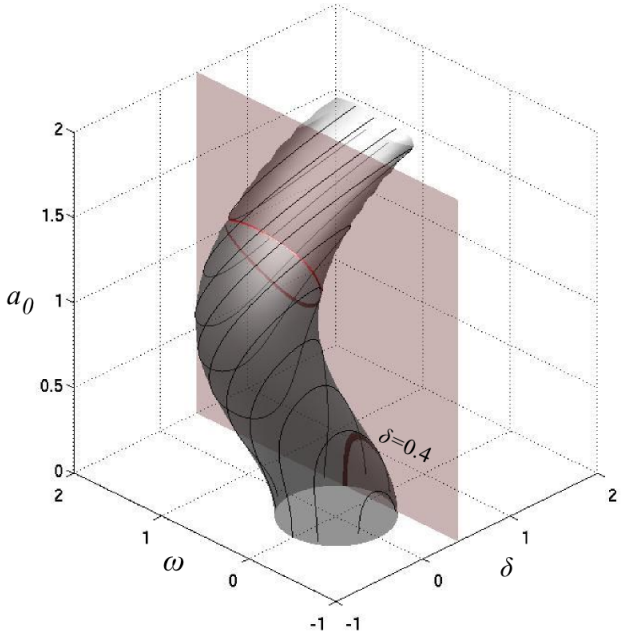

FIGURE 3.3.3. Amplitudes a_0 and frequencies ω of plane wave solutions as a function of δ, defined by Eq. (3.3.15). Black curve indicates the branch of plane wave solutions (defined by (3.3.13)–(3.3.14)) for $\tau = 25$ and $\varphi = 0$. Other parameters: $q = 0$, $\eta = 0.5$, $\beta = 0.5$, $\epsilon = 1$, $\mu = -1$, and $\nu = -0.1$. Red curve shows the cross-section of the tube by the plane of the fixed parameter $\delta = 0.4$.

In the coordinates (δ, ω, a_0), the set of solutions of Eqs. (3.3.13)–(3.3.14) for each q lies on the surface which is implicitly defined by the following equation

$$\left(-\beta q^2 + \delta + \epsilon a_0^2 + \mu a_0^4\right)^2 + \left(\omega + \frac{q^2}{2} - a_0^2 - \nu a_0^4\right)^2 = \eta^2, \tag{3.3.15}$$

obtained from Eqs. (3.3.13)–(3.3.14) by eliminating $\omega\tau - \varphi$. This set has a tube-like structure, topologically equivalent to a cylinder (see Fig. 3.3.3). Indeed, one can introduce the parametric curve $(\tilde{\delta}(a_0), \tilde{\omega}(a_0))$ with $\tilde{\delta}(a_0) = \beta q^2 - \epsilon a_0^2 - \mu a_0^4$ and $\tilde{\omega}(a_0) = -q^2/2 + a_0^2 + \nu a_0^4$, so that Eq. (3.3.15) becomes

$$(\delta - \tilde{\delta}(a_0))^2 + (\omega - \tilde{\omega}(a_0))^2 = \eta^2 \tag{3.3.16}$$

and defines a surface of the tube. Its cross-section for a fixed value of a_0 is a circle with the diameter η. For a fixed control parameter δ, the cross-section can have more elaborate form, see Fig. 3.3.3.

In order to analyze how the number of plane waves depends on the delay time τ, the following equation for ω can be obtained from (3.3.14) and (3.3.13):

$$\omega = \frac{2\pi n}{\tau} + \frac{1}{\tau}F(\omega), \quad n \in \mathbb{Z} \tag{3.3.17}$$

where

$$F(\omega) := \varphi + \arctan\left[\left(-\omega - \frac{q^2}{2} + a_0^2 + \nu a_0^4\right) / \left(\beta q^2 - \delta - \epsilon a_0^2 - \mu a_0^4\right)\right].$$

For large τ, this equation has a unique solution ω_n for any n and all values of the parameters, for which the denominator in the expression for $F(\omega)$ is not zero. This solution is given by

$$\omega_n = \frac{2\pi n}{\tau} + \frac{1}{\tau}F\left(\frac{2\pi n}{\tau}\right) + O(1/\tau^2).$$

The distances between the adjacent solutions $\omega_{n+1} - \omega_n = 2\pi/\tau + O(1/\tau^2)$ decrease for large τ and the solutions fill the whole admissible interval of ω. The number of solutions grows linearly with τ.

Another possibility is to find the set of exact solutions of system of equations (3.3.13)–(3.3.14) with help of numerical methods. Solving (3.3.13) with respect to a_0^2 and substituting the result into (3.3.14), one obtains the equation for the frequencies ω of the plane waves

$$\begin{aligned} 0 = f_\pm(\omega) = \omega + \frac{q^2}{2} + \\ + \frac{\epsilon \pm \sqrt{\epsilon^2 - 4\mu\left(\delta - \beta q^2 + \eta\cos\left(\omega\tau - \varphi\right)\right)}}{2\mu} - \\ - \frac{\nu\left(\epsilon \pm \sqrt{\epsilon^2 - 4\mu\left(\delta - \beta q^2 + \eta\cos\left(\omega\tau - \varphi\right)\right)}\right)^2}{4\mu^2} + \eta\sin\left(\omega\tau - \varphi\right), \end{aligned} \tag{3.3.18}$$

which can be studied numerically for any fixed value of the delay τ. The functions $f_\pm(\omega)$ are shown on Fig. 3.3.4. In particular, with the increase of τ the functions $f_\pm(\omega)$ oscillate faster and number of solutions grows. This corresponds to a general result obtained in [108] stating that in the limit of large delay the number of periodic solutions increases linearly with τ. Eventually the solutions fill the curves defined by relation (3.3.15). Figure (3.3.5) shows the exact solutions (a_0, ω) for increasing delay time τ as points on these curves. It is interesting to remark the strong analogy between the curve (3.3.15) of the plane wave solutions and the ellipse of external cavity modes appearing in rate equation models for semiconductor lasers with time delayed feedback, where the notion is frequently used [109, 110, 105, 40, 111, 112].

Let us consider the effect of the feedback phase φ, which shifts the function $f_\pm(\omega)$, see Fig. 3.3.4. For small delay times, when $f_\pm(\omega)$ oscillates slowly, the role of φ is pronounced since a few of individual solutions are moved along the curve $a_0(\omega)$ and new solutions can be born. As τ increases, the overall number of plane

wave solutions becomes large, thus diminishing the effect of the feedback phase, as shown in Figs. 3.3.4(b) and 3.3.5(b).

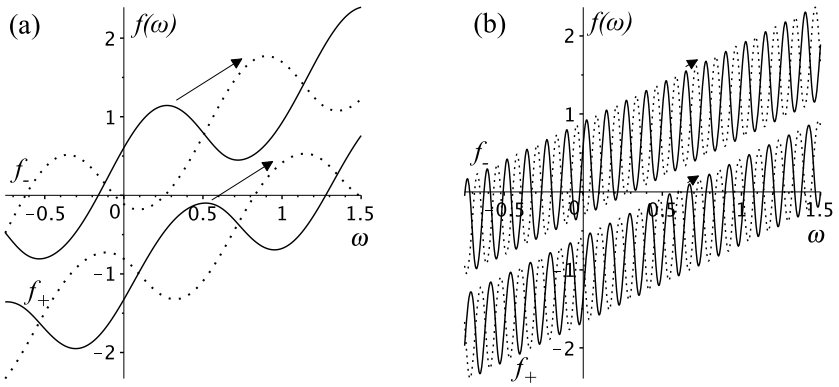

FIGURE 3.3.4. Zeros of functions $f_{\pm}(\omega)$ determine frequencies ω of plane waves. $f_{\pm}(\omega)$ are calculated from Eq. (3.3.18) for (a) $\tau = 5$ and (b) $\tau = 50$. Solid lines: $\varphi = 0$, dashed lines: $\varphi = \pi$. Other parameters: $q = 0$, $\delta = 0.4$, $\eta = 0.5$, $\beta = 0.5$, $\epsilon = 1$, $\mu = -1$, and $\nu = -0.1$.

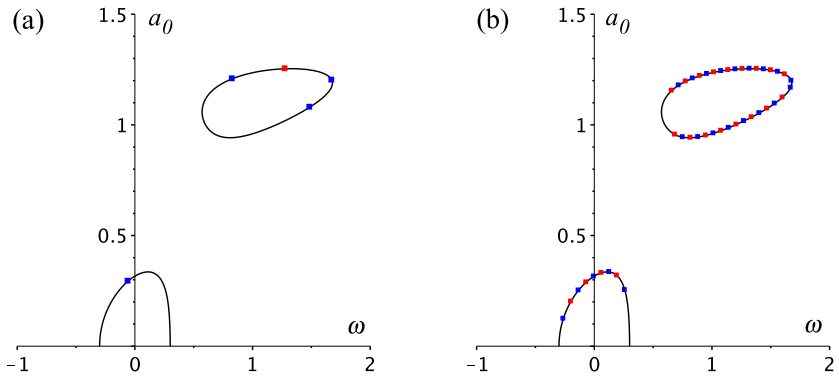

FIGURE 3.3.5. Amplitudes a_0 and frequencies ω of plane wave solutions for fixed $\delta = 0.4$. The solutions are located on curves determined by Eq. (3.3.15) (solid lines), which are independent of the delay τ. Exact plane wave solutions for different values of τ are shown by points: (a) $\tau = 5$, (b) $\tau = 50$. Red points: $\varphi = 0$, blue points: $\varphi = \pi$. Other parameters: $q = 0$, $\eta = 0.5$, $\beta = 0.5$, $\epsilon = 1$, $\mu = -1$, and $\nu = -0.1$.

Even though exact values of a_0 and ω for any fixed set of parameters can only be computed numerically, the branches of plane wave solutions versus parameter δ can be obtained explicitly in a parametric form $(a_0(\omega), \delta(\omega))$. Namely, the amplitude $a_0(\omega)$ is the solution of Eq. (3.3.14). Substituting $a_0(\omega)$ into Eq. (3.3.13) and solving the resulting equation for δ, one obtains an expression for

$\delta(\omega)$. As a result, the branches of plane waves have the parametric form

$$a_0(\omega) := \left\{ \text{solution of } \nu\left(a_0^2\right)^2 + a_0^2 - \eta\sin(\omega\tau - \varphi) - \omega - \frac{q^2}{2} = 0 \right\}, \tag{3.3.19}$$

$$\delta(\omega) := \beta q^2 - \epsilon a_0^2(\omega) - \mu a_0^4(\omega) - \eta\cos(\omega\tau - \varphi).$$

The branches of plane wave solutions obtained using this procedure are shown in Fig. 3.3.6 and Fig. 3.3.7 for cubic and quintic CGLE, respectively. Interestingly, the branches have the form of snaking curves, which are constrained between two "limiting" branches (3.3.2) (red and blue curves in Figs. 3.3.6-3.3.7), which can be obtained by setting $\tau = 0$, $\varphi = 0$ and $\tau = 0$, $\varphi = \pi$, respectively. One can see that the increase of τ leads to even more dense snaking of the curve (Fig. 3.3.6(b)), whereas the increase of q shifts the branches to the right.

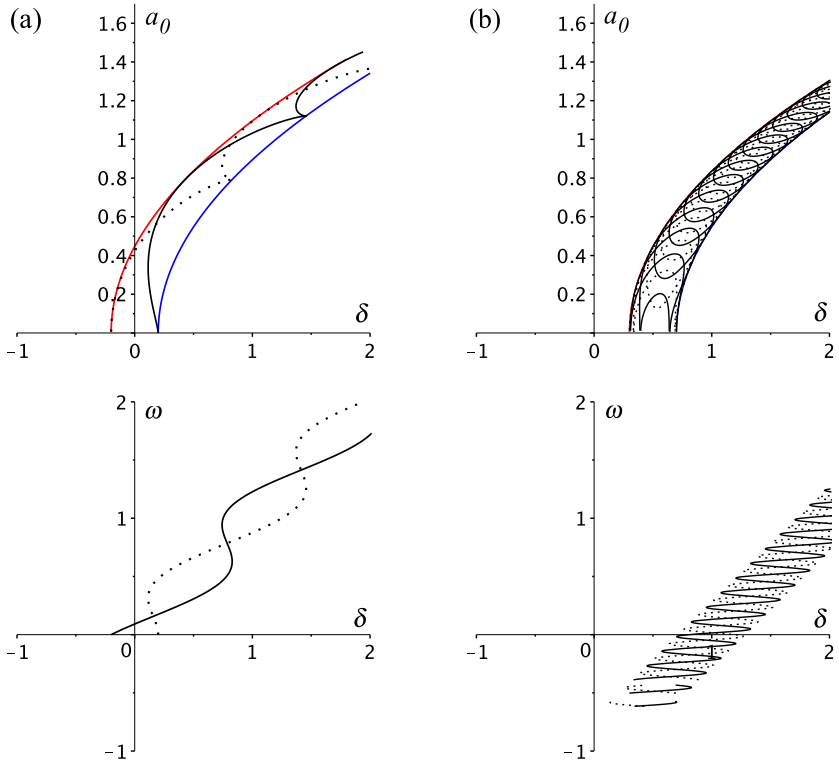

FIGURE 3.3.6. Amplitudes $a_0(\delta)$ and frequencies $\omega(\delta)$ of plane wave solutions in cubic CGLE with delayed feedback for (a) $\tau = 5$, $q = 0$, (b) $\tau = 50$, $q = 1$. Solid black lines: $\varphi = 0$, dotted lines: $\varphi = \pi$. The enveloping red and blue lines are the branches of plane waves solutions for $\tau = 0$, $\varphi = \pi$ and $\tau = 0$, $\varphi = 0$, respectively. Other parameters: $\eta = 0.2$, $\beta = 0.5$, $\epsilon = 1$, $\mu = \nu = 0$.

Stability of plane wave solutions

As in the case without delayed feedback, the ansatz (3.3.4) can be applied to investigate the stability of plane waves. After substituting it into delayed CGLE

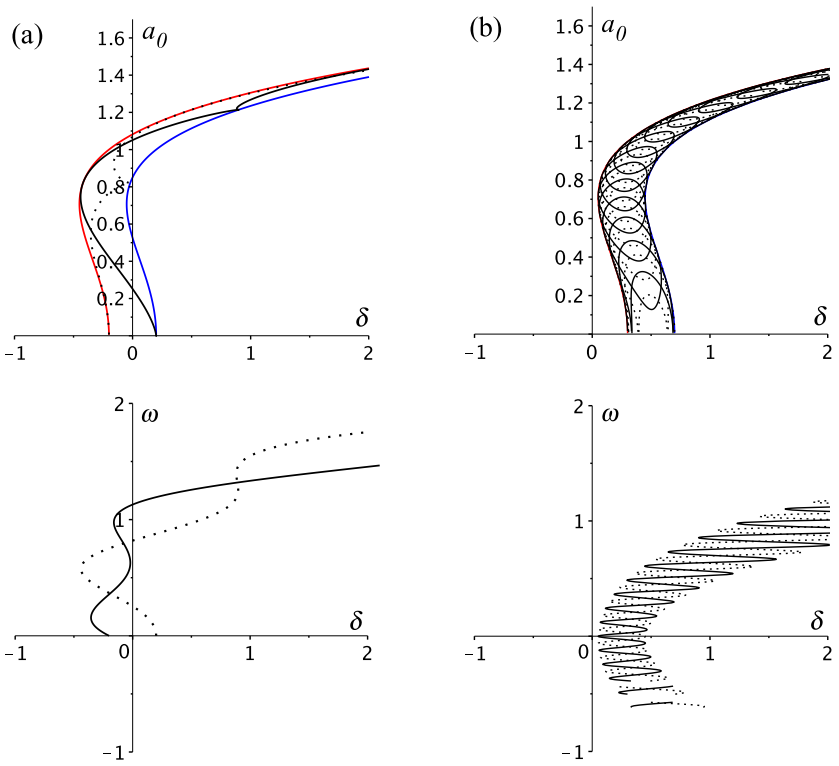

FIGURE 3.3.7. Amplitudes $a_0(\delta)$ and frequencies $\omega(\delta)$ of plane wave solutions in quintic CGLE with delayed feedback for (a) $\tau = 5$, $q = 0$, (b) $\tau = 50$, $q = 1$. Solid black lines: $\varphi = 0$, dotted lines: $\varphi = \pi$. The enveloping red and blue lines are the branches of plane wave solutions for $\tau = 0$, $\varphi = \pi$ and $\tau = 0$, $\varphi = 0$, respectively. Other parameters: $\eta = 0.2$, $\beta = 0.5$, $\epsilon = 1$, $\mu = -1$, $\nu = -0.1$.

(3.1.1) and linearization in a_p, one obtains:

$$\partial_t a_p + i\omega(a_0 + a_p) = \left(\beta + \frac{i}{2}\right)\left(\partial_{xx} a_p + 2iq\partial_x a_p - q^2(a_0 + a_p)\right) + \delta(a_0 + a_p) + \\ + (\epsilon + i)\left(a_0^3 + 2a_0^2 a_p + a_0^2\overline{a_p}\right) + (\mu + i\nu)\left(a_0^5 + 3a_0^2 a_p + 2a_0^2\overline{a_p}\right) \\ + \eta e^{i\varphi - i\omega\tau}\left(a_0 + a_p(t - \tau)\right). \tag{3.3.20}$$

Then, one can simplify this equation using Eq. (3.3.12) and substitute the exponential ansatz (3.3.5) for $a_p(x,t)$ into it. As a result, similarly to Section 3.3.1, we obtain a linear system of equations with respect to two unknowns a_+ and a_-:

$$M_\tau \begin{pmatrix} a_+ \\ a_- \end{pmatrix} = 0,$$

where

(3.3.21)
$$M_\tau = \begin{bmatrix} \lambda + i\omega - \delta + \left(\beta + \frac{i}{2}\right)\left(k^2 + 2kq + q^2\right) - & -(\epsilon + i)\, a_0^2 - 2(\mu + i\nu)\, a_0^4 \\ -2(\epsilon + i)\, a_0^2 - 3(\mu + i\nu)\, a_0^4 - \eta e^{-\lambda\tau} e^{i\varphi - i\omega\tau} & \\ & \\ & \lambda - i\omega - \delta + \left(\beta - \frac{i}{2}\right)\left(k^2 - 2kq + q^2\right) - \\ -(\epsilon - i)\, a_0^2 - 2(\mu - i\nu)\, a_0^4 & -2(\epsilon - i)\, a_0^2 - 3(\mu - i\nu)\, a_0^4 - \eta e^{-\lambda\tau} e^{-i\varphi + i\omega\tau} \end{bmatrix}.$$

The condition

(3.3.22)
$$\det M_\tau = 0$$

now gives us the characteristic equation for the perturbation growth rate λ.

Stability of individual plane wave solutions with arbitrary delay time τ is determined by the real parts of the roots of the characteristic equation (3.3.22). If for all k, the roots satisfy $\mathrm{Re}[\lambda] < 0$ (except the trivial one with $\mathrm{Re}[\lambda] = 0$), then the plane wave is spectrally stable. For a fixed q, the branch of plane waves is given parametrically by $(a_0(\omega), \delta(\omega))$, defined by Eq. (3.3.19). Substituting $a_0(\omega)$ and $\delta(\omega)$ in Eq. (3.3.22), one obtains nonlinear characteristic equation for λ

(3.3.23)
$$\mathcal{F}(\lambda; q, \omega, k, \mathbf{p}) = 0,$$

where $\mathbf{p}$ denotes system parameters $(\beta, \epsilon, \mu, \nu, \eta, \varphi, \tau)$. Equation (3.3.23) was solved numerically for fixed values of $\mathbf{p}$ and varying ω. In this way one obtains the stability properties for the parametrically defined family of plane waves $(a_0(\omega), \delta(\omega))$ for the given CGLE parameters and wavenumber q. Figure 3.3.8 shows the stability properties on the branches of plane waves $(a_0(\omega), \delta(\omega))$ with $q = 0$ and various delay times τ. Stable solutions are plotted in green, unstable in red. Figure 3.3.8(a) illustrates the effect of the feedback phase φ on plane wave solutions and their stability at relatively small delay time $\tau = 5$, whereas Fig. 3.3.8(b) depicts the bifurcations for larger delay time $\tau = 50$. One can observe the growing number of multistable plane waves with the increase of the delay. With the increase of the parameter δ high amplitude parts of the snaking branches with the higher amplitude become stable while low amplitude parts remain unstable. An additional analytical insight into the structure of stable and unstable regions is obtained by using the large delay approximation, which is discussed in the next section.

3.3.3. Large delay

For large delay times, the plane wave solutions fill the tube defined by Eq. (3.3.15) densely, see also Figs. 3.3.3 and 3.3.5(b). Hence, instead of looking at individual solutions and solving the transcendental Eq. (3.3.18), it is convenient to parametrize the whole family of solutions by a parameter $\theta = (\omega\tau\text{-}\varphi\text{+}\pi) \bmod 2\pi$, which may be represented as an angular coordinate on the tube. Every single solution for given control parameters and wavevector q can be uniquely defined by the coordinate θ. Therefore, one can consider the question about the stability of a plane wave at a given θ-value with the amplitude $a_0(\theta)$ and the frequency $\omega(\theta)$. The growth rate λ, which determines the stability of an individual plane wave solution, is obtained from the characteristic equation depending just on the system parameters and the coordinate θ. Note that $\theta = \pi$ corresponds to the plane

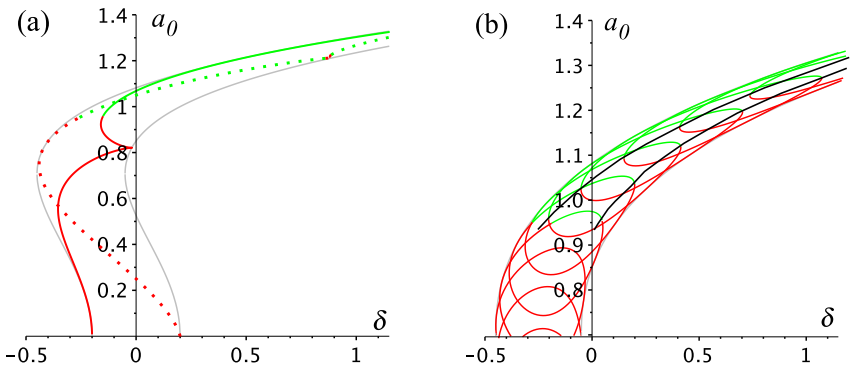

FIGURE 3.3.8. Stability of the branches of plain wave solutions for different delay times (a) $\tau = 5$, $\varphi = 0$ (solid line), $\varphi = \pi$ (dotted line) (b) $\tau = 50$, $\varphi = 0$. Stable parts are shown in green and unstable – in red. Black lines in (b) denote the destabilization borders in the limit of large delay. Other parameters: $\eta = 0.2$, $\beta = 0.5$, $\epsilon = 1$, $\mu = -1$, and $\nu = -0.1$.

waves with the maximal amplitude a_0. The two sides of the tube of plane wave solutions, one with $\theta < \pi$ and another with $\theta > \pi$, are projected onto the same set in the (δ, a_0) plane, but correspond to different values of ω.

To study the strong instability of plane wave solutions, again, as in Sec. 3.3.3, one neglects the terms containing $e^{-\lambda\tau}$ in Eq. (3.3.22). This gives us a quadratic equation for λ. For a given parameter θ, the plane wave is strongly unstable, if the maximum of $\mathrm{Re}[\lambda(k,\theta)]$ is positive. Figure 3.3.9 shows the real part of $\lambda(k,\theta)$ for reduced equation (3.3.22) for two different values of the wavenumber, $q = 0$ and $q = 1$ (δ is fixed to 0.5). Red curves depict zero level lines. One can observe, that at larger values of q, unlike the feedback-free case, the destabilization occurs first at non-zero values of the perturbation wavenumber k.

In order to determine the strong instability boundary of the plane wave solutions, in Fig. 3.3.10 we plot on (δ,θ) plane zero contour levels $\mathrm{Re}[\lambda(\delta,\theta)] = 0$ corresponding to different perturbation wavenumbers k. Figure 3.3.10(a) shows that for the plane wave with $q = 0$, stability border almost coincides with the zero level line corresponding to $k = 0$, depicted by the black line. By contrast, for the plane wave with $q = 1$ a significant part of stability border, shown in red color, corresponds to destabilization with non-zero perturbation wavenumber $k \sim 0.9$ (see Fig. 3.3.10(b)).

In the limit of large delay, the weak instability boundary is determined by the pseudo-continuous spectrum

$$\lambda = \frac{\gamma(\xi)}{\tau} + i\xi. \tag{3.3.24}$$

To calculate this spectrum we substitute (3.3.24) into Eq. (3.3.22) and neglect the terms proportional to γ/τ. Then, denoting

$$Y = e^{-\gamma} e^{-i\xi\tau}, \tag{3.3.25}$$

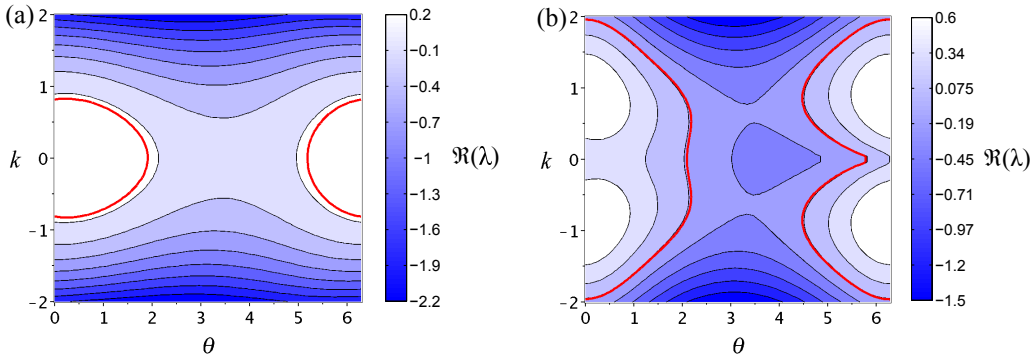

FIGURE 3.3.9. Real parts of the eigenvalues $\mathrm{Re}[\lambda(k,\theta)]$ describing the strong instability of plane waves. For a given plane wave, which is determined by the parameter θ, the positiveness of $\mathrm{Re}[\lambda(k,\theta)]$ for some k implies the strong instability. Red curves depict zero level lines. (a) $q = 0$, (b) $q = 1$. On panel (a), the plane waves are strongly unstable for $\theta \lesssim 1.9$ and $\theta \gtrsim 5.0$. On panel (b), the plane waves are strongly unstable for $\theta \lesssim 1.9$ and $\theta \gtrsim 4.5$. Other parameters are: $\delta = 0.5$, $\eta = 0.2$, $\beta = 0.5$, $\epsilon = 1$, $\mu = -1$, and $\nu = -0.1$.

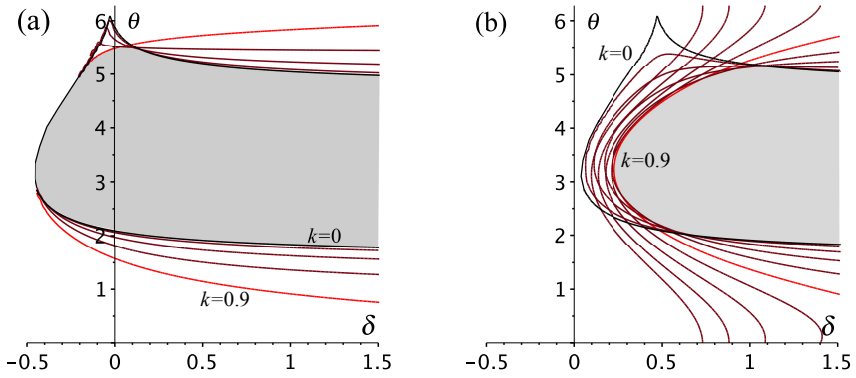

FIGURE 3.3.10. Strong instability of the plane wave solutions with $q = 0$ (a) and $q = 1$ (b). Gray region shows the absence of strong instability. Different curves indicate zero contour levels of $\Re[\lambda(\delta,\theta)]$ corresponding to different perturbation wavenumbers k. Contours, where destabilisation first happens, namely for $k = 0$ and $k = 0.9$, are shown in black and red lines, respectively. (a) $q = 0$, (b) $q = 1$. Other parameters: $\eta = 0.2$, $\beta = 0.5$, $\epsilon = 1$, $\mu = -1$, and $\nu = -0.1$.

we obtain the quadratic equation

$$Y^2 + a_1 Y + a_2 = 0, \tag{3.3.26}$$

where the coefficients a_1 and a_2 depend on the model equation parameters $\mathbf{p}$, plane wave (q,θ), wavenumber of the perturbation k, and the parameter of the pseudo-continuous spectrum ξ, see Eq. (3.3.24). The expressions for the coefficients a_1

and a_2 are extremely cumbersome, therefore they can be omitted for brevity as well as the explicit expressions for the solutions Y_1 and Y_2. The factor γ in (3.3.25) is then given by

$$\gamma_{1,2}(k, \xi; q, \theta, \mathbf{p}) = -\ln |Y_{1,2}|. \tag{3.3.27}$$

For every plane wave solution defined by q and θ and fixed parameters $\mathbf{p}$ one can obtain two surfaces $\gamma_{1,2}(k, \xi)$, which generalize the dispersion relation (see Sec. (3.2.3)). If $\gamma_{1,2} < 0$ for all wavenumbers k and delay modes ξ (except the trivial eigenvalue corresponding to the Goldstone mode), then the corresponding plane wave is stable (provided no strong instability exists). Otherwise, it is weakly unstable. Thus, the weak instability of the plane wave solutions is determined by considering the behavior of the two surfaces $\gamma_{1,2}(k, \xi)$, or, more specifically, the upper one.

Figure (3.3.11) shows the upper branch of $\gamma_{1,2}(k, \xi)$ calculated for different values of θ, δ, and q. Even though the surfaces $\gamma(k, \xi)$ are given by explicit expressions, it was not possible to find simple analytical conditions for weak instability in terms of θ and q. Instead, we have determined the sign of $\sup[\gamma(k, \xi)]$ numerically. The resulting bifurcation diagrams showing the regions of stable, weakly unstable, and strongly unstable plane waves with $q = 0$ and $q = 1$ on (δ, θ) plane are presented in Figure (3.3.12).

The corresponding bifurcation diagrams in (δ, a_0) plane are shown in Figs. 3.3.13 and 3.3.14. Note that in contrast to the unique parametrization of the plane waves with the parameter θ, in general the plane wave solution is not uniquely defined by the parameter a_0 (the frequencies ω can still be different for the same a_0), which means that the sets with $0 \leq \theta \leq \pi$ and $\pi \leq \theta \leq 2\pi$ are overlapping on the (δ, a_0) plane. Moreover, the stability properties of these two sets are not symmetric with respect to $\theta = \pi$, as shown in Figs. 3.3.13, 3.3.14, (a) and (b), respectively.

Note that the areas of weak instability for quintic CGLE in the large delay limit are consistent with the stability borders obtained numerically for $\tau = 50$ (compare the transitions from stability to instability on the branches of solutions and black dashed lines determining the boundaries in the large delay limit in Fig. 3.3.8(b)). It provides also a simple qualitative way how to predict the appearance of stable plane waves: namely, when the branches of plane waves for a finite τ appear to be in the domain of stability given in Figs. 3.3.13, 3.3.14 (dark grey shaded), then they are likely to be stable. Since the domains are independent on τ, the number of coexisting stable plane waves grows linearly with τ [108].

3.3.4. Numerical simulations

To investigate the behavior of particular plane wave solutions, e.g. the onset of destabilization and convergence to stable solutions, we have performed direct numerical integration of the delayed quintic CGLE (3.1.1) with the package ODDTool (see Appendix A). An embedded adaptive Cash-Carp scheme for time-stepping was used while the spatial derivative was treated by three-point central finite difference scheme. Periodic boundary conditions were applied, and the

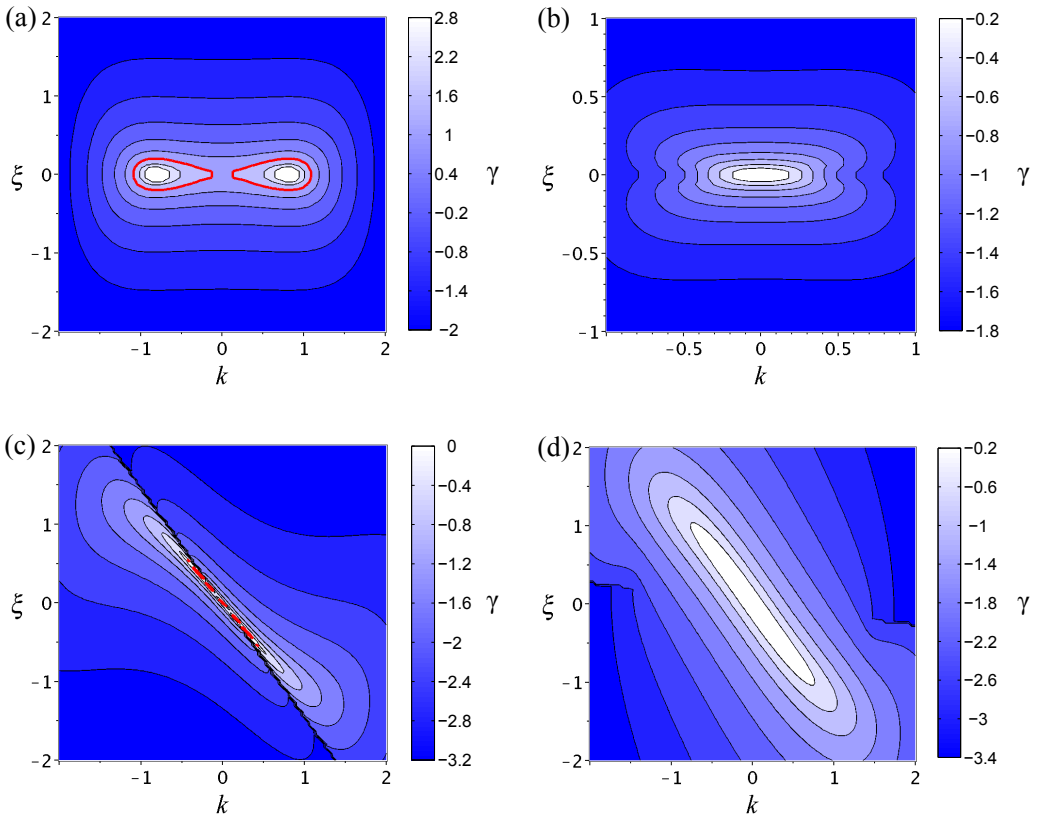

FIGURE 3.3.11. The rescaled growth rate $\gamma = \tau \mathrm{Re}[\lambda]$ of different perturbation modes (generalized dispersion relation) for different plane wave solutions. k is the spatial wavenumber of the perturbations, ξ stands for the delay induced modes. Red curves depict zero level lines. The positiveness of γ implies weak instability of the plane wave. The surface $\gamma(\xi, q)$ is obtained from Eq. (3.3.27) for different values of θ, δ, and q. (a) $\theta = 0$, $\delta = 0.5$, $q = 0$. (b) $\theta = 2$, $\delta = 1.0$, $q = 0$. (c) $\theta = 2$, $\delta = 1.0$, $q = 1$. (d) $\theta = 4$, $\delta = 1.0$, $q = 1$. Panels (b) and (d) [(a) and (c)] correspond to stable [weakly unstable] plane waves. Other parameters: $\eta = 0.2$, $\beta = 0.5$, $\epsilon = 1$, $\mu = -1$, and $\nu = -0.1$.

length of the system is chosen to include 16 spatial periods of simulated plane waves with $q = 1$. Space was discretized into 500 points, while relative tolerance for Cash-Karp scheme was set at 10^{-6}.

First, we have considered the solution starting in the vicinity of the unstable homogeneous plane wave with $q = 0$, see red point in Fig. 3.3.15(b). Fig. 3.3.15(a) shows the evolution of the amplitude, while Fig. 3.3.15(b) shows the stable plane wave (green circle), to which the solution is attracted. In the case when there are no stable plane waves for given system parameters, the solution converges to the stable homogeneous state $A = 0$.

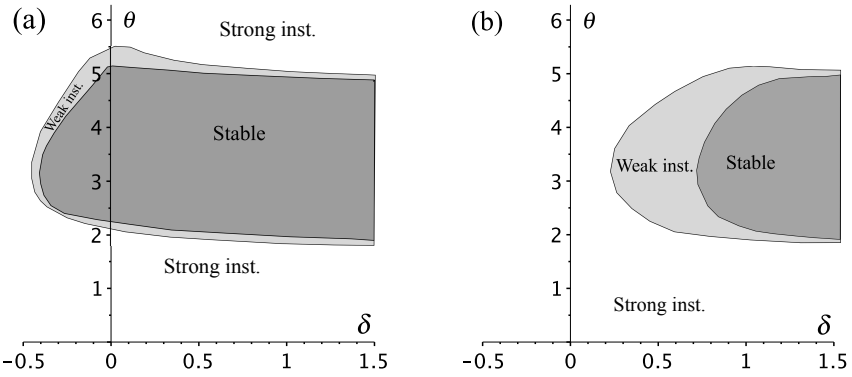

FIGURE 3.3.12. Regions of stability (dark gray), weak (light gray) and strong (white) instability for the plane waves in quintic CGLE on (δ, θ) plane. (a) $q = 0$, (b) $q = 1$. Other parameters: $\eta = 0.2$, $\beta = 0.5$, $\epsilon = 1$, $\mu = -1$, and $\nu = -0.1$.

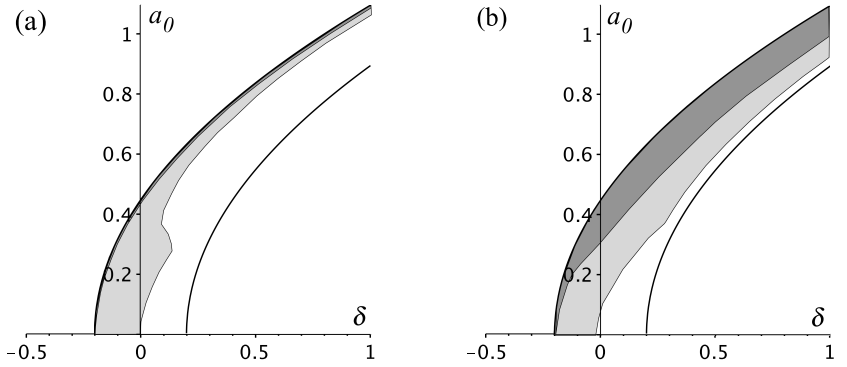

FIGURE 3.3.13. Regions of stability (dark gray), weak (light gray) and strong (white) instability for the plane waves in cubic CGLE in (δ, a_0) plane. (a) $\theta < \pi$, (b) $\theta > \pi$. Other parameters $q = 0$, $\eta = 0.2$, $\beta = 0.5$, and $\epsilon = -1$.

Transitions similar to those shown in Fig. 3.3.15 were also observed for $q \neq 0$, see Fig. 3.3.16, where two unstable plane waves with $q = 1$ were chosen as initial conditions. Figures 3.3.17(a) and (b) present the spatio-temporal evolution of the solutions corresponding to the transitions shown in Fig. 3.3.16. It is seen that the solution (a) develops defects after several delay cycles and transforms into a slightly modulated solution with lower spatial wavenumber ($q = 0.25$), which is stable for the given control parameter values. Note that for these parameter values there are no stable plane waves with the wavenumber $q = 1$. By contrast, solution (b) does not change its principal spatial wavenumber. After several delay periods of transient it converges without defects to a stable plane wave having the same wavenumber $q = 1$, see corresponding transition (b) in Fig. 3.3.16.

Now one can choose τ sufficiently large ($\tau = 50$), so that the results of asymptotic analysis obtained in the limit of large delay can be exploited. We consider a plane

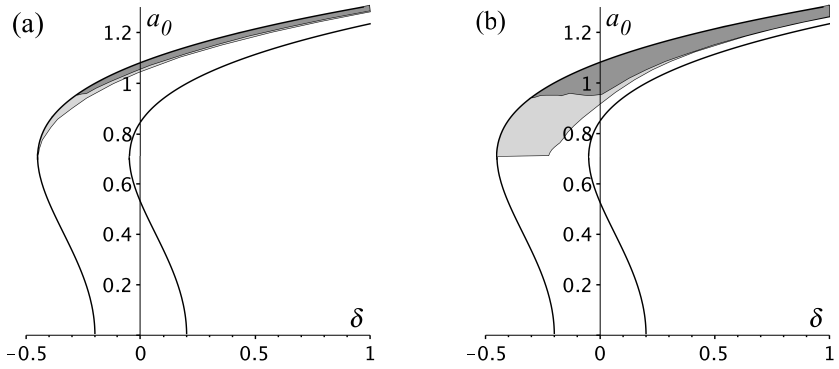

FIGURE 3.3.14. Regions of stability (dark gray), weak (light gray) and strong (white) instability for the plane waves in quintic CGLE in (δ, a_0) plane. (a) $\theta < \pi$, (b) $\theta > \pi$. Other parameters $q = 0$, $\eta = 0.2$, $\beta = 0.5$, $\epsilon = 1$, $\mu = -1$, and $\nu = -0.1$.

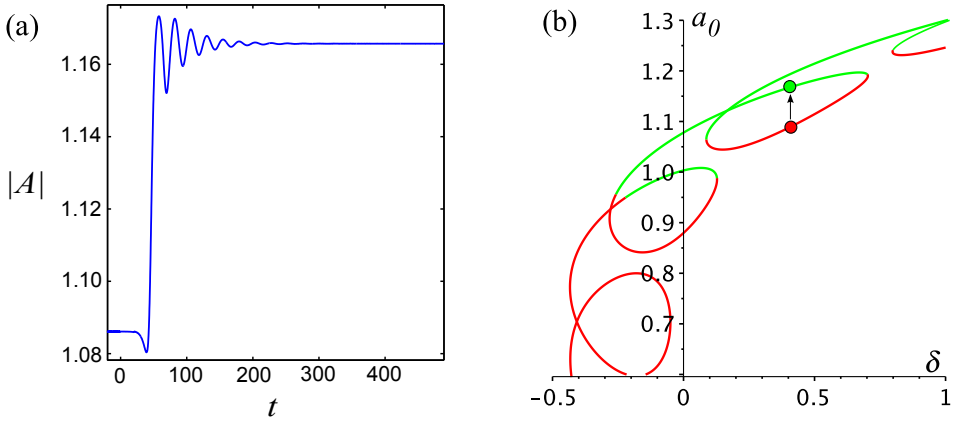

FIGURE 3.3.15. Solution starting from the neighborhood of an unstable plane wave with $q = 0$ is attracted to a stable plane wave with the same wavenumber. (a) depicts the time evolution of the amplitude a. (b) shows the corresponding transition in (δ, a_0) plane. Initial unstable solution: $\omega = 1.12$, $a_0 = 1.086$ (red circle). Resulting stable solution: $\omega = 0.998$, $a_0 = 1.166$ (green circle). System parameters: $\delta = 0.023$, $\tau = 20$, $\eta = 0.2$, $\beta = 0.5$, $\epsilon = 1$, $\mu = -1$, and $\nu = -0.1$.

wave with the control parameters from weakly unstable region on (θ, δ) plane and investigate the evolution of a small perturbation of this plane wave. Here, we expect to observe the onset of destabilization after a long period. Figure 3.3.18(a) illustrates the choice of the initial plane wave, while Fig. 3.3.18(b) shows the transient and the onset of destabilization. The solution stays close to the weakly unstable plane wave for about 80 delay time periods, and then goes away from it. Eventually, the solution is attracted to a stable plane wave with $q = 1/8$.

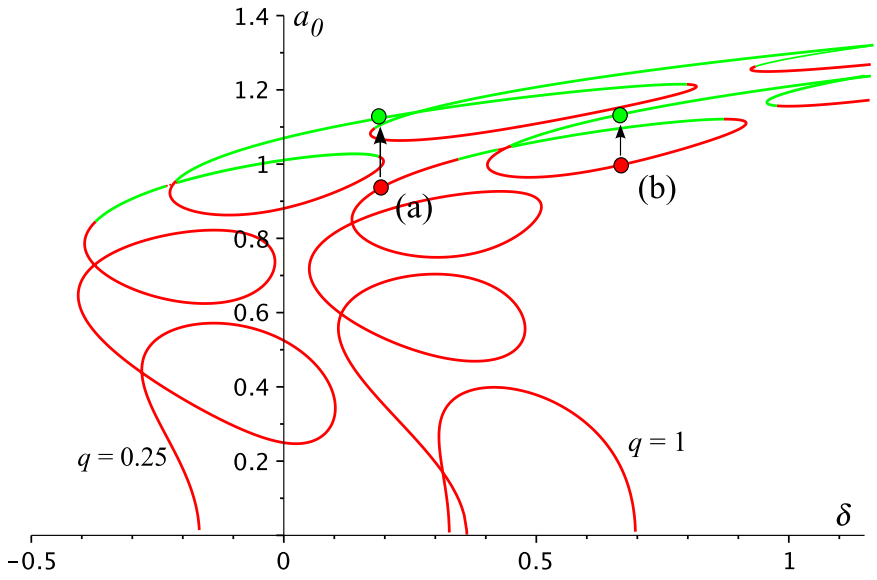

FIGURE 3.3.16. Evolution of solutions starting close to unstable plane waves with $q = 1$. Solution (a) with $\delta = 0.19$, $\omega = 0.31$, and $a_0 = 0.87$ approach the stable plane wave with different wavenumber $q = 0.25$, and $\omega = 0.969$, $a_0 = 1.12$. Solution (b) $\delta = 0.66$, $\omega = 0.5$, $a_0 = 0.99$ approaches the stable solution with the same wavenumber $q = 1$, and $\omega = 0.626$, $a_0 = 1.11$.

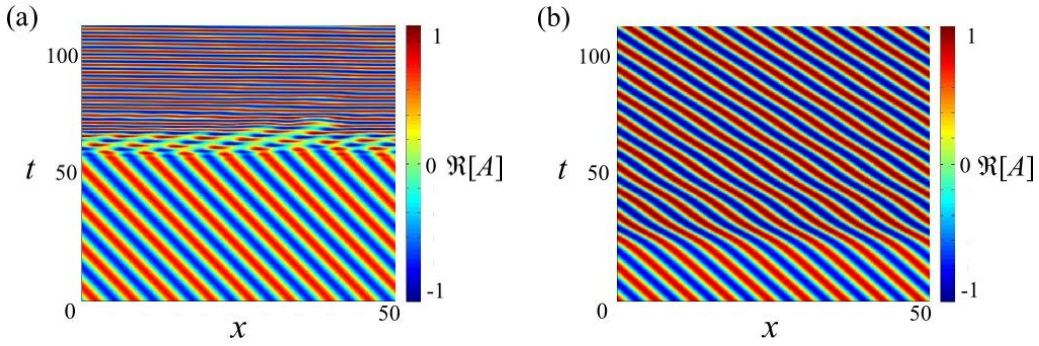

FIGURE 3.3.17. Evolution of plane waves with $q = 1$. The profile of $\Re[A]$ is shown in color. System parameters: $\tau = 20$, $\eta = 0.2$, $\beta = 0.5$, $\epsilon = 1$, $\mu = -1$, and $\nu = -0.1$. Panel (a) corresponds to the transition (a) in Fig. 3.3.16 when a defect is developed and the spatial wavenumber is changed. Panel (b) corresponds to the wavenumber-preserving transition (b) in Fig. 3.3.16 without defects.

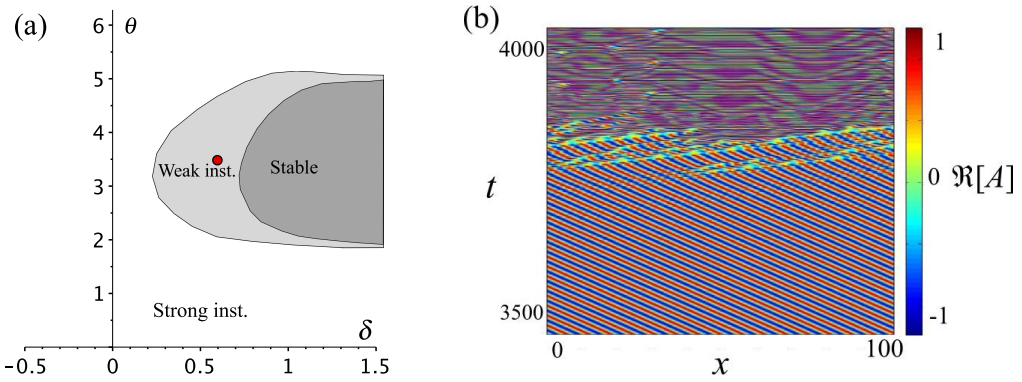

FIGURE 3.3.18. A solution started from the vicinity of a weakly unstable plane wave with $q = 1$ for large delay. The weak instability of the plane wave implies that the perturbation stays small at least several delay intervals. Initial unstable solution: $\theta = 3.94$, $\omega = 0.33$, $a_0 = 1.05$ (red circle in (a)). System parameters: $\delta = 0.56$, $\tau = 50$, $\eta = 0.2$, $\beta = 0.5$, $\epsilon = 1$, $\mu = -1$, and $\nu = -0.1$.

3.4. Discussion

In this Chapter of the Thesis the properties of plane wave solutions of cubic and cubic-quintic CGLE with delayed feedback were investigated. It was demonstrated that the delayed feedback induces a multistability of plane wave solutions with the same wavenumber q. As the gain parameter δ is varied, the branches of plane wave solutions are shown to exhibit a snaking behavior, where the frequency of the snaking oscillations is proportional to the time delay τ. Furthermore, stability properties of trivial homogeneous zero solution and plane wave solutions with different wavenumbers were investigated. The numerical bifurcation diagrams for various delay times as well as the analytical results in the limit of large delay reveal the borders of strong and weak instabilities of the plane waves. Direct numerical integration of the model equation confirms the results of analytical investigations.

To conclude, one could note that the results obtained here, especially those concerning the delay-induced multistability of plane wave solutions, open up an opportunity to extend the proposed approach to the analysis of more complex solutions of Ginzburg-Landau type equations with delay. In particular, as a natural extension of the present work, in the next Chapter of the Thesis we investigate the effect of delayed feedback on the stability properties of the localized pulse (dissipative soliton) solutions. There are some other possibilities to expand the results of this Chapter: for example, in addition to the simple additive feedback studied here, other feedback types can be considered, such as frequency-selective feedback that was shown to be useful for controlling localized structures in experiments with vertical-cavity surface-emitting lasers [113]. Another possibility is to investigate some more elaborate types of delay controls, e.g. non-local delay

control [104, 103, 114, 30]. This work is, however, out of the scope of the present Thesis.

CHAPTER 4

Delay-induced dynamics of localized structures

4.1. Introduction

As was stated in the Introduction, formation and complex dynamics of localized patterns in dissipative systems have been reported in different areas of research. They manifest themselves as localized light spots in nonlinear optics [115, 116, 117, 118, 12], solitary waves in fluid dynamics [119, 120], concentration pulses or spots in chemical and biological systems [121, 12, 18], current filaments in semiconductor devices and gas-discharge systems [13, 14, 122]. One of the established examples of localized structures are cavity solitons (CSs), which are localized spots of light in the transverse section of passive and active optical devices, broad area lasers and wide-aperture semiconductor cavities with external coherent pumping [115, 123]. Recently, much attention was paid to the investigation of the influence of the delayed optical feedback on the stability properties of these structures [96, 60, 124]. In particular, it was demonstrated that in a driven passive cavity with delayed feedback a drift instability of a cavity soliton leading to a motion in the transverse direction and some other instabilities can develop [96, 60]. The influence of the feedback phase and carrier relaxation rate on the drift instability threshold was investigated in [124]. In this Chapter, we focus on the effects of the delayed feedback on the dynamical properties of localized structures. First, in Section 2 of this Chapter we show how the delayed optical feedback produces multistability of laser cavity solitons. Moreover, we describe which types of instabilities of cavity solitons are induced by delayed feedback, including a novel type of delay induced modulational instability. In Section 3, it will be also demonstrated that the aforementioned modulational instability occurs for localized solutions in cubic-quintic complex Ginzburg-Landau equation [68]. The delay-induced dynamics in the generic Lugiato-Lefever (LL) model [125] will be described as well. The discussion on the results of this Chapter are given in Section 4.

4.2. Laser with saturable absorber and delayed feedback

4.2.1. Model equations

The dynamics of a wide-aperture laser with a saturable absorber subject to a coherent optical delayed feedback can be described by the one-dimensional quasi-optical equation [126] with an additional delayed feedback term:

$$\partial_t A = (d+i)\,\partial_{xx} A + f\left(|A|^2\right) A + \eta e^{i\varphi} A\left(x, t-\tau\right), \tag{4.2.1}$$

where $A(t, x)$ is slowly varying amplitude of the electric field; τ, η, and φ are delay time, feedback strength, and phase, respectively. Here, time t and transverse coordinate x are dimensionless, whereas $d\partial_{xx}A$ denotes a small diffusion term with a positive diffusion coefficient d. The delayed feedback term in Eq. (4.2.1) is introduced with the assumption that the external cavity is self-imaging, so that the diffraction in this cavity can be neglected [124]. Here, we focus on the case of instantaneous gain and absorption relaxation. Then the nonlinear function in Eq. (4.2.1) describing the saturable gain and absorption as well as linear cavity losses can be written in the form [127]

$$f\left(|A|^2\right) = -1 + \frac{g_0}{1 + |A|^2/s} - \frac{a_0}{1 + |A|^2}, \tag{4.2.2}$$

where g_0 and a_0 are linear gain and the absorption coefficients, and s is the ratio of the saturation intensities in the amplifying and absorbing media.

4.2.2. Localized solutions

The CS solutions can be found in the form $A(x, t) = A_0(x)e^{-i\omega t}$, where $A_0(x)$ is the complex amplitude with the field intensity $|A_0|^2$ localized around some point in space and ω is the soliton frequency shift. The properties of localized solutions of Eq. (4.2.1) without delayed feedback ($\eta = 0$) were studied previously in detail, see, e.g., [127, 128, 129]. Let us briefly recall the properties of the localized solutions in such a case. As in [127, 129], the values of the parameters $a_0 = 2.0$, $s = 10.0$, and $d = 0.1$ will be fixed for the rest of the paper. For these fixed parameter values, the branch of the single-soliton solution creates a spiral with the center P when the frequency shift ω is plotted versus the gain g_0, see Fig. 4.2.1. At the point **S** solution becomes stable via saddle-note bifurcation. Thick solid line shows the stable part of the branch. Point **H** denotes the Andronov-Hopf bifurcation with symmetric eigenfunctions. The saddle-node and Hopf points appear in a similar way on the next turn of the spiral. In what follows, the solution branch between the first fold **S** and the Andronov-Hopf bifurcation **H**, where the solution without delay is stable, will play important role leading to the emergence of multiple stable solitons in the system with feedback.

To find the localized solutions in the system with delayed feedback, one can substitute the ansatz $A_0(x)e^{-i\omega t}$ into Eq. (4.2.1) and obtain the following ordinary differential equation for unknowns A_0 and ω:

$$(d + i)\,\partial_{xx}A_0 + i\omega A_0 + f\left(|A_0|^2\right)A_0 + \eta e^{i\theta}A_0 = 0. \tag{4.2.3}$$

Here $\theta = (\omega\tau + \varphi) \mod 2\pi$ denotes the effective feedback phase. Equation (4.2.3) defines a set of soliton solutions parametrized by the phase θ. This set can be calculated in a similar way as in the system without delay, since Eq. (4.2.3) is an ordinary differential equation. In this way, one can find ω_θ and $A_{0,\theta}(x)$. Then the solitons within this set corresponding to any given value of time delay τ are determined from the condition

$$\omega_\theta\tau + \varphi = \theta \mod 2\pi. \tag{4.2.4}$$

As soon as the dependency ω_θ is calculated numerically, the solutions θ_k of Eq. (4.2.4) define the cavity solitons solutions with the frequencies ω_{θ_k} at a given

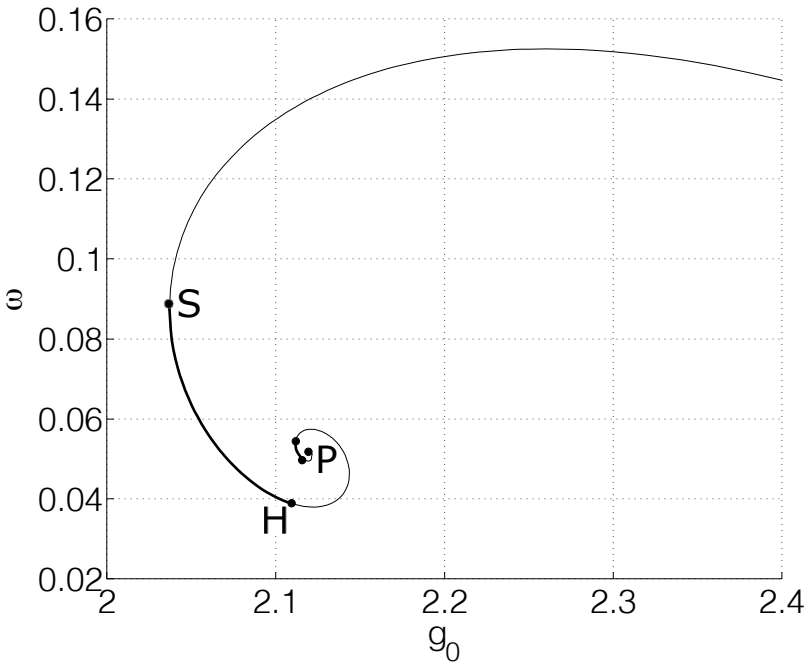

FIGURE 4.2.1. Branch of solitons as a function of the gain parameter g_0 in the case without feedback $\eta = 0$. Solid line corresponds to stable solitons. Point **S** denotes a saddle-node bifurcation, and **H** the Hopf bifurcation. The branch has the form of a spiral, and **P** denotes the winding point (center) for this spiral. Other parameters: $a_0 = 2.0$, $I_g = 10.0$, and $d = 0.1$.

value of time delay τ. Therefore, as a first step it is necessary to describe the whole set of the solitons in Eq. (4.2.3) for all possible values of the parameter θ.

It is known for the case with $\eta = 0$ [127] that the branch of CSs has a form of a spiral in the (g_0, ω)-plane [green line in Fig. 4.2.2]. Therefore, in a system perturbed by the delayed feedback $\eta > 0$, an offset spiraling branch of solitons appears in the (g_0, ω)-plane for each fixed value of the effective feedback phase θ. The set of such branches for all possible θ forms a one-parametric family in the form of a spiraling tube with a diameter proportional to η [see Fig. 4.2.2].

For any given value of delay τ, the CSs can be found from the relation (4.2.4), which defines a line on the tube. Figure 4.2.2 (black solid line) shows the resulting soliton branch for the feedback time $\tau = 250$. One can observe that the soliton branch makes a number of turns around the tube giving rise to multistability of CSs. Indeed, at the fixed value of the pump parameter g_0 and sufficiently large delay time τ, one obtains a set of external cavity solitons, similarly to the case of external CW cavity modes in a single-mode laser with delayed feedback [109, 110, 111, 112, 105, 40, 130], cf. an inset in Fig. 4.2.2 where a cross-section of the tube is presented. There, black dots depict CS solutions for $\tau = 1000$ in the (P, ω) plane, where $P = \int dx |A_0|^2$.

Similar multistability effect was experimentally observed in a broad-area VCSEL with frequency-selective feedback [62, 131]. The existence of such a multistability follows from the form of Eq. 4.2.4, which can be rewritten as $\omega_\theta = (\theta - \varphi)/\tau + 2\pi k/\tau$. Properties of its solutions can be easily studied, e.g. geometrically. In particular, one can show that the number of solutions θ_k of this equation grows linearly with τ, and, for large delay, the solutions cover the whole range of the phases θ with the spacing between them of the order $1/\tau$, cf. [105, 130]. In particular, in the limit of large delay, the CS solutions fill the whole surface of the tube densely.

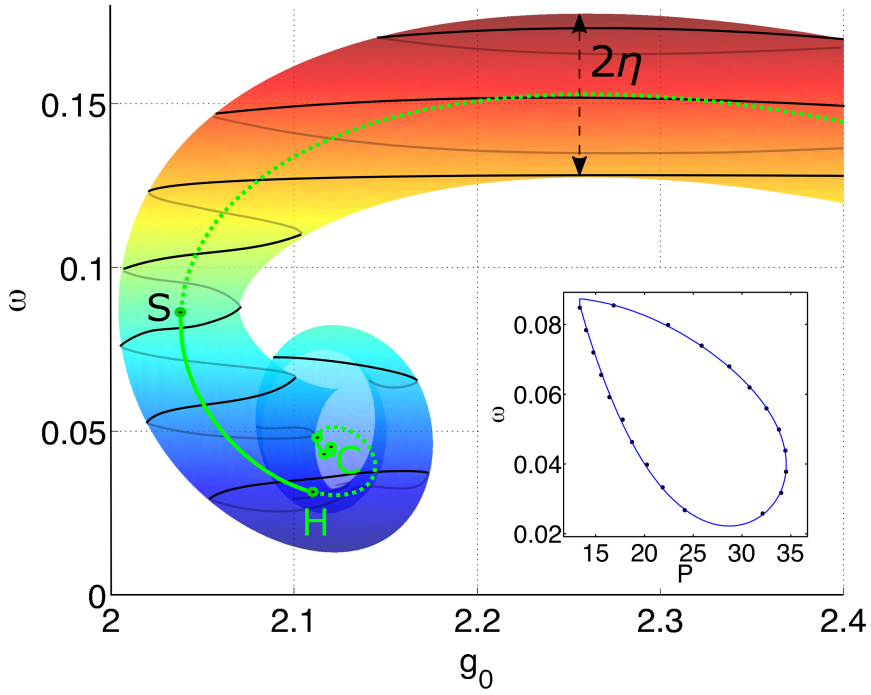

FIGURE 4.2.2. Tube of solitons defined by Eq. (4.2.3) for all possible values of phase θ and other parameters fixed as $\eta = 0.025$, $\varphi = 0$, $a_0 = 2.0$, $I_g = 10.0$, and $d = 0.1$. The tube corresponds to all possible values of the delay time τ. Black line: soliton branch for $\tau = 250$. Green (light gray) line: branch of solitons for the case without feedback, $\eta = 0$ (solid for stable and dashed for unstable). **S** indicates a saddle-node bifurcation, and **H** an Andronov-Hopf bifurcation. The branch has the form of a spiral with the accumulation point **C**.

4.2.3. Stability of localized solutions

To analyze the stability of the localized solutions in the presence of delayed feedback, one can apply the ansatz $A(x,t) = (A_0(x) + A_p(x,t))\, e^{-i\omega t}$ in the evolution equation (4.2.1). Here, A_p stands for a small perturbation of the soliton solution.

After linearization in A_p, we obtain

$$\begin{aligned}(4.2.5)\qquad \partial_t A_p &= -i\omega A_p + (d+i)\,\partial_{xx} A_p + \\ &+ f\left(|A_0|^2\right) A_p + |A_0|^2 f'\left(|A_0|^2\right) A_p + \\ &+ {A_0}^2 f'\left(|A_0|^2\right) \overline{A_p} + \eta e^{i\theta} A_p(t-\tau).\end{aligned}$$

By substituting $A_p(x,t) = (A_R(x) + iA_I(x))\, e^{\lambda t}$ into Eq. (4.2.5), where λ is the complex eigenvalue, one can arrive at the transcendental eigenvalue problem

$$(4.2.6)\qquad L\Psi := [\tilde{L} - I\lambda + \eta B e^{-\lambda\tau}]\Psi = 0,$$

where $\Psi = (A_R, A_I)^T$ is an eigenfunction, $\tilde{L}$ is the linearization of the instantaneous part around the solution $(A_{0R}, A_{0I})^T = (\mathrm{Re}A_0(x), \mathrm{Im}A_0(x))^T$

$$\tilde{L} = \begin{pmatrix} d\frac{\partial^2}{\partial x^2} + f\left(|A_0|^2\right) + & -\omega - \frac{\partial^2}{\partial x^2} + \\ +2f'\left(|A_0|^2\right) A_{0R}^2 & +2f'\left(|A_0|^2\right) A_{0R}A_{0I} \\ \omega + \frac{\partial^2}{\partial x^2} + & d\frac{\partial^2}{\partial x^2} + f\left(|A_0|^2\right) + \\ +2f'\left(|A_0|^2\right) A_{0R}A_{0I} & +2f'\left(|A_0|^2\right) A_{0I}^2 \end{pmatrix},$$

and

$$B = \begin{pmatrix} \cos\theta & -\sin\theta \\ \sin\theta & \cos\theta \end{pmatrix},$$

which is a 2×2 matrix of rotation by angle θ.

To find the eigenvalues numerically, the eigenvalue problem (4.2.6) is rewritten in matrix form by discretizing the space. The characteristic roots of the resulting system are found using the spectral method described in [132], see Fig. 4.2.4. With the increase of delay time τ, the computational complexity of the eigenvalue problem increases. However, as it is shown below, in such a case, the stability analysis can be significantly simplified by using the large delay approximation.

4.2.3.1. *Drift bifurcation*

Due to translational and phase shift symmetries of Eq. (4.2.1), the operator L has two zero eigenvalues corresponding to a pair of eigenfunctions (also known as Goldstone modes) [129]: even phase shift neutral mode $\Psi^{ph} = (-\mathrm{Im}A_0(x), \mathrm{Re}A_0(x))^T$ and odd translational neutral mode $\Psi^{tr} = \partial_x(\mathrm{Re}A_0(x), \mathrm{Im}A_0(x))^T$. The real eigenvalue which corresponds to Galilean symmetry [1-7] is generally non-zero due to diffusion and delayed feedback. Drift bifurcation occurs when the eigenvalue corresponding to the translational mode becomes doubly degenerate with geometrical multiplicity one [133]. That is, the critical real eigenvalue passes through zero at the bifurcation point, so that the corresponding critical eigenfunction at this point is proportional to Ψ^{tr}. This critical eigenvalue can be either a delay-induced branch of zero translational eigenvalue or correspond to Galilean mode. To determine the drift instability threshold let us look for real solutions of the eigenvalue problem (4.2.6) in the vicinity of zero, $\lambda = \varepsilon \ll 1$. The corresponding eigenfunction Ψ can be represented as $\Psi = \Psi^{tr} + \varepsilon\Psi_1 + \mathcal{O}(\varepsilon^2)$ with some unknown function Ψ_1. Substituting this expansion into Eq.(4.2.6), expanding the

resulting equation into power series in ε, and collecting zero order terms one can get the relation $L_0\Psi^{tr} = 0$ with $L_0 = \tilde{L} + \eta B$, which is satisfied by the definition of the neutral mode Ψ^{tr}. Then, collecting the first order terms in ε we obtain

$$L_0\Psi_1 = (I + \eta\tau B)\Psi^{tr}. \tag{4.2.7}$$

According to the Fredholm alternative (9), this equation possesses a nontrivial solution if and only if the solvability condition is fulfilled which requires the orthogonality of the right hand side to the translational eigenfunction $\Psi^{tr\dagger}$ of the adjoint operator $L_0^\dagger$. The solvability condition leads to the expression

$$\eta_d = -p/\left[\tau\left(p\cos\theta - q\sin\theta\right)\right] \tag{4.2.8}$$

for the threshold feedback rate associated with the drift instability of the cavity soliton. Here $p = \langle\Psi_R^{tr}, \Psi_R^{tr\dagger}\rangle + \langle\Psi_I^{tr}, \Psi_I^{tr\dagger}\rangle$ and $q = \langle\Psi_I^{tr}, \Psi_R^{tr\dagger}\rangle - \langle\Psi_R^{tr}, \Psi_I^{tr\dagger}\rangle$, where $\Psi = (\Psi_R^{tr}, \Psi_I^{tr})^T$ ($\Psi^{tr\dagger} = (\Psi_R^{tr\dagger}, \Psi_I^{tr\dagger})^T$) is the translational neutral mode of L_0 (adjoint operator $L_0^\dagger$) and inner product is defined by $\langle\Psi_j, \Phi_k^\dagger\rangle = \int_{-\infty}^{\infty}\Psi_j\Phi_k^\dagger dx$. Note that in this case for the solvability condition the standard L_2 inner product can be used since the operator L_0 does not contain the delayed part [60, 96, 124]. The same relation (4.2.8) can be obtained from the orthogonality condition of the generalized eigenfunction Φ^{tr}, which satisfies the equation $L_0\Phi^{tr} = \Psi^{tr}$, and the adjoint neutral mode $\Psi^{tr\dagger}$ with the bilinear form introduced in the preliminary Chapter 2 and defined in [64, 65, 134].

When increasing the feedback rate above the threshold given by (4.2.8), a pitchfork bifurcation takes place: the stationary soliton looses stability giving rise to a pair of branches of stable cavity solitons moving uniformly along the x-axis in opposite directions. Note that the drift instability exists only in the interval of feedback phases θ, where the right hand side in Eq. (4.2.8) is positive. Drift instability threshold calculated for $\tau = 1000$ is shown by solid red line in Fig. 4.2.3. The domain where drift instability is possible for arbitrary delay time is indicated by horizontal hatching.

4.2.3.2. *Saddle-node phase bifurcation*

Similarly to the translational zero eigenvalue, the zero eigenvalue of the phase shift neutral mode can become doubly degenerate in the presence of delayed feedback. Threshold of this instability η_p is given by Eq. (4.2.8) with the neutral modes Ψ^{tr} and $\Psi^{tr\dagger}$ replaced by the phase shift neutral modes Ψ^{ph} and $\Psi^{ph\dagger}$ in the expressions for the coefficients p and q. In Fig. 4.2.3 it is shown by a dashed green line. In fact, this bifurcation corresponds to a saddle-node bifurcation, where a pair of soliton solutions merge and disappear (cf. Fig. 4.2.2), and it is defined by the condition $d\omega/d\theta = 1/\tau$, which follows directly from Eq. (4.2.4). By differentiating Eq. (4.2.3) by θ one can easily show that this condition is equivalent to the condition $\eta = \eta_p$ obtained from Eq. (4.2.8) with the translational neutral mode replaced by the phase one. That is, the aforementioned multistability of the CSs is induced by the saddle-node phase bifurcation.

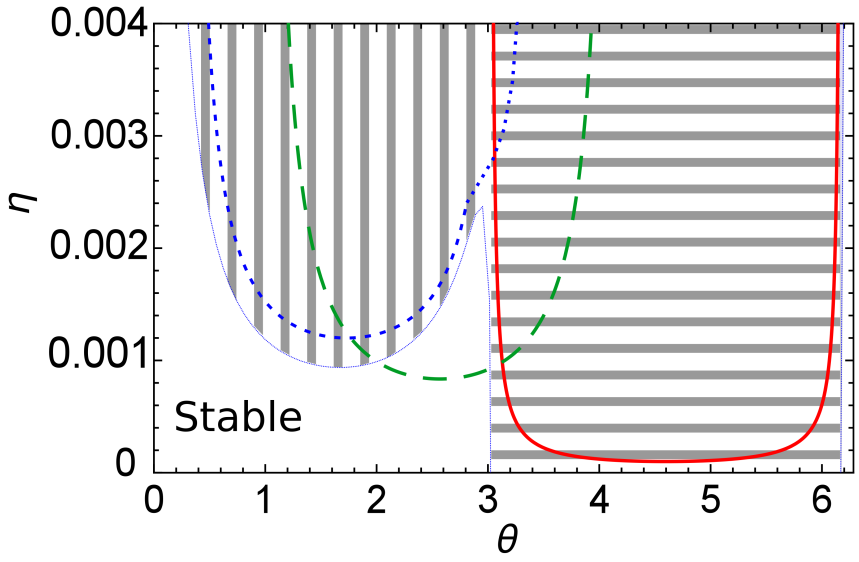

FIGURE 4.2.3. Cavity soliton bifurcation diagram in (θ, η)-plane. In the large delay limit, horizontally hatched region corresponds for the drift destabilization and vertically hatched region to modulational instability related to the translational neutral mode. Solid red, dotted blue, and dashed green lines show the destabilization threshold for drift, modulational, and phase instabilities, respectively, calculated for $\tau = 1000$. Control parameter $g_0 = 2.07$.

4.2.3.3. *Modulational instability*

It was shown in [77, 57, 78] that the spectrum of the delay systems is split into discrete and pseudo-continuous parts in the case when the delay time is sufficiently large to induce multiple delay-induced linear modes. While the aforementioned drift instability is associated with the discrete part of the spectrum, an instability of the pseudo-continuous part can produce another type of bifurcation scenario. Figure 4.2.4 shows a set of eigenvalues belonging a branch of pseudo-continuous spectrum with the translational zero eigenvalue at the origin. The panels (a) and (b) correspond to weakly stable and unstable case, respectively, indicating the presence of delay-induced modulational instability [76]. The modulational instability is characterized by a branch of eigenvalues whose second derivative becomes positive in the origin as in Fig. 4.2.4(b).

In order to obtain the conditions for the onset of a modulational instability, let us consider the pair of complex conjugate eigenvalues $\lambda_\pm$ with smallest nonzero imaginary parts on the pseudo-continuous branch. The long-wavelength modulational instability takes place when this pair crosses the imaginary axis. In the limit of large delay times, the distance between the imaginary parts of the neighboring eigenvalues on the pseudo-continuous branch shown in Fig. 4.2.4 becomes close to $\epsilon = 2\pi/\tau$ [77, 78], the eigenvalues $\lambda_\pm$ can be expanded in power series in the small parameter ϵ as $\lambda_\pm = \pm i\epsilon\,[1 + \nu\epsilon/(2\pi)] + \gamma_{\pm 2}\epsilon^3/(2\pi) + ...$, where ν is

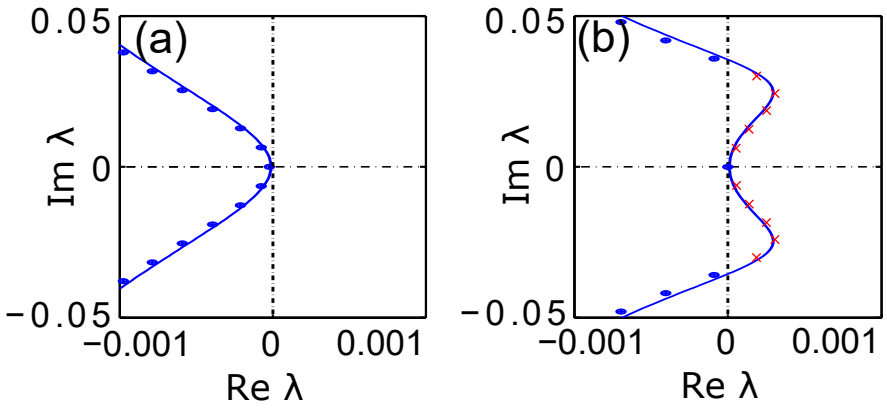

FIGURE 4.2.4. Pseudo-continuous spectrum curves for $\eta = 0.005$. Stable soliton (a) for $\theta = 4$ and modulationally unstable soliton (b) for $\theta = 1.5$. Blue dots and red crosses show stable and unstable eigenvalues for $\tau = 1000$.

real, since the second order derivative along the branch vanishes at the bifurcation point. Here we have used the fact that λ_- and λ_+ are complex conjugated. Substituting this expansion into the eigenvalue problem (4.2.6), representing the unknown eigenfunctions in the form $\Psi = \Psi^{tr} + \epsilon\Psi_1 + \epsilon^2\Psi_{\pm 2} + ...$, and collecting first order terms in ϵ we obtain a linear equation for the first order correction Ψ_1:

$$L_0\Psi_1 = (I + \nu\eta B)\Psi^{tr}. \tag{4.2.9}$$

Next, collecting the terms of the order ϵ^2 and applying solvability condition to the resulting equation, one can obtain the third order corrections to the real parts of $\lambda_\pm$, which lead to the following condition for the modulational instability threshold:

$$\eta_m = p^2 / \left[2\sin\theta(qP - pQ)\right]. \tag{4.2.10}$$

Here the coefficients P and Q are calculated using the same formulas as those for p and q, but with Ψ^{tr} replaced by the first order correction Ψ_1 obtained by solving Eq. (4.2.9). In contrast to p and q, the coefficients P and Q depend on the phase θ. The modulational instability shown with the dashed blue line in Fig. 4.2.3 gives rise to a sequence of Andronov-Hopf bifurcations taking place above the threshold defined by Eq. (4.2.10). One can see that Eq. (4.2.10) obtained in the limit of large delay provides a reasonable approximation for the Andronov-Hopf bifurcation threshold calculated at $\tau = 1000$. The latter threshold is indicated with dotted blue line in Fig. 4.2.3.

Figure 4.2.5 shows zigzagging motion of the soliton after the onset of both drift and modulational delay-induced instabilities. The period of oscillations is close to the delay time τ. Figure 4.2.5(a) presents a soliton with periodically varying velocity $V_1(t)$ having positive average value $\bar{V}_1 > 0$. It is worth to notice that qualitatively similar zigzagging motion was observed numerically in a model of vertical cavity semiconductor laser with frequency-selective feedback [135]. Due to the symmetry properties of the problem this periodic regime coexists with

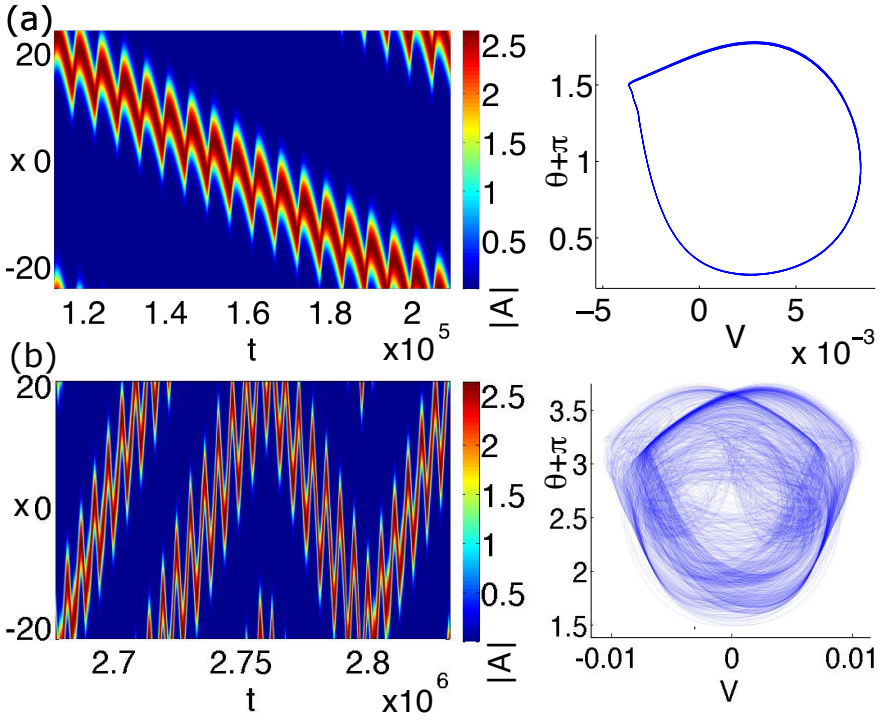

FIGURE 4.2.5. Zigzagging solitons appearing above the drift and modulational instability thresholds. (a) - regime with periodic in time velocity, $\varphi = -1.0$ (b) - aperiodic regime, $\varphi = 0.0$. On the right: phase portraits of zigzagging solitons in coordinates V (soliton center velocity) and θ (feedback phase). Other parameters: $\tau = 5000, \eta = 0.002$.

another stable periodic regime having exactly opposite velocity $V_2(t) = -V_1(t)$. With the increase of the parameter φ both periodic regimes are transformed into aperiodic solutions which finally merge into a single chaotic attractor. Figure 4.2.6 shows the transition to chaos via period-doubling bifurcations with the increase of the phase of the delayed feedback φ. A period-doubling transition to chaos leads to the attractor, which corresponds to a zigzagging soliton changing the direction of motion aperiodically after large time intervals, see Fig. 4.2.5(b). Surprisingly, the time intervals between these changes of the direction of the soliton motion are much larger than the delay time or any other system timescale.

4.3. Other spatially extended systems with delayed feedback

4.3.1. Cubic-quintic CGLE with delayed feedback

In this section, it will be demonstrated that the delay induced modulational instability, which is similar to that described above, can destabilize localized solution of cubic-quintic complex Ginzburg-Landau equation (CGLE). CGLE plays an important role in modeling of various natural phenomena including nonlinear optical waves, second-order phase transitions, Rayleigh-Bénard convection, and

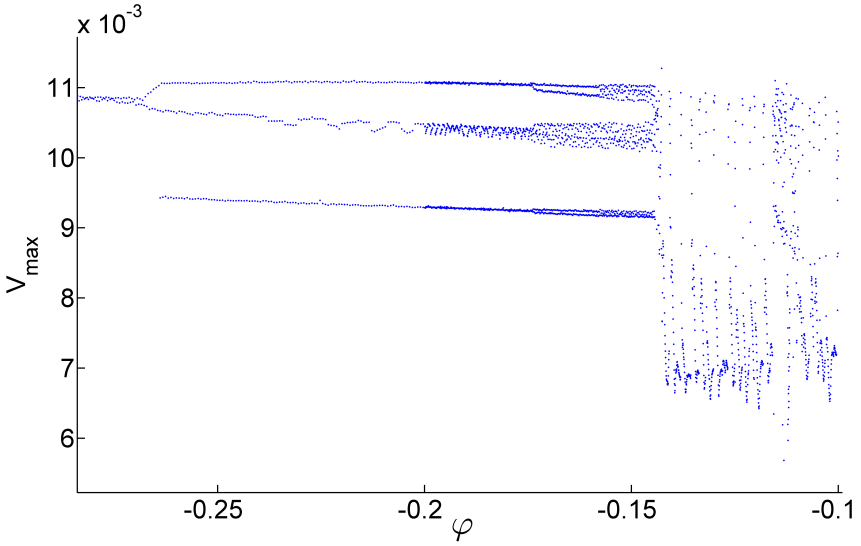

FIGURE 4.2.6. Maximum of the soliton velocity V_{max}. Control parameter is feedback phase φ. Other parameters: $\tau = 5000$ and $\eta = 0.002$.

superconductivity [86, 87]. Its universality is ensured by the fact that CGLE is an amplitude equation describing the onset of instability near an Andronov-Hopf bifurcation in spatially extended dynamical systems [66]. In nonlinear optics, equations of CGLE type are widely used to describe such phenomena as mode-locking in lasers [88, 89, 90], short pulse propagation in optical transmission lines [91], dynamics of multimode lasers, and transverse pattern formation in nonlinear optical media [129, 93].

Here we consider one-dimensional cubic-quintic CGLE with delayed feedback (see Chapter 3 of the Thesis). In this case the equation for the complex amplitude $A(x,t)$ reads:

$$\begin{aligned} \partial_t A &= \left(d + \frac{i}{2}\right) \partial_{xx} A + \delta A + (\epsilon + i)\,|A|^2 A + \\ &+ (\mu + i\nu)\,|A|^4 A + \eta e^{i\varphi} A(x, t-\tau). \end{aligned} \tag{4.3.1}$$

Here the parameter $d > 0$ is the diffusion coefficient, diffraction (second-order dispersion) coefficient is scaled to $1/2$, and δ describes the linear loss or gain. Parameters ϵ, μ, and ν determine the shape of the nonlinearity.

Stable localized solutions are found in the range of parameters described in, e.g., [88]. We consider a stable localized solution for the following parameter values: $d = 0.5, \delta = -0.1, \epsilon = 0.5, \mu = -0.1$, and $\nu = -0.1$. With the addition of the delayed feedback, modulational instability can develop as it is illustrated by Figure 4.3.1, where pseudo-continuous spectrum curves for $\eta = 0.09$, $\theta = 5.8$, and $\tau = 1000$, corresponding to modulationally unstable localized solution, are shown.

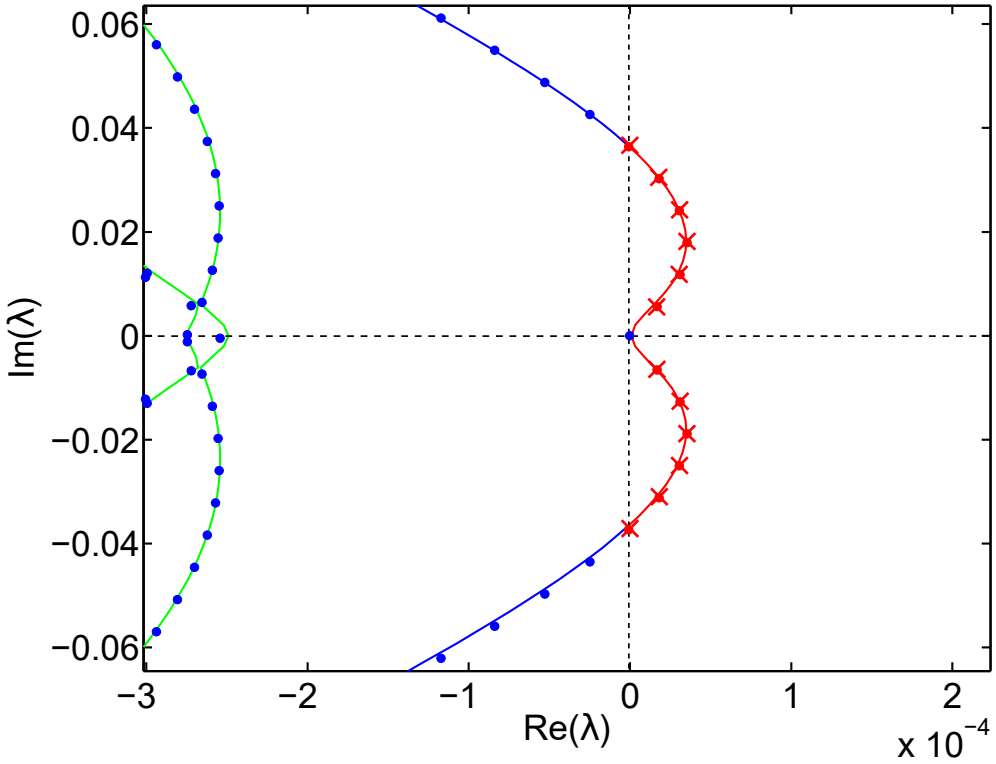

FIGURE 4.3.1. Pseudo-continuous spectrum curves for $\eta = 0.09$, $\theta = 5.8$, and $\tau = 1000$. Localized solution exhibits delay-induced modulational instability of the same type as in the model of a laser with a saturable absorber. Blue dots and red crosses show stable and unstable eigenvalues for $\tau = 1000$.

4.3.2. Lugiato-Lefever model with time-delayed feedback

In this section, the aim is to analyze the impact of the delayed feedback on the CS dynamics in the generic Lugiato-Lefever (LL) model [125]. This model describes the appearance of either spatial [136, 137] or temporal [138] localized structures in nonlinear cavities as well as the interaction between such structures [139]. The important feature which separates it from previously investigated CGLE and laser with saturable absorber models is the inclusion of the injection term. As for the previous models, the optical delayed feedback is implemented in the LL model by considering a self-imaged external cavity and a single roundtrip delay term [96, 140], i. e.

$$\frac{\partial E}{\partial t} = i\nabla_\perp^2 E - (1 + i\theta)E + i|E|^2 E + E_i + \eta e^{i\phi} E(t - \tau). \tag{4.3.2}$$

Here E is the normalized amplitude of the electric field and θ is the frequency detuning between the injected light E_i and the cavity resonance. E_i is considered as being real without loss of generality. The feedback is characterized by the

time-delay τ, feedback strength η and phase ϕ. Homogeneous steady state (HSS) solutions E_S of Eq. (4.3.2) are found by setting the time derivatives and Laplacian equal to zero

$$-(1+i\theta)E_S + i|E_S|^2E_S + E_i + \eta e^{i\phi}E_S = 0, \tag{4.3.3}$$

which results in an implicit equation for $I_S = |E_S|^2$:

$$I_i = I_S\{[1-\eta\cos\phi)]^2 + [I_S - \theta + \eta\sin\phi]^2\}, \tag{4.3.4}$$

where $I_i = E_i^2$. Depending on choice of θ the curve $I_S(I_i)$ for the case of no feedback ($\eta = 0$) is either monostable ($\theta < \sqrt{3}$) or bistable ($\theta > \sqrt{3}$) [136]. The optical feedback strongly impacts the shape of this curve by both its magnitude and phase and changes the condition for bistability as $(\theta - \eta\sin\phi)^2 > 3(1 - \eta\cos\phi)^2$. This condition follows from the expression for the saddle-node (fold) bifurcation on the HSS $dI_i/dI_S = 0$ leading to

$$I_S^{SN_{h1,2}} = \frac{2(\theta - \eta\sin\phi)}{3} \pm \frac{1}{3}\sqrt{(\theta - \eta\sin\phi)^2 - 3(1-\eta\cos\phi)^2}. \tag{4.3.5}$$

For the monostable case Eq. 4.3.5 represents the inflection point of the $I_S(E_i)$ curve. Examples of the impact of the optical feedback on the shape of the $I_S(E_i)$ curve are shown in Fig. 4.3.2.

The linear stability of the HSS is analyzed by considering small fluctuations around this state that are modulated with transverse wave vector k ($k = k_x$ in the 1D case and $k = (k_x, k_y)$ in the 2D case)

$$\begin{bmatrix} \delta E(r_\perp, t) \\ \delta E^*(r_\perp, t) \end{bmatrix} = e^{(\lambda t + ik\cdot r)} \begin{bmatrix} \delta E \\ \delta E^* \end{bmatrix}. \tag{4.3.6}$$

Plugging this expression in Eq. 4.3.2 and its complex conjugate and linearizing with respect to the small fluctuations around the HSS results in the following equation for the eigenvalue λ

$$\det \begin{pmatrix} \lambda + A_r + iA_i + ik^2, & -iE_S^2 \\ iE_S^{*2}, & \lambda + A_r - iA_i - ik^2 \end{pmatrix} = 0, \tag{4.3.7}$$

where

$$A_r = 1 - \eta e^{-\lambda\tau}\cos\phi,$$
$$A_i = \theta - 2I_S - \eta e^{-\lambda\tau}\sin\phi.$$

Without delayed feedback, the characteristic equation 4.3.7 is quadratic and, therefore, the eigenvalues are a pair of complex conjugated numbers. As a result, four bifurcation scenarios may occur. When the eigenvalues are purely real and one of them changes sign from negative to positive, this unstable eigenvalue could correspond either to zero, $k^2 = 0$, or to nonzero wavenumber, $k^2 > 0$. In the first case the saddle-node bifurcations appear, which correspond to the turning points of the bistable curve and imply that the part of this curve having negative slope is always unstable. The second case indicates the onset of Turing-like instability

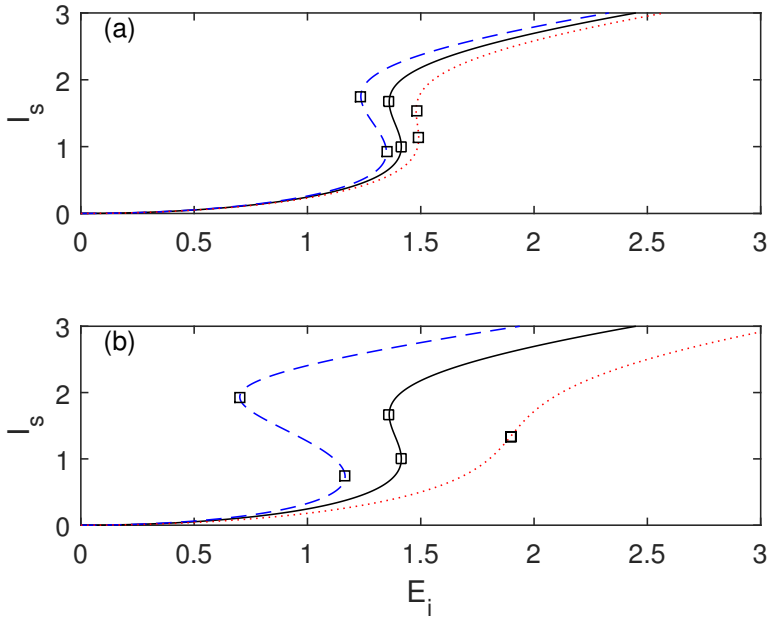

FIGURE 4.3.2. Steady state branches of the homogeneous solution of Lugiato-Lefever model (Eq. 4.3.2) for $\theta = 2$ and different phases of the optical feedback: $\phi = 0$ (dashed blue line) and $\phi = \pi$ (dotted red line). Top (bottom) panel corresponds to the feedback strength $\eta = 0.1$ ($\eta = 0.5$). Black solid lines in two panels are obtained for the case without optical feedback. Saddle-node bifurcations (Eq. 4.3.5) are denoted by $\square$ and coincide with the onset of the Turing instability $I_S^{T(k^2=0)} = I_S^{SN_{h1,2}}$ for the limit $k^2 \to 0$ (c.f. Eq. 4.3.9).

giving rise to a patterned state. Similarly, when the real part of a pair of complex eigenvalues becomes positive for $k^2 = 0$, an Andronov-Hopf bifurcation of the HSS occurs, while, for $k^2 > 0$, a traveling wave instability develops giving rise to a travelling pattern.

With delayed optical feedback, the eigenvalues λ of Eq. 4.3.7 are not anymore determined by simple solutions of a quadratic equation because in this case both A_r and A_i depend on λ via the exponent in the feedback term. In general, Eq. 4.3.7 is solved numerically by finding λ for each given k^2.

The case of Turing instability can be treated analytically: inserting $\lambda = 0$ in Eq. 4.3.7 results in a quadratic equation for k^2 with solutions

$$k^2 = -\theta + 2I_S + \eta \sin\phi \pm \sqrt{I_S^2 - (1 - \eta\cos\phi)^2}. \tag{4.3.8}$$

Here the existence of real solutions for the wave vector k indicates the presence of Turing instability. From Eq. 4.3.8 one can see that in the limit when marginally stable eigenvalues of the Turing instability tend to zero, $k^2 \to 0$ one can recover

the conditions of the saddle-node bifurcations, see Eq. 4.3.5, i.e.

$$I_S^{T(k^2=0)} = I_S^{SN_{h1,2}}. \tag{4.3.9}$$

The dependence of the wave vector square k^2 on the intensity of the steady state electric field intensity I_S as obtained from Eq. 4.3.8 is shown in Fig. 4.3.3 for a feedback strength of $\eta = 0.1$ (top panel) and $\eta = 0.5$ (bottom panel) and different feedback phases.

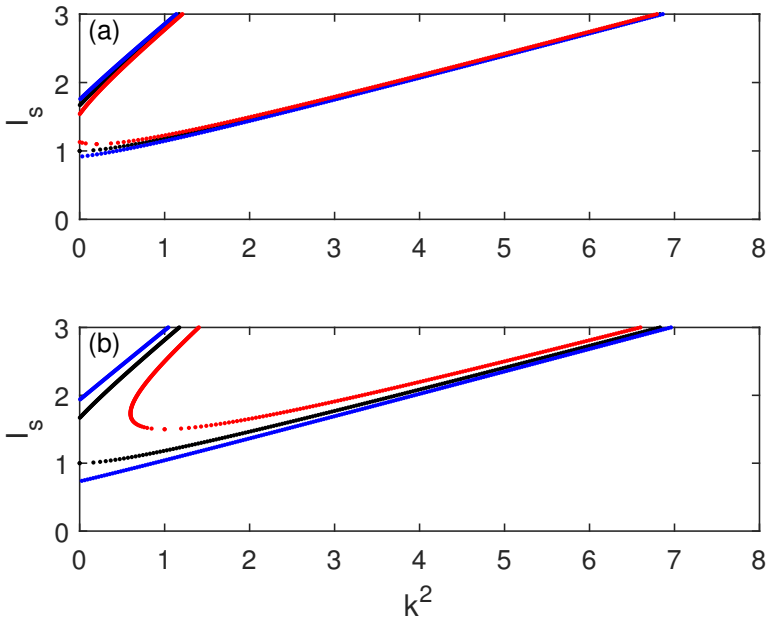

FIGURE 4.3.3. Wave vector square k^2 at the onset of modulation instabilities (real eigenvalue $\lambda = 0$) as a function of the steady state intensity I_S for different phase of the optical feedback: $\phi = 0$ (blue dotted curve) and $\phi = \pi$ (red dotted curve). Top panel is for feedback strength of $\eta = 0.1$ and the bottom panel is for $\eta = 0.5$ (see Fig. 4.3.2). Black dotted curves in the two panels are for the case without optical feedback.

As can be seen from Fig. 4.3.3, the $k^2 = 0$ points coincide with the turning points of the bistable curve and the inflection point of the monostable curve (see Eq. 4.3.9). The upper branch is always Turing unstable for the parameters of Fig. 4.3.3.

A map of the saddle-node bifurcation in the $\theta - E_i$ plane is shown in Fig. 4.3.4. As θ increases, the bistable region widens, however, it is strongly influenced by the phase of optical feedback being much larger for $\phi = 0$ than for $\phi = \pi$. Such profound effect of the feedback phase on the bistable region has been previously observed when studying cavity soliton dynamics in VCSEL [140].

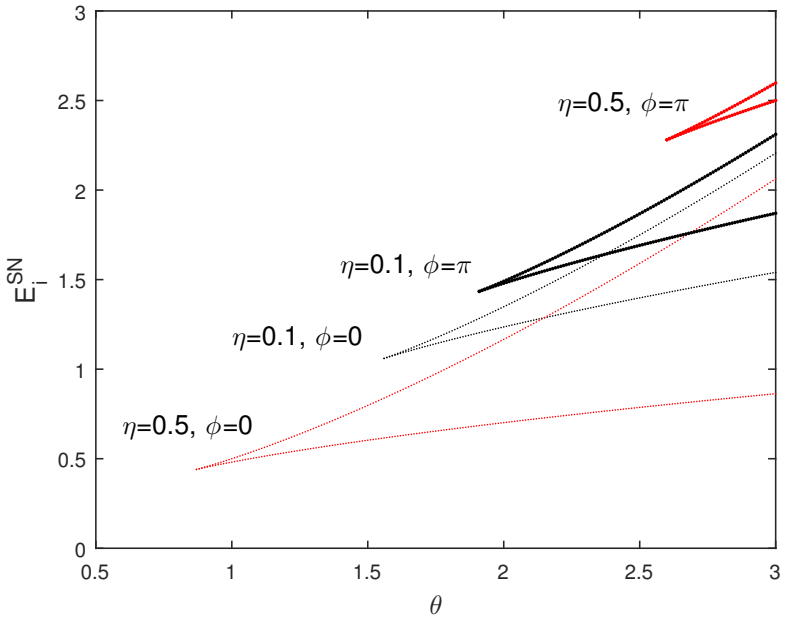

FIGURE 4.3.4. Maps of the saddle-node bifurcations in the $\theta - E_i$ plane. Black (red) curves are for $\eta = 0.1$ ($\eta = 0.5$) and small (large) dots are for feedback phase $\phi = 0$ ($\phi = \pi$).

As demonstrated before, the delayed feedback may create new Andronov-Hopf bifurcations in the system due to the exponential term $e^{-\lambda\tau}$ in Eq. 4.3.7. Indeed, it has been shown that feedback-induced Andronov-Hopf bifurcations are responsible for time-periodic and eventually more complex dynamics of cavity solitons in VCSEL with saturable absorber [141]. In order to identify such bifurcations one can solve Eq. 4.3.7 for $k^2 = 0$. An example of appearance of such a feedback-induced Andronov-Hopf bifurcation is presented in Fig. 4.3.5 for the case of $\eta = 0.5$, $\tau = 10$ and $\phi = \pi/3$.

A map of the saddle-node and Andronov-Hopf bifurcations in Lugiato-Lefever model in the plane of (E_i, η) for fixed feedback phase of $\phi = \pi$ and $\tau = 10$ is shown in Fig. 4.3.6. When increasing the feedback strength, the bistable region delimited by the two saddle-node (fold) bifurcation lines disappears while a region located between the two Andronov-Hopf lines appears and broadens.

Traveling wave (TW) bifurcation occurs when the Andronov-Hopf bifurcation takes place at nonzero k^2. In a similar manner as when arriving at Eq. 4.3.8, one can express analytically k^2 as a solution of the quadratic equation obtained from the real part of Eq. 4.3.7 at a fixed I_S and $\lambda = i\Omega$. Plugging this solution in the equation for the imaginary part of Eq. 4.3.7 (the resulting equation is too long to be presented here) provides an one-parameter implicit equation for Ω. In such a way one can follow semi-analytically the TW bifurcations in the parameter space: an example of the TW instability is shown in Fig. 4.3.7 for $\eta = 0.5$ and $\phi = \pi/3$.

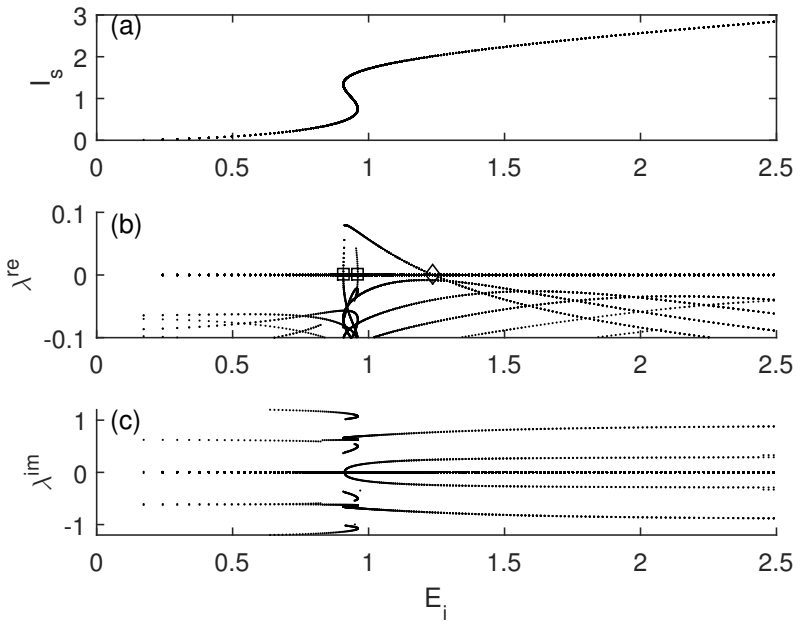

FIGURE 4.3.5. Time-delayed feedback-induced Andronov-Hopf bifurcation in Lugiato-Lefever model (4.3.2) for $\eta = 0.5$, $\tau = 10$ and $\phi = \pi/3$. (a) Homogeneous steady-state solution $I_S(E_i)$; (b) real and (c) imaginary parts of the eigenvalues calculated from Eq. 4.3.7 for $k^2 = 0$. Saddle-node and Andronov-Hopf bifurcations are denoted by $\square$ and $\Diamond$, respectively.

Spatial dynamics

Stationary CS and periodic patterns are given by the solutions of Eq. 4.3.2 with $dE/dt = 0$, i.e. by solving the system of four first order ordinary differential equations:

$$\begin{aligned} \tfrac{du_1}{dx} &= u_3 \\ \tfrac{du_2}{dx} &= u_4 \\ \tfrac{du_3}{dx} &= (T - I)u_1 + Pu_2 \\ \tfrac{du_4}{dx} &= -Pu_1 + (T - I)u_2 + E_i, \end{aligned} \tag{4.3.10}$$

with $u_1 = \mathrm{Re}E$, $u_2 = \mathrm{Im}E$, $u_3 = du_1/dx$, $u_4 = du_2/dx$, $I = |E|^2 = u_1^2 + u_2^2$, $T = \theta - \eta \sin\phi$, and $P = 1 - \eta\cos\phi$. The fixed points u_{si} of Eq. 4.3.10 are the HSSs of the original LL Eq. 4.3.2. Asymptotic behavior of the CS tails at $x \to \pm\infty$ can be understood from the linear stability analysis of the HSS of Eq. 4.3.10 with spatial variable x viewed as time variable. To this end one can consider small deviations ϵ_i around u_{si}, i.e. $u_i(x) = u_{si} + \epsilon_i e^{\lambda x}$. Such an analysis for the case of LL equation with optical feedback leads to the following characteristic polynomial for the spatial eigenvalues

$$\lambda^4 - 2(T - 2I_S)\lambda^2 + 3I_S^2 + P^2 - 4I_S T + T^2 = 0. \tag{4.3.11}$$

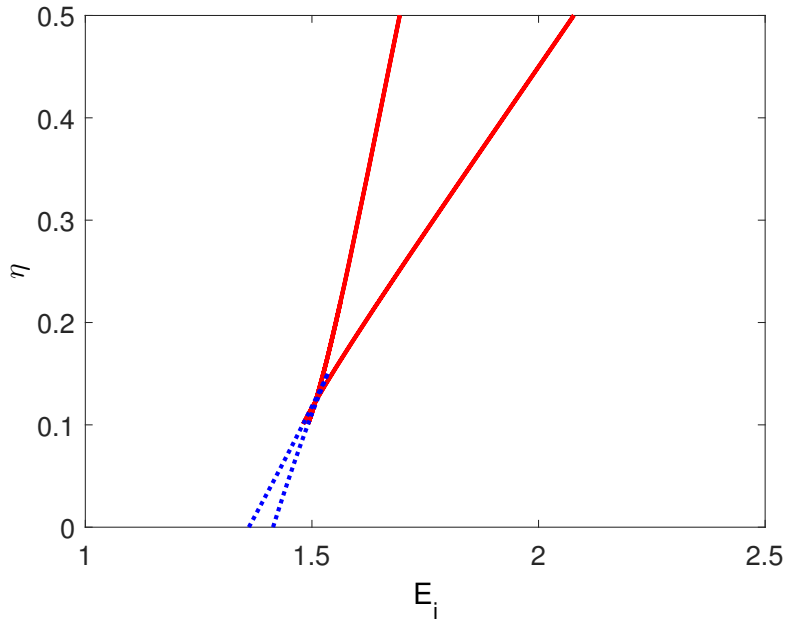

FIGURE 4.3.6. Map of the fold (dashed blue lines) and Andronov-Hopf (solid red lines) bifurcations in Lugiato-Lefever model in the plane of (E_i, η) for fixed feedback phase of $\phi = \pi$ and $\tau = 10$.

Spatial eigenvalues appear in pairs of opposite sign

$$\lambda = \pm\sqrt{\theta - \eta\sin\phi - 2I_S \pm \sqrt{I_S^2 - (1-\eta\cos\phi)^2}}, \tag{4.3.12}$$

i.e. a repelling eigenvalue is accompanied by an attracting one with the same rate. This is a consequence of the reflection symmetry $x \to -x$ of Eq. 4.3.2, i.e., the invariance of Eq. 4.3.10 with respect to the transformations $x \to -x$ and $(u_1, u_2, u_3, u_4) \to (u_1, u_2, -u_3, -u_4)$ [142, 143]. The qualitatively different eigenspectra have been classified in [142, 143] and are shown in Fig. 4.3.8 for the cases of: no feedback (a), and feedback with strength $\eta = 0.5$ and phases $\phi = 0$ (b) and $\phi = \pi$ (c). The case of feedback with strength $\eta = 0.5$ and phase $\phi = 0$ is shown on Fig. 4.3.9(a). The line RH denotes a reversible Hopf bifurcation, i.e. a Hopf bifurcation with a degenerate pair of pure imaginary eigenvalues in reversible system (4.3.10) and is defined by $I_S^{RH} = 1 - \eta\cos\phi$ which according to Eq. 4.3.12 gives $\lambda = \pm\sqrt{\theta - 2 + \eta(2\cos\phi - \sin\phi)}$, i.e. purely imaginary eigenvalues for $\theta < 2 + \eta(\sin\phi - 2\cos\phi)$. Quadruple zero (QZ) point with four-fold zero eigenvalue $\lambda = 0$ is then given by $\theta = 2 - \eta(\sin\phi - 2\cos\phi)$. On the right hand side of QZ point the RH curve becomes Belyakov-Devaney (BD) transition with two pairs of purely real eigenvalues so that no local bifurcation occurs at the BD line.

According to Eq. 4.3.12 for $I_S > 1 - \eta\cos\phi$ zero real part eigenvalues occur for $\theta = 2I_S + \eta\sin\phi \mp \sqrt{I_S^2 - (1-\eta\cos\phi)^2}$ which determines the lines SN_{h1}

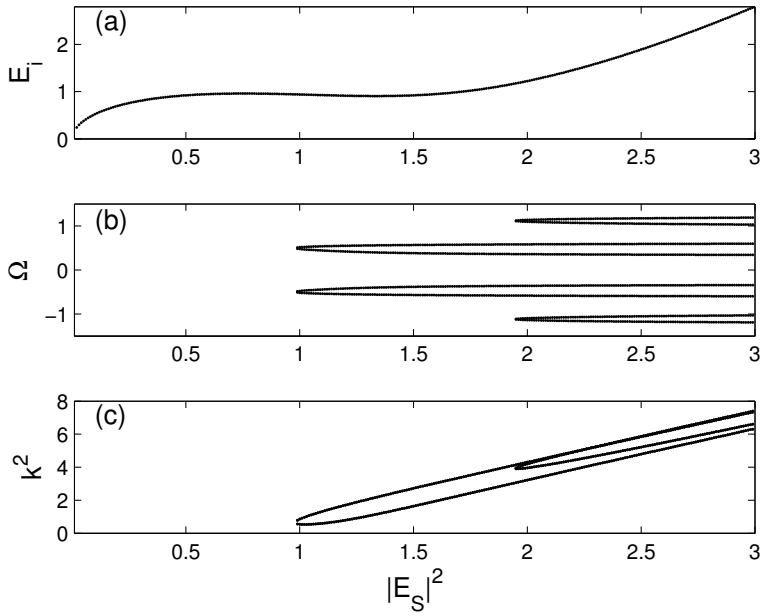

FIGURE 4.3.7. Time-delayed feedback-induced traveling-wave (TW) instability in Lugiato-Lefever model for $\eta = 0.5$ and $\phi = \pi/3$. (a) Steady-state homogeneous solution $E_i(I_S)$, $I_S = |E_S|^2$; (b) Imaginary parts of the eigenvalue Ω calculated from Eq. 4.3.7 for $k^2 > 0$. (c) Corresponding wave vector square, k^2.

and SN_{h2} of reversible Takens-Bogdanov or Takens-Bogdanov-Hopf bifurcations with two zero spatial eigenvalues and two purely real or imaginary eigenvalues of opposite sign. As can be seen by comparing Figs. 4.3.8(a)-(b) and 4.3.9(c), only a relative expansion or shrinkage of the different regions in the parameter space occurs when changing the feedback strength and phase, while the bifurcation picture remains the same. Fig. 4.3.9(b) presents the same bifurcation map as the one in Fig. 4.3.8(a) corresponding to $\eta = 0.5$ and $\phi = 0$, but in the plane $\theta - E_i$. In the spatial dynamics picture, CS is a homoclinic orbit to a fixed point (HSS) passing close to a periodic orbit (the pattern state). CS complexes form when CSs lock by their oscillating tails, i.e. when Eq. 4.3.12 possesses a complex quartet of eigenvalues.

Spatiotemporal dynamics

A homogeneous steady state may coexist with periodic structures such as hexagons and stripes [144, 136]. A CS consists of a region of one state surrounded by another state. When CSs are well separated from each other, they are independent and randomly distributed in space. However, when the distance between peaks decreases they start to interact via their oscillating, exponentially decaying tails. This interaction then leads to the formation of clusters [145] through the so-called snaking phenomenon [143]. Optical feedback does not change the clustering behavior, however, it changes the region in the parameter space where clustering

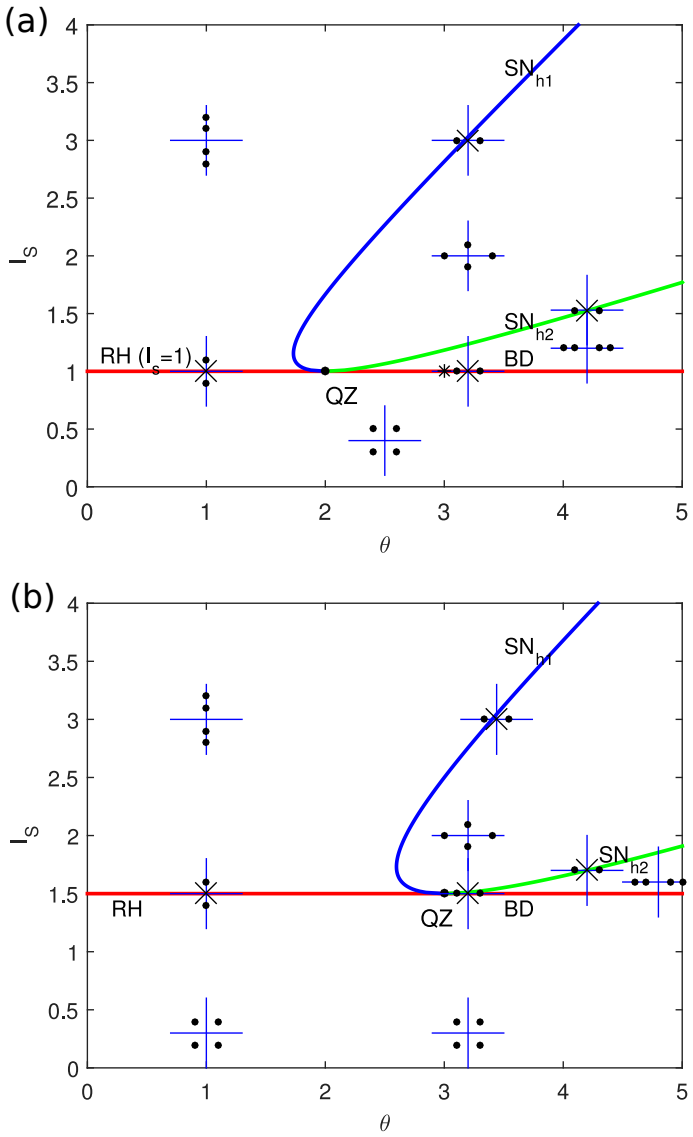

FIGURE 4.3.8. Regions of different spatial eigenvalue spectra on (θ, I_s) plane, denoted by pictograms: dots denote single and crosses - double (degenerate) eigenvalues with x (y) axis - real (imaginary) value. Transition (bifurcation) lines between different regions are denoted by $SN_{h1,2}$ for saddle-node bifurcation, RH for reversible Hopf bifurcation and BD for Belyakov-Devaney transition.. QZ denotes quadruple-zero eigenvalue. Feedback strength and phase are: (a) $\eta = 0$, (b) $\eta = 0.5$, $\phi = 0$ and (b) $\eta = 0.5$, $\phi = \pi$.

appears. Moreover, the behavior can now occur as a function of the delayed feedback parameters. An example is shown in Fig. 4.3.10 where the three cavity soliton branches of single CS, double and triple CS clusters as a function of the

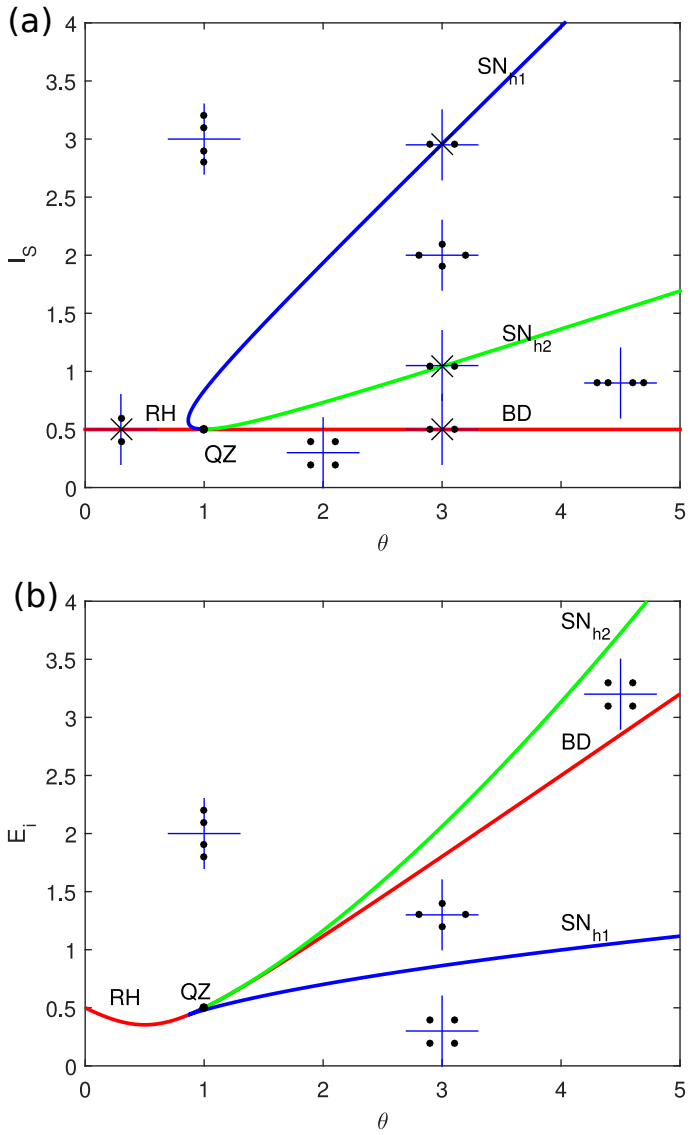

FIGURE 4.3.9. (a) Regions of different spatial eigenvalue spectra on (θ, I_s) plane, denoted by pictograms: dots denote single and crosses - double (degenerate) eigenvalues with x (y) axis - real (imaginary) value. Transition (bifurcation) lines between different regions are denoted by $SN_{h1,2}$ for saddle-node bifurcation, RH for reversible Hopf bifurcation and BD for Belyakov-Devaney transition. QZ denotes quadruple-zero eigenvalue. Feedback strength and phase are $\eta = 0.5$, $\phi = 0$. (b) Same map is presented in the plane (θ, E_i).

strength η of the time-delayed feedback are demonstrated. Here the black (grey) solid line is the stable (unstable) HSS.

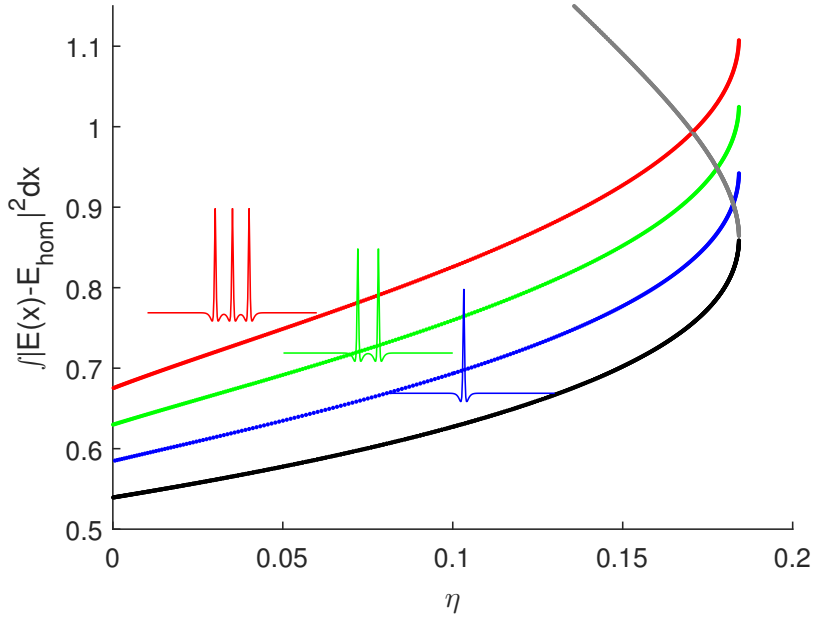

FIGURE 4.3.10. Three cavity soliton branches of single CS (blue), double (green) and triple (red) CS clusters as a function of the strength η of the time-delayed feedback for $E_i = 1.3$, $\tau = 10$ and $\phi = \pi/3$. Black (grey) solid line is the homogeneous stable (unstable) steady state.

The delayed optical feedback may also induce in the LL model a drift bifurcation of the CS, similar to the case of the laser with saturable absorber in the previous Section. It was previously reported in the case of Swift-Hohenberg equation [96] and the VCSEL model [140, 124] as well. Such a feedback induced CS drift is illustrated in Fig. 4.3.11 for the case of $\theta = 2$, $E_i = 1.3$, and delayed feedback with a fixed phase $\phi = \pi$ and different strengths $\eta = 0.11$, 0.12, and 0.15. The CS is launched at $t = 0$ and starts moving after a certain delay, which decreases as the feedback strength is increased, see also [140]. Furthermore, the CS moves faster as η is increased.

In order to estimate the threshold of the CS drift bifurcation we proceed in a similar way as in previous Sections, see also [96, 124]. Slightly above this threshold one can consider a CS moving uniformly with a small velocity $v = |\mathbf{v}|$ and expand the electric field amplitude in power series of v: $E = E_0(\boldsymbol{\xi}) + v\,[E_1(\boldsymbol{\xi}) + vE_2(\boldsymbol{\xi}) + v^2E_3(\boldsymbol{\xi}) + ...]$. Here $E = E_0(\mathbf{r})$ is the stationary soliton profile, $\boldsymbol{\xi} = \mathbf{r} - v\,\mathbf{e}\,t$, $\mathbf{r} = (x, y)$, and $\mathbf{e}$ is the unit vector in the direction of the soliton motion. Substituting this expansion into Eq. (4.3.2) and collecting the first order terms in small parameter v one obtains

$$L \begin{pmatrix} \mathrm{Re}E_1 \\ \mathrm{Im}E_1 \end{pmatrix} = \begin{pmatrix} \mathrm{Re}[w_{01}(1+\eta\tau e^{i\varphi})] \\ \mathrm{Im}[w_{01}(1+\eta\tau e^{i\phi})] \end{pmatrix} \tag{4.3.13}$$

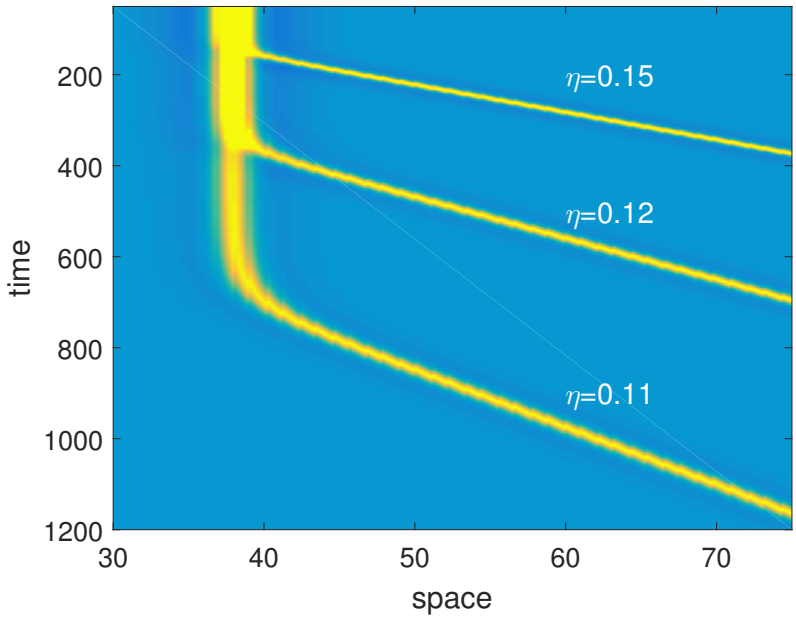

FIGURE 4.3.11. CS drift for $\theta = 2, E_i = 1.3$ and feedback with different strengths η and fixed delay time of $\tau = 10$ and phase of $\phi = \pi$. The CS is launched at $t = 0$ and start moving after a certain delay, which decreases as the feedback strength is increased [140]. Notice also the CS moves faster as η is increased.

with $w_{01} = \mathbf{e} \cdot \nabla E_0$. The linear operator L is given by

$$L = \begin{pmatrix} 1 + 2A_0B_0 & \nabla^2_{eff} + 2B_0^2 \\ -\nabla^2_{eff} - 2A_0^2 & 1 - 2A_0B_0 \end{pmatrix},$$

where $A_0 = \mathrm{Re}E_0$, $B_0 = \mathrm{Im}E_0$ and $\nabla^2_{eff} = \nabla^2 - \theta + |E_0|^2$. By applying the solvability condition to the right hand side of Eq. (4.3.13), one obtains the drift instability threshold which is similar to the case of the laser with saturable absorber:

$$\eta\tau = -\frac{X_1 + Y_2}{\cos\phi(X_1 + Y_2) + \sin\phi(Y_1 - X_2)}, \tag{4.3.14}$$

where $X_{1,2} = \langle \psi^\dagger_{1,2}, \nabla \mathrm{Re}E_0 \rangle$ and $Y_{1,2} = \langle \psi^\dagger_{1,2}, \nabla \mathrm{Im}E_0 \rangle$. Here, the eigenfunction $\psi^\dagger = \left(\psi^\dagger_1, \psi^\dagger_2\right)^T$ is the solution of the homogeneous adjoint problem $L^\dagger\psi^\dagger = 0$ and the scalar product $\langle , \rangle$ is defined as $\langle U, V \rangle = \int_{-\infty}^{+\infty} UV\, d\mathbf{r}$. For a feedback phase of $\phi = \pi$, one can recover from (4.3.14) the threshold condition obtained earlier for the drift instability of cavity solitons in the Swift-Hohenberg equation with delayed feedback, $\eta_0\tau = 1$ [96]. In Fig. (4.3.12) the threshold values of the product of the feedback strength and delay time $\eta_0\tau$ at onset of CS drift instability as a function of feedback phase ϕ are plotted. As in the previous model, previously

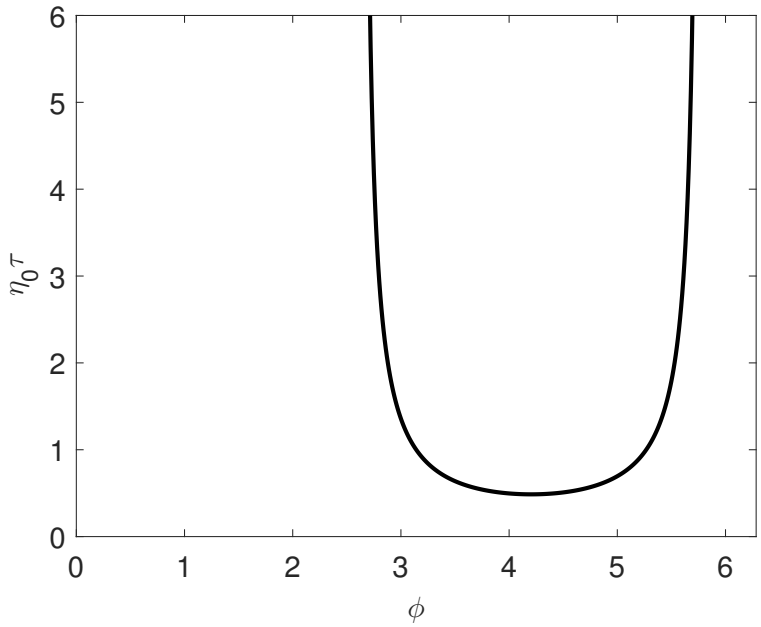

FIGURE 4.3.12. Threshold values of the product of the feedback strength and delay time $\eta_0\tau$ at the onset of CS drift instability as a function of feedback phase ϕ. LL parameters are $\theta = 2$ and $E_i = 1.3$.

observed for the VCSEL model in [124] the drift instability is only possible in certain windows of the feedback phase.

One can now proceed with increasing the feedback strength beyond the drift instability threshold. Fig. 4.3.13 shows the CS time-evolution as the feedback strength η is increased from 0 to 0.5 by a step of 0.02 each 200 time units. The feedback phase is fixed at $\phi = \pi$. Fig. 4.3.14 presents the space-time dynamics for fixed feedback parameters in the four representative regions denoted in Fig. 4.3.13 by A, B, C and D. As can be seen from Fig. 4.3.13, a stable stationary CS shown in Fig. 4.3.14 persists until the feedback strength reaches the value $\eta = 0.16$ at time $t = 1600$. At this feedback strength a drift bifurcation takes place and the CS starts moving, see Fig. 4.3.14B. When the feedback strength reaches a value of $\eta = 0.34$ at time $t = 3600$, the CS drifting with a constant velocity undergoes an Andronov-Hopf bifurcation, leading to undamped oscillations of the soliton, see Fig. 4.3.14C. Finally, at the feedback strength of $\eta = 0.42$ (at time $t = 4200$) the system enters a well developed spatio-temporal chaotic regime, see Fig. 4.3.14D. Note, that recently it was demonstrated that optical feedback can induce spatial-temporal chaotic dynamics in the Lugiato-Lefever model, which may lead to the appearance of rogue waves [146].

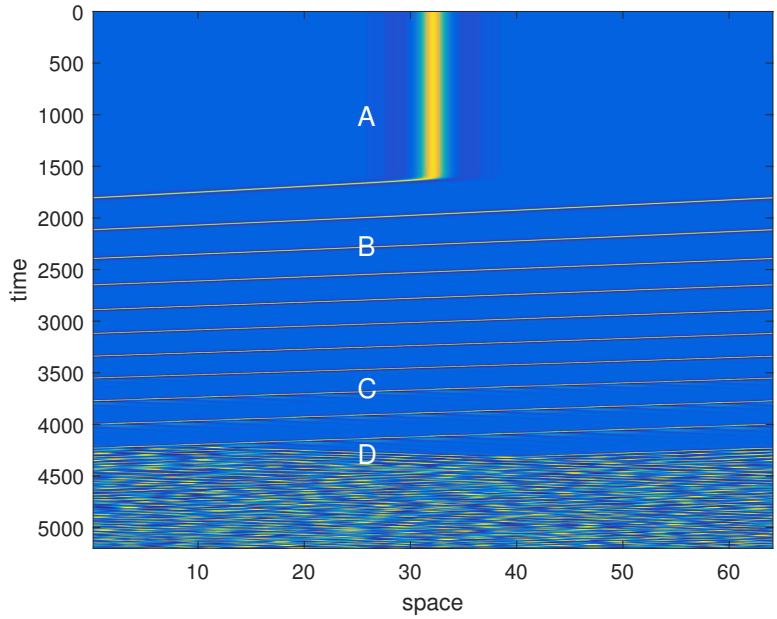

FIGURE 4.3.13. (color online) CS evolution from a stable CS through moving and moving-oscillating CS till developed spatio-temporal chaos. $\theta = 2$, $E_i = 1.3$, and the feedback strength η increases each 200 time units from 0 to 0.5 with step of 0.02. Feedback delay is $\tau = 10$ and phase is $\phi = \pi$.

4.4. Discussion

In this Chapter of the Thesis the dynamics of localized structures in several spatially extended dynamical systems under the influence of delayed optical feedback was investigated. First, we have considered a model of wide-aperture laser with a saturable absorber and delayed optical feedback [147], and demonstrated the appearance of multiple coexistent laser cavity solitons. In a limit of large delay, these localized solutions form a tube in parameter coordinates similar to the case of plane waves in CGLE. In addition, we report a novel destabilization mechanism of localized solutions in spatially extended systems, which is induced by delayed feedback. It is shown that at large delays apart from the drift and phase instabilities the soliton can exhibit a delay-induced modulational instability associated with the translational neutral mode. The combination of drift and modulational instabilities produces zigzagging motion of the solitons, which are either periodic, with the period close to the delay time, or chaotic, with low-frequency fluctuations in the direction of the soliton motion.

The impact of delayed optical feedback on the spatial and spatio-temporal dynamics of Lugiato-Lefever model was analysed as well [148]. It was shown the shape of the bistable curve of the homogeneous solution can be significantly modified due to the presence of the delayed feedback. The linear stability analysis of this solution reveals the impact of the delayed feedback strength and phase

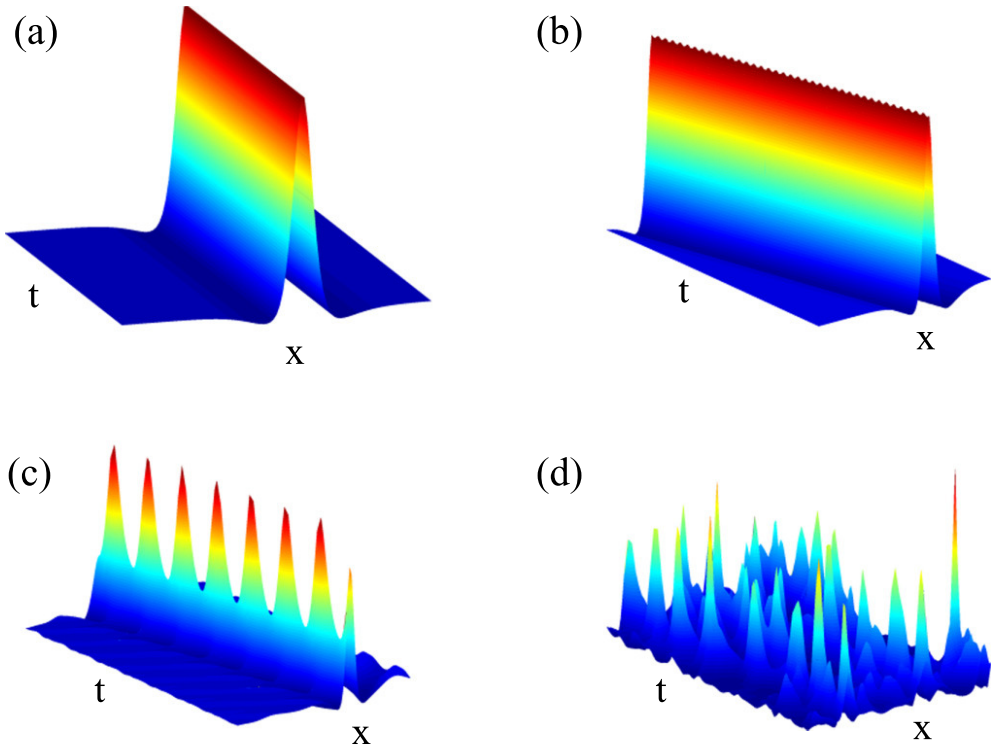

FIGURE 4.3.14. Space-time dynamics in the LL model for fixed optical feedback parameters in the four representative regions denoted in Fig. 4.3.13 by A, B, C and D. The feedback strength is: a) $\eta = 0.08$, b) $\eta = 0.2$, c) $\eta = 0.34$, d) $\eta = 0.4$.

on the Turing, Andronov-Hopf, and traveling wave instability regions. It was demonstrated that the delayed feedback influences the spatial dynamics by only shifting the regions with different spatial eigenvalue spectra. Considering the spatio-temporal dynamics, the influence of the delayed feedback strength on the clustering behavior at a fixed feedback phase was investigated. Depending on the feedback parameters, delayed feedback may also induce a drift bifurcation from a stationary cavity soliton to a moving one, as well as an Andronov-Hopf bifurcation of the moving soliton, which would become a sequence of Andronov-Hopf with the increase of delay time and eventually form the aforementioned modulational instability in the limit of large delay. It was shown, that above a certain value of the delayed feedback strength the Lugiato-Lefever system enters a region of spatial-temporal chaos.

Finally, the same phenomena of appearance of delay induced modulational instability was demonstrated for the localized structures in cubic-quintic Ginzburg-Landau equation. Since the CGLE plays a role of the normal form for a large class of complex spatially-extended systems of different physical origin [66], the results are also relevant beyond the scope of the nonlinear optics. Based on our results one can expect that the observed phenomena of delay induced multistability of CSs as well as delay-induced modulational instability and zigzagging of

CSs appear in other spatially extended systems subject to delayed feedback. It would be necessary to remark, that the delay-induced modulational instability was already defined in [76] for the linearized system. However, until now there was no known example as well as a detailed study of the development of such kind of instability either in fully nonlinear models or real physical phenomena.

CHAPTER 5

Dynamics in coupled systems with time-delay

5.1. Introduction

In this Chapter, the dynamics in the array of mode-locked lasers described by the coupled systems of delay equations is investigated. In general, the analysis and results of this Chapter are applicable to a large class of arrays of coupled spatially extended dynamical systems which admit localized pulse solutions. In what follows, the analysis is performed for the particular system with ring geometry with symmetrical bi-directional coupling, where each node on a ring is a mode-locked laser emitting a train of short pulses.

Mode-locked semiconductor lasers are widely used for generation of short optical pulses with high repetition rates and optical frequency combs suitable for numerous practical applications. Combining many lasers into an array one can achieve much larger output power and substantially improve the characteristics of the output beam by synchronizing the frequencies of the individual lasers [149, 150, 151, 152, 153, 154, 155, 156]. Furthermore, it was recently demonstrated experimentally and verified theoretically that, in contrast to broad area lasers suffering from transverse instabilities leading to poor output beam quality, beam anti-phase synchronization in multistripe laser arrays can be used to generate high power beams with low far-field divergence [157, 63]. Unlike most previous studies focused on the dynamics of coupled CW lasers, here we investigate the dynamical regimes of operation in an array of pulsing mode-locked lasers locally coupled via overlapping evanescent fields in a ring geometry. Note that investigations of the dynamical regimes in a similar system of two coupled mode-locked lasers were recently reported in [158].

First, in Section 2 of this Chapter the model equations for the array of mode-locked lasers will be introduced. In the next Section, the amplitude synchronized solutions and their stability are described. In Section 4, it will be demonstrated that the system has a novel stable dynamical regime where a periodic sequences of clusters of fundamental mode-locked pulses are radiated. One can show that the described novel pulse train states coexist with the regimes which are amplitude synchronized and possess fixed phase shifts between lasers. In Section 5, the discussion on the results of this Chapter is given.

5.2. Model equations

Schematic representation of the ring array of mode-locked lasers coupled via overlapping electric fields is shown in Fig. 5.2.1. The dynamics of such system can

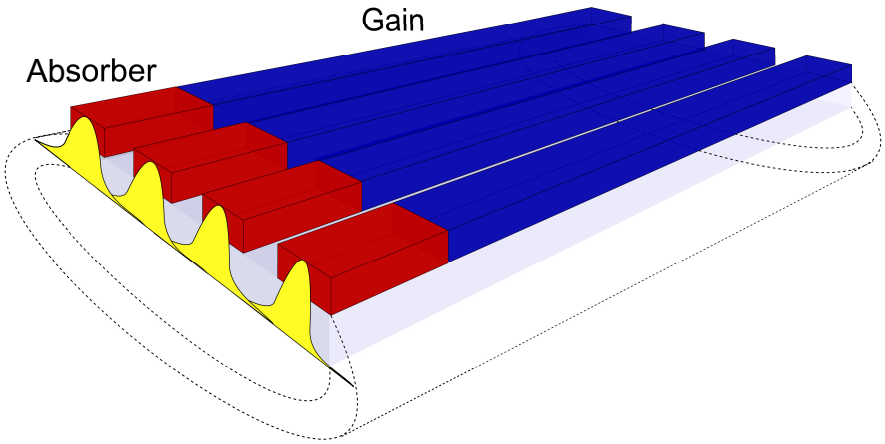

FIGURE 5.2.1. Schematic representation of a ring array of passively mode-locked lasers coupled via overlapping evanescent fields (yellow). Gain and absorber sections are indicated by blue and red color, respectively.

be described by the set of symmetrically coupled systems of delay differential equations for a single mode-locked laser [159]:

$$\begin{aligned} \dot{A}_j + \gamma A_j &= \gamma\sqrt{\kappa} R_j A_j(t-\tau) + \eta e^{i\varphi}(A_{j-1} + A_{j+1}), \\ \dot{G}_j &= G_0 - \gamma_g G_j - e^{-Q_j}(e^{G_j} - 1)|A_j(t-\tau)|^2, \\ \dot{Q}_j &= Q_0 - \gamma_q Q_j - s(1 - e^{-Q_j})|A_j(t-\tau)|^2, \end{aligned} \tag{5.2.1}$$

where $j = 1, ..., N$. Here, A_j denotes the complex field amplitude of j-th laser, whereas G_j and Q_j are saturable gain and loss, respectively, and

$$R_j := \exp\left[(1 - i\alpha_g)\, G_j - (1 - i\alpha_q)\, Q_j\right]/2 - i\vartheta.$$

All laser indexes j are taken modulo N. The parameter γ represents the spectral filtering bandwidth, κ is the attenuation factor describing linear non-resonant intensity losses per cavity round trip, G_0 is the pump parameter, which is proportional to the injection current in the gain region, Q_0 is the unsaturated absorption parameter, γ_g and γ_q are the carrier relaxation rates in the amplifying and absorbing sections, respectively, and s is the ratio of the saturation intensities in these two sections. Though all the parameter values can vary among different lasers, one can assume that this variation is sufficiently small and consider equal parameters. In the absence of coupling, i.e. for $\eta = 0$, for the chosen parameter values (see Table 1.) each laser operates in a stable fundamental passive mode-locking regime with a single sharp pulse per cavity round trip time [159]. This regime corresponds to modulated waves (relative periodic orbits) with $A_j(t) = U(t - \theta_j)e^{i\omega t + i\upsilon_j}$, $G_j = G(t - \theta_j)$, and $Q_j = Q(t - \theta_j)$, where $U(t)$, $G(t)$, and $Q(t)$ are periodic in time with the period T close to the delay τ, and arbitrary phase shifts θ_j and υ_j.

$\gamma = 33.3$	$G_0 = 2.0$
$\kappa = 0.1$	$Q_0 = 4.0$
$\alpha_g = 2.0$	$\gamma_g = 0.0133$
$\alpha_q = 3.0$	$\gamma_q = 1$
$\vartheta = 0$	$s = 25$
	$\tau = 1.875$

TABLE 1. Parameters for a single mode-locked laser

5.3. Amplitude synchronized solutions

5.3.1. Existence and stability of synchronized solutions

For small coupling η, the phase shifts θ_j and υ_j start evolving slowly in time due to the interaction between the lasers and, as a result, a synchronized state can be achieved. In particular, due to the index shift symmetry of the system, the solutions are observed [160, 155, 156, 161, 162], which are synchronized in amplitude $|A|_{j+1} = |A|_j$ with some constant phase shift between the adjacent lasers $\upsilon = \upsilon_{j+1} - \upsilon_j = 2\pi l/N$, i.e. $A_{j+1} = e^{i\upsilon}A_j$, where $N\upsilon \mod 2\pi = 0$. Then the coupling term C in Eq. (5.2.1) reads:

$$C = \eta e^{i\varphi}(A_{j-1} + A_{j+1}) = \eta e^{i\varphi}A(e^{-i\upsilon} + e^{i\upsilon}) = (2\eta\cos\upsilon)e^{i\varphi}A. \tag{5.3.1}$$

Due to the symmetrical coupling and the fact that lasers are identical, l can change from 0 to $N/2$ if N is even or $(N-1)/2$ if N is odd. Here, $l = 0$ corresponds to complete synchronization. Figure 5.3.1 shows the amplitude and phase profiles of anti-phase ($l = N/2$) synchronized solution. There is also a potentially interesting "non-invasive" case $l = N/4$, for which the coupling vanishes $A_{j-1} + A_{j+1} = 0$. For odd values of N, however, the anti-phase and non-invasive synchronized regimes do not exist.

Further we consider the minimal cases of $N = 2$ and $N = 4$ lasers, where $N = 4$ is the smallest number that allows in-phase, anti-phase, and non-invasive synchronized solutions. Following the approach of *master stability function* [163, 164], one can calculate the stability for any amplitude synchronized solution.

First, one can introduce new vectors of dynamical variables $\mathbf{x}^j = \left(x_1^j, x_2^j, x_3^j\right)^T$: $A_j = e^{ij\upsilon}x_1^j, G_j = x_2^j, Q_j = x_3^j$, so that all lasers are completely synchronized in $\mathbf{x}^j(t) = \mathbf{s}(t)$. The coupled equations (5.2.1) then become

$$\dot{\mathbf{x}^j} = \mathbf{F}\left(\mathbf{x}^j\right) + \mathbf{P}\left(\mathbf{x}^j\left(t-\tau\right)\right) + \eta e^{i\varphi}\sum_{p=1}^{N} B_{jp}\mathbf{H}\left(\mathbf{x}^j\right), \tag{5.3.2}$$

where $\mathbf{F}$ and $\mathbf{P}$ are the uncoupled instantaneous and delayed parts of the dynamics, $\mathbf{H}\left(\mathbf{x}^j\right) = (x_1^j, 0, 0)^T$ is the output function of the dynamical variables of each laser, and B_{jp} is the corresponding element of coupling matrix $\mathbf{B}$. Note that in

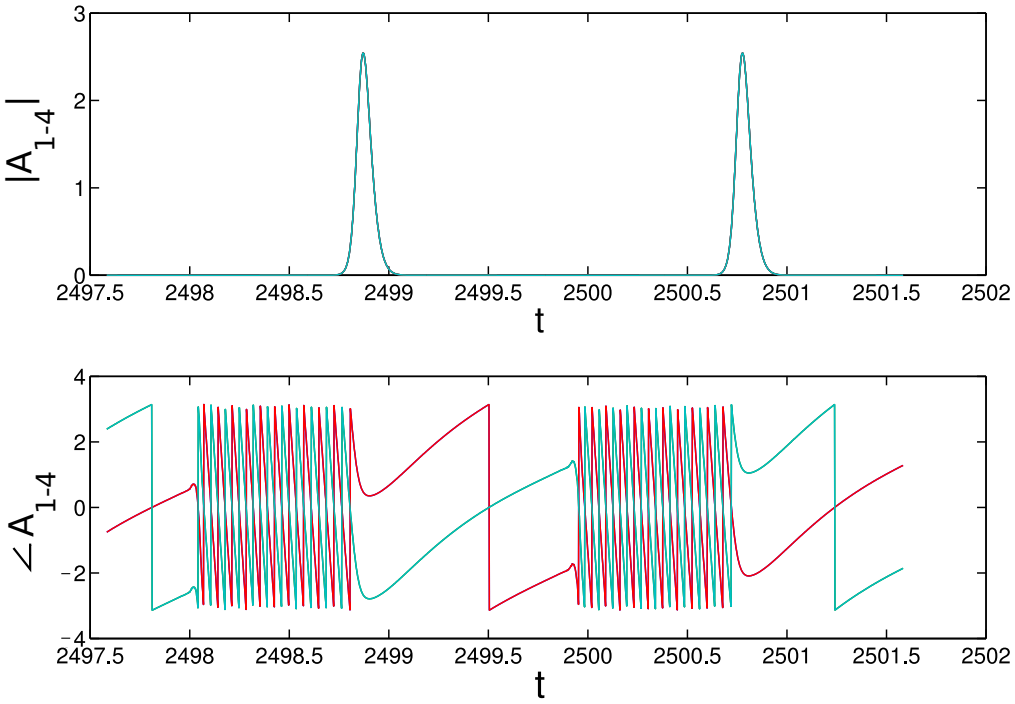

FIGURE 5.3.1. Intensity (top) $|A_{1-4}|^2$ and instantaneous phase (bottom) $\angle A_{1-4}$ of the numerically simulated stable anti-phase synchronized solution in a system of four coupled lasers for $\eta = 2.5, \varphi = \pi/2$. Colors overlap, demonstrating complete amplitude synchronization and two pairs of phase synchronized lasers with phase difference $\upsilon_{j+1} - \upsilon_j = \pi$. Other parameters: $\gamma = 33.3$, $\kappa = 0.1$, $\alpha_g = 2.0$, $\alpha_q = 3.0$, $\vartheta = 0$, $G_0 = 2.0$, $Q_0 = 4.0$, $\gamma_g = 0.0133$, $\gamma_q = 1$, $s = 25$, and $\tau = 1.875$.

this case the coupling matrix is

$$\mathbf{B} = \begin{pmatrix} 0 & e^{iv} & \cdots & 0 & e^{-iv} \\ e^{-iv} & 0 & e^{iv} & \cdots & 0 \\ . & . & \ddots & . & . \\ 0 & \cdots & e^{-iv} & 0 & e^{iv} \\ e^{iv} & 0 & \cdots & e^{-iv} & 0 \end{pmatrix}.$$

Now we insert the perturbed values of $\mathbf{x}^j(t) = \mathbf{s}(t) + \xi^j(t)$ in (5.3.2) and expand all functions in Taylor series to 1st order. This gives

(5.3.3)

$$\dot{\xi}^j = \left[D\mathbf{F}(\mathbf{s})\,\delta_{ij} + \eta e^{i\varphi} \sum_{p=1}^{N} B_{jp} D\mathbf{H}(\mathbf{s}) \right] \cdot \xi^j(t) + \left[D\mathbf{P}(\mathbf{s}(t-\tau))\,\delta_{ij} \right] \cdot \xi^j(t-\tau),$$

where $D\mathbf{F}(\mathbf{s})$, $D\mathbf{P}(\mathbf{s}(\mathbf{t}-\tau))$ and $D\mathbf{H}(\mathbf{s})$ are the Jacobians of the uncoupled system and output function, and δ_{ij} is a Kroneker delta. Now we use the fact that

the equations (5.3.3) are organized in block form, where the blocks correspond to the (jp) indices of $\mathbf{B}$. The system (5.3.3) then can be diagonalized (the first term remains the same) and rewritten in eigenmode form:

$$\dot{\zeta}^k = \left[D\mathbf{F}\left(\mathbf{s}\right) + \eta e^{i\varphi}\sigma_k D\mathbf{H}\left(\mathbf{s}\right)\right]\cdot\zeta^k\left(t\right) + \left[D\mathbf{F}_\tau\left(\mathbf{s}\left(t-\tau\right)\right)\right]\cdot\zeta^k\left(t-\tau\right), \tag{5.3.4}$$

where σ_k is kth eigenvalue of $\mathbf{B}$. Using the properties of $\mathbf{B}$, one can find its eigenvalues as $\sigma_k = e^{-iv}\sigma_{-1,k} + e^{iv}\sigma_{+1,k}$, where $\sigma_{\pm1,k} = e^{\pm 2\pi ik/N}$ are the eigenvalues of $N\times N$ matrices $\mathbf{B}_{+1}$ and $\mathbf{B}_{-1}$ [spatial plane wave modes with wavenumber k]:

$$\mathbf{B}_{+1} = \begin{pmatrix} 0 & 1 & \cdots & 0 & 0 \\ 0 & 0 & 1 & \cdots & 0 \\ . & . & \ddots & . & . \\ 0 & \cdots & 0 & 0 & 1 \\ 1 & 0 & \cdots & 0 & 0 \end{pmatrix}, \quad \mathbf{B}_{-1} = \begin{pmatrix} 0 & 0 & \cdots & 0 & 1 \\ 1 & 0 & 0 & \cdots & 0 \\ . & . & \ddots & . & . \\ 0 & \cdots & 1 & 0 & 0 \\ 0 & 0 & \cdots & 1 & 0 \end{pmatrix}.$$

To find all the Floquet exponents μ for linearized problem (5.3.4), one should first calculate the branch of original solutions of equation (5.2.1) with coupling term $C_0 = \chi_0 A = 2\eta\cos\left(2\pi l/N\right)e^{i\varphi}A$ (5.3.1). Then, for stability calculation on the chosen branch instead of C_0 one should use N equations with the corrected coupling term

$$\begin{aligned} C_k &= \eta e^{i\varphi}\left(e^{-2\pi il/N}e^{-2\pi ik/N} + e^{2\pi il/N}e^{2\pi ik/N}\right)A = \\ &= 2\cos\left(2\pi\left(k+l\right)/N\right)\eta e^{i\varphi}A = \chi_k A. \end{aligned} \tag{5.3.5}$$

The linearization of each of these equations is exactly Eq. (5.3.4) and provides the stability of the synchronized systems of N lasers against the plane wave with wavenumber $k = 1..N$.

Figure 5.3.2, (a) demonstrates the stability regions for the in-phase and anti-phase synchronized mode-locked solutions of the system of four lasers using the master stability function approach [163] in the (φ,η) - plane of coupling parameters. The form of coupling implies that the stability region of the anti-phase synchronized solution coincides with that of the in-phase synchronized solution shifted by π with respect to the coupling phase angle φ. Interestingly, the none-invasive solution is unstable for all values of coupling parameters (φ,η). The results were obtained with path continuation package DDE-BIFTOOL. Furthermore, the P and T lines in Fig. 5.3.2, (a) show bifurcation thresholds of the in-phase synchronized regime ($l = 0$). In particular, the green line (T) indicates a torus bifurcation threshold whereas the two red lines correspond to pitchfork bifurcations.

5.3.2. Numerical simulation of bifurcations of phase synchronized solution

Let us perform direct numerical simulation of system (5.2.1) for $N = 4$ and plot first and second laser amplitude maximums $\max|A_{1,2}|$ while changing slowly the coupling phase angle φ for fixed η=0.5. Figure 5.3.3, (a) shows one-dimensional bifurcation diagram when φ increases from $\varphi = 0$ to $\varphi = 2\pi$. Figure 5.3.3, (c), shows the instantaneous phase difference between two adjacent lasers $\angle A_1 - \angle A_2$.

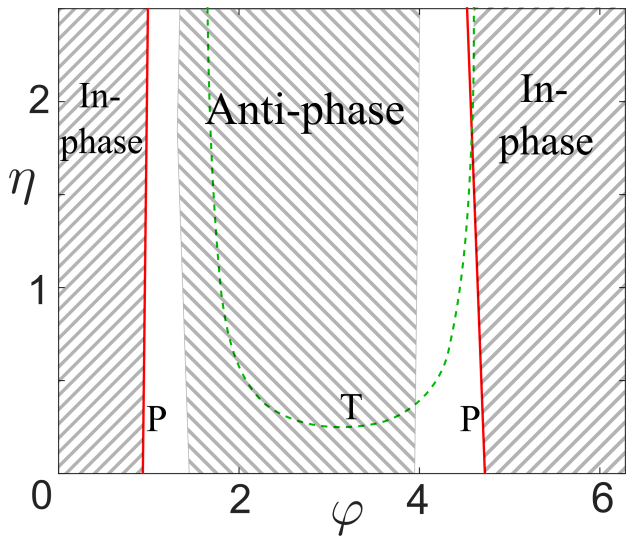

FIGURE 5.3.2. (a) Bifurcation diagram in coordinates (φ, η) for the synchronized solutions in the ring array of four lasers. Left- and right-inclined hatching indicates the stability regions for the in-phase ($l = 0$) and anti-phase ($l = 2$) synchronized solutions. Green line corresponds to a torus bifurcation (T) and red lines to pitchfork bifurcations (P) of the in-phase synchronized solution.

We start with fully synchronized solution, which then undergoes pitchfork bifurcation and after some transient period where becomes anti-phase synchronized solution. Since from the model equations (5.2.1) it follows that the dynamics of anti-phase solution is the same as in-phase after the transformation $\varphi \to \varphi + \pi$, from this point the picture repeats itself as one increases phase angle φ and switches between phase and anti-phase synchronized solutions.

As the parameter is swept in other direction, decreasing φ from 2π to 0, see Fig. 5.3.3, (b) and (d), one obtains a different picture. We start again from complete synchronized regime, but instead of switching between phase and anti-phase synchronized solutions, after the transition around $\varphi = 5$, a new *bound pulse train* regime appears, which is a subject of the next section.

5.4. Bound pulse trains

5.4.1. Space-time representation of bound pulse train regimes

The torus bifurcation T in Fig. 5.3.2 leads to a slight change of the pulse shape from one pulse period to another, while synchronization and period of pulsing remain the same. Instead, the pitchfork bifurcations P of the synchronized solution lead to the appearance of a new *pulse train bound-state regime*. In this regime, lasers pulse sequentially on the ring one after another, as shown in Fig. 5.4.2. Here, each laser stays close to its fundamental mode-locked regime with period τ_0 close to the delay time τ. The pulse train bound-state regime can be better

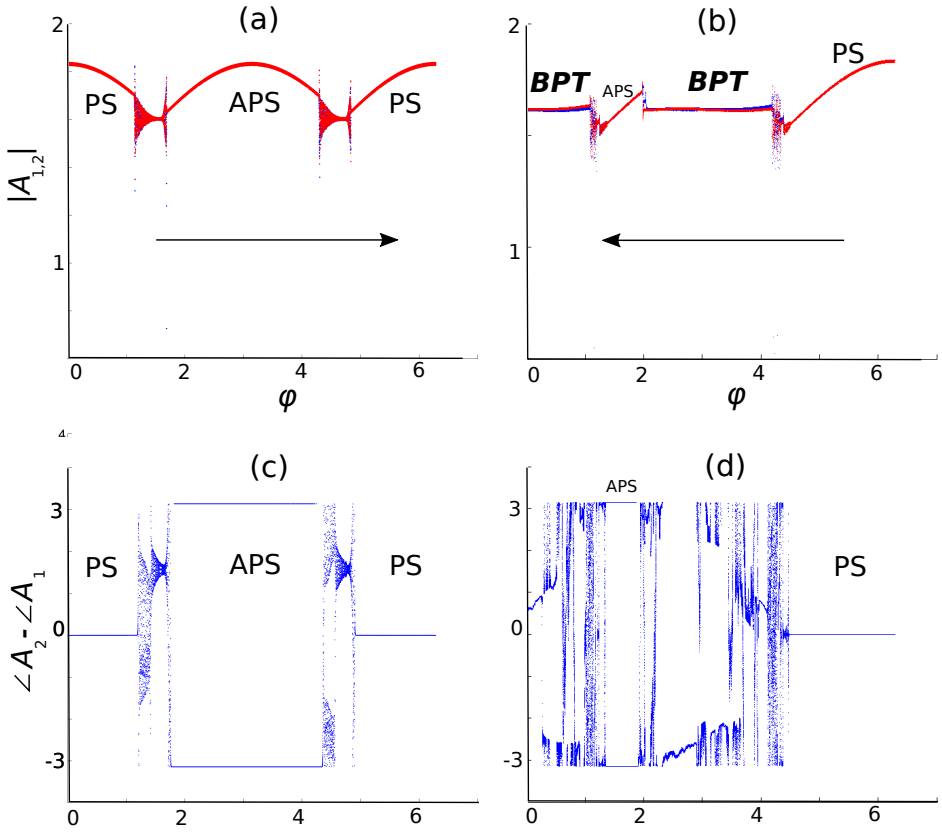

FIGURE 5.3.3. Bifurcation diagram for a system of two mode-locked lasers obtained numerically by sweeping coupling phase parameter φ. Left column: increasing coupling phase φ, (a) shows amplitudes $\max|A_{1,2}|$ with red and blue dots correspondingly, (c) shows instantaneous phase difference $\angle A_2 - \angle A_1$. Right column: decreasing coupling phase φ, (b) shows $\max|A_{1,2}|$, (d) shows $\angle A_2 - \angle A_1$. Coupling strength is fixed to $\eta = 0.5$. Other parameters from Table (1).

visualized using the so-called pseudo-spatial coordinates plane (T, σ) [33], where $\sigma = t \bmod \tau_0$ is the original fast time and $T = t/\tau_0$ is the slow time (number or round trips, $\tau_0 = \tau + 0.03$), see Fig. 5.4.1(a). One can observe that pulses which were initially distributed on the interval $\sigma \in [0, \tau_0]$ start to interact and finally form a bound cluster. The distance between the pulses in this cluster can be controlled by changing the coupling phase φ, as demonstrated on Fig. 5.4.2, (a) and (b). Similar bound pulse train for the case of two coupled lasers is shown in Fig. 5.4.1(b).

5.4.2. Analytical derivation of bound pulse trains

In what follows, we investigate the origin of this bound state solution by applying the multiscale method [165, 83] to the two-laser system in order to find the reduced

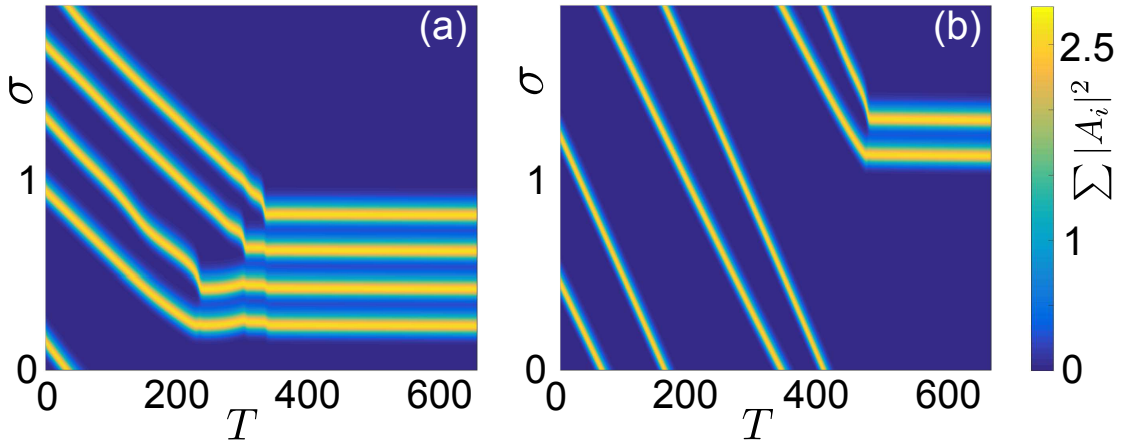

FIGURE 5.4.1. (a) Space-time diagram of the pulse train bound state regime for four lasers in coordinates (T, σ), where $\sigma = t \bmod \tau_0$ is the original fast time and $T = t/\tau_0$ the slow time ($\tau_0 = 1.9054$). Brighter colors indicate higher values of the sum of the laser intensities $\sum_{i=1}^{4} |A_i|^2$. (b) Space-time diagram for pulse train bound state regime for two lasers ($\tau_0 = 1.9043$). Coupling parameters are: η=0.5, $\varphi = 3.0$. Other parameters are the same as in previous figures.

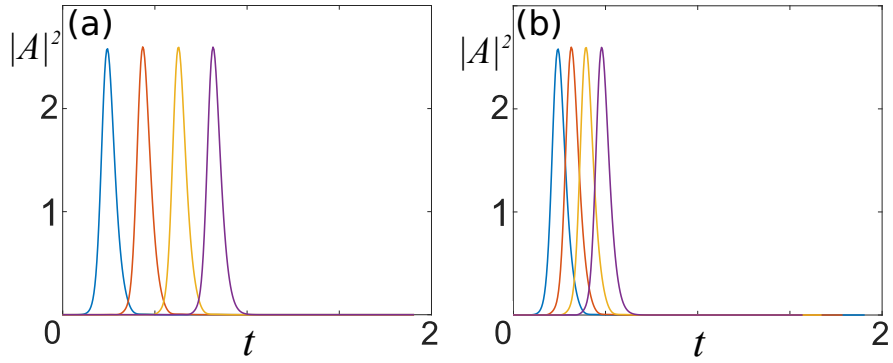

FIGURE 5.4.2. Laser intensities for the stable bound pulse train regime in a ring of four lasers calculated for η=0.5 and (a): phase $\varphi = 3.0$, (b): $\varphi = 4.5$. Different colors correspond to different lasers. Other parameters are the same as in previous figures.

system of equations governing the slow dynamics of the time separation between the pulses and their phase differences.

In order to use the multiscale method, we consider the limit of small coupling, $\eta = \varepsilon\mu$ with a small parameter ε, and search for the solution of system (5.2.1) in the form $A_j(t_0, t_1) = e^{i\phi_j(t_1)}\mathcal{A}\left[t_0 + \theta_j(t_1)\right] + \varepsilon A_j^1(t_0, t_1)$, $G_j = \mathcal{G}\left[t_0 + \theta_j(t_1)\right] + \varepsilon G_j^1(t_0, t_1)$, and $Q_j = \mathcal{Q}\left[t_0 + \theta_j(t_1)\right] + \varepsilon Q_j^1(t_0, t_1)$. Here $\mathcal{A}$, $\mathcal{G}$, and $\mathcal{Q}$ is a τ_0-periodic

solution of the unperturbed system (mode-locked regime in an uncoupled laser), A_j^1, G_j^1, and Q_j^1 describe first order corrections due to the coupling between the lasers, $t_0 = t$ and $t_1 = \varepsilon t$ are fast and slow times, respectively.

Let us write down the equations for two coupled lasers. We have moved all the delayed terms A_τ, G_τ, Q_τ from equations for $\dot{G}$ and $\dot{Q}$ to the first equation and assumed the coupling rate $\epsilon\eta$ small, so it does not substantially change the pulse shapes:

$$\begin{aligned}
\dot{A}_1 + \gamma A_1 + i\omega A_1 &= \gamma\sqrt{\kappa}e^{(1-i\alpha_g)G_{1\tau}/2-(1-i\alpha_q)Q_{1\tau}/2-i\vartheta}A_{1\tau} + 2\epsilon\eta e^{i\varphi}A_2, \\
\dot{G}_1 &= G_0 - \gamma_g G_1 - e^{-Q_1}(e^{G_1}-1)|A_1|^2, \\
\dot{Q}_1 &= Q_0 - \gamma_q Q_1 - s(1-e^{-Q_2})|A_1|^2. \\
\dot{A}_2 + \gamma A_2 + i\omega A_2 &= \gamma\sqrt{\kappa}e^{(1-i\alpha_g)G_{2\tau}/2-(1-i\alpha_q)Q_{2\tau}/2-i\vartheta}A_{2\tau} + 2\epsilon\eta e^{i\varphi}A_1, \\
\dot{G}_2 &= G_0 - \gamma_g G_2 - e^{-Q_2}(e^{G_2}-1)|A_2|^2, \\
\dot{Q}_1 &= Q_0 - \gamma_q Q_2 - s(1-e^{-Q_2})|A_2|^2.
\end{aligned} \tag{5.4.1}$$

In the calculations that follow, we consider the model equations for the first laser and assume $A := A_1, G := G_1, Q := Q_1$ etc.

We introduce time scales $t_0 = t$ and $t_1 = \varepsilon t$ with operators $D_0 = \frac{\partial}{\partial t_0}$, $D_1 = \frac{\partial}{\partial t_1}$ and look for solutions in the form $A(t_0,t_1) = A^0(t_0,t_1) + \varepsilon A^1(t_0,t_1)$, $G = G^0(t_0,t_1) + \varepsilon G^1(t_0,t_1)$, $Q = Q^0(t_0,t_1) + \varepsilon Q^1(t_0,t_1)$, and $\dot{A} = D_0 A + \varepsilon D_1 A$, $\dot{G} = D_0 G + \varepsilon D_1 G$, $\dot{Q} = D_0 Q + \varepsilon D_1 Q$. Then we expand the equations by t_1 following [83, 165] and obtain the unperturbed equation in $\mathcal{O}(1)$:

$$\begin{aligned}
D_0 A^0 + (\gamma + i\omega)\, A^0 &= \\
= \gamma\sqrt{\kappa}e^{((1-i\alpha_g)G^0(t_0-\tau,t1)-(1-i\alpha_q)Q^0(t_0-\tau,t_1))/2-i\vartheta}A^0(t_0-\tau,t_1), \\
D_0 G^0 = g_0 - \gamma_g G^0 - e^{-Q^0}(e^{G^0}-1)|A^0|^2, \\
D_0 Q^0 = q_0 - \gamma_q Q^0 - (1-e^{-Q^0})|A^0|^2.
\end{aligned}$$

and equations for the first order correction in $\mathcal{O}(\epsilon)$:

$$\begin{aligned}
D_0 A^1 + D_1 A^0 + (\gamma + i\omega)\, A^1 &= \gamma\sqrt{\kappa}e^{((1-i\alpha_g)G^0_\tau-(1-i\alpha_q)Q^0_\tau)/2-i\vartheta} \\
\big[A^1_\tau - \tau D_1 A^0_\tau + A^0_\tau((1-i\alpha_g)/2(G^1_\tau - \tau D_1 G^0_\tau) - (1-i\alpha_q)/2(Q^1_\tau - \tau D_1 Q^0_\tau))\big] + \\
+ 2\eta e^{i\varphi}A_2,
\end{aligned}$$

$$\begin{aligned}
D_0 G^1 + D_1 G^0 = -\gamma_g G^1 - e^{-Q^0}(|A^0|^2 Q^1 - (A^0 A^{1*} + A^1 A^{0*}) + \\
+ e^{G^0}(|A^0|^2(G^1 - Q^1) + (A^0 A^{1*} + A^1 A^{0*}))), \\
D_0 Q^1 + D_1 Q^0 = -\gamma_q Q^1 - \\
- s(e^{-Q^0}(|A^0|^2 Q^1 - (A^0 A^{1*} + A^1 A^{0*})) + (A^0 A^{1*} + A^1 A^{0*})).
\end{aligned}$$

Here, we assume $\mathcal{A}, \mathcal{G}, \mathcal{Q}$ as a T-periodic solution of unperturbed equation, then $A^0 = e^{i\phi_1(t_1)}\mathcal{A}(t_0 + \theta_1(t_1))$, $G^0 = \mathcal{G}(t_0 + \theta_1(t_1)), Q^0 = \mathcal{Q}(t_0 + \theta_1(t_1))$. The same way we replace A^1, Q^1, G^1 with $e^{i\phi_1(t_1)}A^1(t_0 + \theta_1(t_1), t_1)$. The first equation is split

into the real and imaginary parts, assuming $A^1 = B + iC$, and $\mathcal{A} = \mathcal{B} + i\mathcal{C}$. For the second laser amplitude profile, the unperturbed solution is written down as $A_2^0 = e^{i\phi_2(t_1)}\mathcal{A}_2(t_0+\theta_2(t_1))$, where $\mathcal{A}_2 = \mathcal{B}_2+i\mathcal{C}_2$ and the following set of equations is obtained:

(5.4.2)
$$\begin{aligned} D_0 B + \gamma B + \omega C - \gamma\sqrt{\kappa}e^{(\mathcal{G}_\tau-\mathcal{Q}_\tau)/2}((2B_\tau + (\mathcal{B}_\tau + \alpha_g\mathcal{C}_\tau)G_\tau^1 - \\ (\mathcal{B}_\tau + \alpha_q\mathcal{C}_\tau)Q_\tau^1)\cos((\alpha_g\mathcal{G}_\tau - \alpha_q\mathcal{Q}_\tau)/2 + \vartheta) + \\ (2C_\tau + (\mathcal{C}_\tau - \alpha_g\mathcal{B}_\tau)G_\tau^1 - (\mathcal{C}_\tau - \alpha_q\mathcal{B}_\tau)Q_\tau^1)\sin((\alpha_g\mathcal{G}_\tau - \alpha_q\mathcal{Q}_\tau)/2 + \vartheta))/2 = \\ -\dot\theta_1(\dot{\mathcal{B}} + \tau(\ddot{\mathcal{B}} + \gamma\dot{\mathcal{B}} - \omega\dot{\mathcal{C}})) + \dot\phi_1(\mathcal{C} + \tau(\dot{\mathcal{C}} + \gamma\mathcal{C} + \omega\mathcal{B})) \\ +2\eta(\cos(\varphi+\Phi)\mathcal{B}_2 - \sin(\varphi+\Phi)\mathcal{C}_2), \end{aligned}$$

(5.4.3)
$$\begin{aligned} D_0 C + \gamma C - \omega B - \gamma\sqrt{\kappa}e^{(\mathcal{G}_\tau-\mathcal{Q}_\tau)/2}(-(2B_\tau + (\mathcal{B}_\tau + \alpha_g\mathcal{C}_\tau)G_\tau^1 - \\ (\mathcal{B}_\tau + \alpha_q\mathcal{C}_\tau)Q_\tau^1)\sin((\alpha_g\mathcal{G}_\tau - \alpha_q\mathcal{Q}_\tau)/2 + \vartheta) + \\ (2C_\tau + (\mathcal{C}_\tau - \alpha_g\mathcal{B}_\tau)G_\tau^1 - (\mathcal{C}_\tau - \alpha_q\mathcal{B}_\tau)Q_\tau^1)\cos((\alpha_g\mathcal{G}_\tau - \alpha_q\mathcal{Q}_\tau)/2 + \vartheta))/2 = \\ -\dot\theta_1(\dot{\mathcal{C}} + \tau(\ddot{\mathcal{C}} + \gamma\dot{\mathcal{C}} + \omega\dot{\mathcal{B}})) - \dot\phi_1(\mathcal{B} + \tau(\dot{\mathcal{B}} + \gamma\mathcal{B} - \omega C)) \\ +2\eta(\cos(\varphi+\Phi)\mathcal{C}_2 + \sin(\varphi+\Phi)\mathcal{B}_2), \end{aligned}$$

(5.4.4)
$$\begin{aligned} D_0 G^1 + (\gamma_g + e^{\mathcal{G}-\mathcal{Q}}(\mathcal{B}^2+\mathcal{C}^2))G^1 + e^{-\mathcal{Q}}((\mathcal{B}^2+\mathcal{C}^2)(1-e^{\mathcal{G}})Q^1 + \\ 2(e^{\mathcal{G}}-1)(\mathcal{B}B + C\mathcal{C})) = -\dot\theta_1\dot{\mathcal{G}}, \end{aligned}$$

(5.4.5)
$$\begin{aligned} D_0 Q^1 + (\gamma_q + se^{-\mathcal{Q}}(\mathcal{B}^2+\mathcal{C}^2))Q^1 + 2s(1-e^{-\mathcal{Q}})(\mathcal{B}B + C\mathcal{C}) = \\ -\dot\theta_1\dot{\mathcal{Q}}, \end{aligned}$$

where the phase difference between lasers is denoted by $\Phi = \phi_2 - \phi_1$. The time separation $\Theta = \theta_2 - \theta_1$ is introduced in the same manner.

Equations (5.4.2)-(5.4.5) together with the same equations for the second laser form the following linear system of delay differential equations for the vector of perturbations $S_j = (\mathrm{Re}\, A_j^1, \mathrm{Im}\, A_j^1, G_j^1, Q_j^1)^T$:

(5.4.6)
$$\begin{aligned} -\dot S_j + a_1(t)\,S_j(t) + a_2(t)S_j(t-\tau) = \\ a_3\dot\theta_j + a_4\dot\phi_j + \mathcal{R}\left((-1)^j\Theta, (-1)^j\Phi\right), \end{aligned}$$

$j = 1, 2$, with linear operators $a_{1,2}$ and vector functions $a_{3,4}$ depending only on the unperturbed pulse solution $\mathcal{B}, \mathcal{C}, \mathcal{G}, \mathcal{Q}$. Expressions for $a_{1,2,3,4}$ and $\mathcal{R}$ are given below.

The linear operators a_1,a_2 in Eq. (2) read:

$$a_1 = \begin{pmatrix} -\gamma & \omega & 0 & 0 \\ -\omega & -\gamma & 0 & 0 \\ -2e^{-\mathcal{Q}}(e^{\mathcal{G}}-1)\mathcal{B} & -2e^{-\mathcal{Q}}(e^{\mathcal{G}}-1)\mathcal{C} & -\gamma_g - & e^{-\mathcal{Q}}(\mathcal{B}^2+\mathcal{C}^2) \\ & & -e^{\mathcal{G}-\mathcal{Q}}(\mathcal{B}^2+\mathcal{C}^2) & (e^{\mathcal{G}}-1) \\ -2s(1-e^{-\mathcal{Q}})\mathcal{B} & -2s(1-e^{-\mathcal{Q}})\mathcal{C} & 0 & -\gamma_q - se^{-\mathcal{Q}} \\ & & & (\mathcal{B}^2+\mathcal{C}^2) \end{pmatrix},$$

and $a_2 = \tilde{M}\gamma\sqrt{\kappa}e^{(\mathcal{G}-\mathcal{Q})/2}/2$, where

$$\tilde{M} = \begin{pmatrix} 2\cos\alpha & 2\sin\alpha & (\mathcal{B}+\alpha_g\mathcal{C})\cos\alpha + & -(\mathcal{B}+\alpha_q\mathcal{C})\cos\alpha - \\ & & +(\mathcal{C}-\alpha_g\mathcal{B})\sin\alpha & -(\mathcal{C}-\alpha_q\mathcal{B})\sin\alpha \\ -2\sin\alpha & 2\cos\alpha & -(\mathcal{B}+\alpha_g\mathcal{C})\sin\alpha + & (\mathcal{B}+\alpha_q\mathcal{C})\sin\alpha - \\ & & +(\mathcal{C}-\alpha_g\mathcal{B})\cos\alpha & -(\mathcal{C}-\alpha_q\mathcal{B})\cos\alpha \\ 0 & 0 & 0 & 0 \\ 0 & 0 & 0 & 0 \end{pmatrix},$$

while $\alpha = (\alpha_g\mathcal{G} - \alpha_q\mathcal{Q})/2 + \vartheta$ and $\mathcal{B} = \mathrm{Re}\,\mathcal{A}, \mathcal{C} = \mathrm{Im}\,\mathcal{A}, \mathcal{G}, Q$ are the profiles of the solution of uncoupled system (1) for one laser.

The vector functions a_3,a_4 in Eq. (2) read:

$$a_3 = \begin{pmatrix} -\dot{\mathcal{B}} - \tau(\ddot{\mathcal{B}} + \gamma\dot{\mathcal{B}} - \omega\dot{\mathcal{C}}) \\ -\dot{\mathcal{C}} - \tau(\ddot{\mathcal{C}} + \gamma\dot{\mathcal{C}} + \omega\dot{\mathcal{B}}) \\ -\dot{\mathcal{G}} \\ -\dot{\mathcal{Q}} \end{pmatrix}, \quad a_4 = \begin{pmatrix} \mathcal{C} + \tau(\dot{\mathcal{C}} + \gamma\mathcal{C} + \omega\mathcal{B}) \\ -\mathcal{B} - \tau(\dot{\mathcal{B}} + \gamma\mathcal{B} - \omega C) \\ 0 \\ 0 \end{pmatrix},$$

and

$$\mathcal{R} = \begin{pmatrix} 2\eta\left(\cos(\varphi+\Phi)\,\mathcal{B}(t+\Theta) - \sin(\varphi+\Phi)\,\mathcal{C}(t+\Theta)\right) \\ 2\eta\left(\cos(\varphi+\Phi)\,\mathcal{C}(t+\Theta) + \sin(\varphi+\Phi)\,\mathcal{B}(t+\Theta)\right) \\ 0 \\ 0 \end{pmatrix}.$$

Next, the Fredholm alternative (see Theorem 9) is applied. The solvability condition (for bounded solutions) of the linear non-homogeneous system (5.4.6) requires that its right hand side is orthogonal to the neutral (or Goldstone) modes of the adjoint homogenous system, see [28, 65, 34] and Appendix B. In the case of small coupling coefficient, $\eta \ll 1$, these modes can be approximated by $\psi_j^\dagger$ and $\xi_j^\dagger$ with $j = 1, 2$, that are related to the phase shift and the time-shift invariance of the model equations. These modes can be found numerically (see, e.g. [83, 165]). The orthogonality condition of the right hand side of (5.4.6) to $\psi_{1,2}^\dagger$ with respect to the inner product $(u, v) = \int_0^T u(t)v(t)dt$ [28] reads

$$\int_0^T \left(a_3\dot{\theta}_j + a_4\dot{\phi}_j + \mathcal{R}\left((-1)^j\Theta, (-1)^j\Phi\right)\right)\psi_j^\dagger(t)dt = 0$$

and leads to the system of two ordinary differential equations

$$p_\psi\dot{\theta}_1 + q_\psi\dot{\phi}_1 = \mu R_\psi(\Theta, \Phi), \tag{5.4.7}$$

$$p_\psi\dot{\theta}_2 + q_\psi\dot{\phi}_2 = \mu R_\psi(-\Theta, -\Phi), \tag{5.4.8}$$

where coefficients p_ψ, q_ψ, and R_ψ are given by the corresponding scalar products later in the text. Subtracting equations (5.4.7) and (5.4.8) from one another, one obtains the equation for the phase difference Φ and time separation of the pulses Θ:

$$p_\psi\dot{\Theta} + q_\psi\dot{\Phi} = \mu\left(R_\psi(-\Theta,-\Phi) - R_\psi(\Theta,\Phi)\right). \tag{5.4.9}$$

In the same way, the orthogonality conditions to the modes $\xi^\dagger_{1,2}$ lead to the equation

$$p_\xi\dot{\Theta} + q_\xi\dot{\Phi} = \mu\left(R_\xi(-\Theta,-\Phi) - R_\xi(\Theta,\Phi)\right). \tag{5.4.10}$$

The coefficients in Eqs. (5.4.9) and (5.4.10) read:

$$p_\psi = \tau\left[\left\langle\ddot{\mathcal{B}} + \gamma\dot{\mathcal{B}} - \omega\dot{\mathcal{C}}, \psi_1^\dagger\right\rangle + \left\langle\ddot{\mathcal{C}} + \gamma\dot{\mathcal{C}} + \omega\dot{\mathcal{B}}, \psi_2^\dagger\right\rangle\right], \tag{5.4.11}$$

$$q_\psi = \left[\left\langle -\mathcal{C} - \tau\left(\dot{\mathcal{C}} + \gamma\mathcal{C} + \omega\mathcal{B}\right), \psi_1^\dagger\right\rangle + \left\langle\mathcal{B} + \tau\left(\dot{\mathcal{B}} + \gamma\mathcal{B} - \omega\mathcal{C}\right), \psi_2^\dagger\right\rangle\right], \tag{5.4.12}$$

(5.4.13)
$$R_\psi(\Theta,\Phi) = 2\eta\left[\cos(\varphi+\Phi)(\langle\mathcal{B}_2,\psi_1^\dagger\rangle + \langle\mathcal{C}_2,\psi_2^\dagger\rangle) + \sin(\varphi+\Phi)(\langle\mathcal{B}_2,\psi_2^\dagger\rangle - \langle\mathcal{C}_2,\psi_1^\dagger\rangle)\right],$$

and

(5.4.14)
$$p_\xi = \left\langle\dot{\mathcal{B}} + \tau(\ddot{\mathcal{B}} + \gamma\dot{\mathcal{B}} - \omega\dot{\mathcal{C}}), \xi_1^\dagger\right\rangle + \left\langle\dot{\mathcal{C}} + \tau(\ddot{\mathcal{C}} + \gamma\dot{\mathcal{C}} + \omega\dot{\mathcal{B}}), \xi_2^\dagger\right\rangle + \left\langle\dot{\mathcal{G}}, \xi_3^\dagger\right\rangle + \left\langle\dot{\mathcal{Q}}, \xi_4^\dagger\right\rangle,$$

$$q_\xi = \tau\left[\left\langle -\dot{\mathcal{C}} - \omega\mathcal{B}, \xi_1^\dagger\right\rangle + \left\langle\dot{\mathcal{B}} - \omega\mathcal{C}, \xi_2^\dagger\right\rangle\right], \tag{5.4.15}$$

(5.4.16)
$$R_\xi(\Theta,\Phi) = 2\eta\left[\cos(\varphi+\Phi)(\langle\mathcal{B}_2,\xi_1^\dagger\rangle + \langle\mathcal{C}_2,\xi_2^\dagger\rangle) + \sin(\varphi+\Phi)(\langle\mathcal{B}_2,\xi_2^\dagger\rangle - \langle\mathcal{C}_2,\xi_1^\dagger\rangle)\right].$$

Solving now (5.4.9) and (5.4.10) for $\dot{\Theta}$ and $\dot{\Phi}$, one can obtain the reduced system of two ordinary differential equations for the slow time evolution of Θ and Φ:

$$\begin{aligned}\dot{\Theta} &= \frac{2\eta}{p_\psi q_\xi - p_\xi q_\psi}\sqrt{(c_1^2+c_2^2)}\cos\left(\Phi - \arctan c_1/c_2\right),\\ \dot{\Phi} &= \frac{2\eta}{p_\psi q_\xi - p_\xi q_\psi}\sqrt{(c_3^2+c_4^2)}\sin\left(\Phi + \pi/2 - \arctan c_3/c_4\right),\end{aligned} \tag{5.4.17}$$

where

$$\begin{aligned}c_1 &= \left[\left(b_8-b_6\right)q_\psi + \left(b_2-b_4\right)q_\xi\right]\cos\varphi - \left[\left(b_7-b_5\right)q_\psi + \left(b_1-b_3\right)q_\xi\right]\sin\varphi,\\ c_2 &= \left[-\left(b_5+b_7\right)q_\psi + \left(b_1+b_3\right)q_\xi\right]\cos\varphi - \left[\left(b_6+b_8\right)q_\psi - \left(b_2+b_4\right)q_\xi\right]\sin\varphi,\\ c_3 &= \left[\left(b_6-b_8\right)p_\psi - \left(b_2-b_4\right)p_\xi\right]\cos\varphi + \left[\left(b_7-b_5\right)p_\psi + \left(b_1-b_3\right)p_\xi\right]\sin\varphi,\\ c_4 &= \left[\left(b_5+b_7\right)p_\psi - \left(b_1+b_3\right)p_\xi\right]\cos\varphi + \left[\left(b_6-b_8\right)p_\psi - \left(b_2+b_4\right)p_\xi\right]\sin\varphi,\end{aligned}$$

and

$$b_1 = -\langle \mathcal{B}(t+\Theta), \psi_1 \rangle - \langle \mathcal{C}(t+\Theta), \psi_2 \rangle, b_2 = \langle \mathcal{C}(t+\Theta), \psi_1 \rangle - \langle \mathcal{B}(t+\Theta), \psi_2 \rangle,$$
$$b_3 = \langle \mathcal{B}(t-\Theta), \psi_1 \rangle + \langle \mathcal{C}(t-\Theta), \psi_2 \rangle, b_4 = -\langle \mathcal{C}(t-\Theta), \psi_1 \rangle + \langle \mathcal{B}(t-\Theta), \psi_2 \rangle,$$
$$b_5 = -\langle \mathcal{B}(t+\Theta), \xi_1 \rangle - \langle \mathcal{C}(t+\Theta), \xi_2 \rangle, b_6 = \langle \mathcal{C}(t+\Theta), \xi_1 \rangle - \langle \mathcal{B}(t+\Theta), \xi_2 \rangle,$$
$$b_7 = \langle \mathcal{B}(t-\Theta), \xi_1 \rangle + \langle \mathcal{C}(t-\Theta), \xi_2 \rangle, b_8 = -\langle \mathcal{C}(t-\Theta), \xi_1 \rangle + \langle \mathcal{B}(t-\Theta), \xi_2 \rangle.$$

Finally, the reduced system (5.4.17) can be rewritten in a more convenient way as:

$$\begin{aligned} \dot{\Theta} &= \eta \cos\left(\Phi + \Delta_\Theta(\Theta)\right) f_\Theta(\Theta), \\ \dot{\Phi} &= \eta \sin\left(\Phi + \Delta_\Phi(\Theta)\right) f_\Phi(\Theta), \end{aligned} \tag{5.4.18}$$

where $f_{\Theta,\Phi}(\Theta)$ are non-negative functions. Note that the specific shape of the right hand side of (5.4.18) is due to the fact that the functions $R_{\psi,\xi}(\Theta,\Phi)$ contain only first Fourier harmonic in Φ.

The bound pulse train states correspond to the fixed points of the system (5.4.18). These points, lying on the intersection of nullclines of (5.4.18), are defined by the condition $\cos\left(\Phi + \Delta_\Theta(\Theta)\right) = \sin\left(\Phi + \Delta_\Phi(\Theta)\right) = 0$, which implies that one of the two conditions should be satisfied, $\Delta_\Theta(\Theta) = \Delta_\Phi(\Theta)$, or $\Delta_\Theta(\Theta) = \Delta_\Phi(\Theta) + \pi$. The first condition corresponds to the saddles of the system (5.4.18), while the second equation corresponds either to nodes or to foci. Figure 5.4.6(a) shows intersecting nullclines of system (5.4.18) in the (Θ,Φ) phase plane. Here, blue filled (unfilled) circles depict stable (unstable) nodes, red filled (unfilled) circles correspond to stable (unstable) foci, and blue squares – to saddles. All of these equilibria correspond to pulse bound states in system (5.2.1) with the same stability properties. Note that a particular case $\Theta = 0$ corresponds to the synchronized pulses with the zero time separation, when the system (5.4.18) transforms into a single equation $\dot{\Phi} = \mu C_\Phi \sin\Phi$, which admits either in-phase $\Phi = 0$ or anti-phase synchronization $\Phi = \pi$ as it was mentioned above.

Noteworthy, the reduced system (5.4.18) resembles the equations governing the slow dynamics of the distance and phase difference between two interacting dissipative solitons in spatially extended systems described by generalized complex Ginzburg-Landau equation on an unbounded domain [82, 81, 166, 167]. The case of coupled lasers, however, is distinct in two aspects: (i) unlike the case of complex Ginzburg-Landau equation the presence of the phase shifts $\Delta_{\Theta,\Phi}(\Theta)$ in Eqs. (5.4.18) allows for the existence of bound states with the Θ-dependent phase difference between the pulses different from 0, π, and $\pm\pi/2$, and (ii) instead of a countable set of equidistant roots, the functions $f_{\Theta,\Phi}(\Theta)$ have no roots at all, which means that in laser arrays there is a finite number of bound states which are distributed along the Θ-axis in a more complex manner.

The 2D phase plane diagram of the reduced system of equations (5.4.18) is presented in Fig. 5.4.4, where the equilibria and their basins of attraction are shown. Note, that due to the symmetry $(\Theta,\Phi) \to (-\Theta,-\Phi)$ it is sufficient to show only the left half of the coordinate system (Θ,Φ). Here, the point **C1** corresponds to a

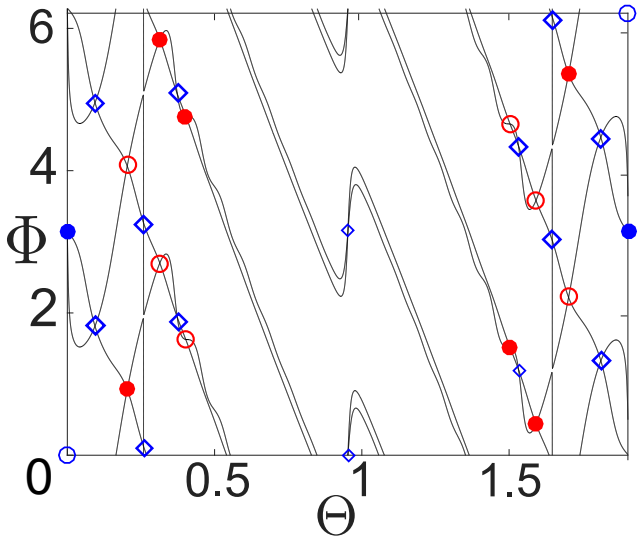

FIGURE 5.4.3. (a) Fixed points and nullclines for the reduced system (5.4.18) in the coordinate plane (Θ, Φ) calculated for coupling phase $\varphi = 3.0$. Blue filled (empty) circles correspond to stable (unstable) nodes, red filled (empty) circles to stable (unstable) foci, whereas blue empty diamonds to saddles.

stable anti-phase synchronized solution, while points **B1**, **B2**, and **B3** indicate the bound states with nonzero pulse time separations Θ and phase shifts Φ between the pulse intensity maxima. Figure 5.4.4 shows the case of $\varphi = 3.0$. The basins of attraction of the stable states are separated by saddles and, interestingly, they can wind into spiral sources as it is shown in the inset of Fig. 5.4.4.

For other values of φ, there can co-exist from two to five stable equilibria corresponding to distinct bound states, see Fig. (5.4.5), where it is easy to observe the symmetry $(\Theta, \Phi) \to (-\Theta, -\Phi)$. Note that for some region in the coupling phase parameter both in-phase and anti-phase synchronized solutions are unstable, while the pulse bound states are stable, see Fig. (5.4.5), top panel. The video showing the position of the equilibria and corresponding basins of attraction for different values of φ is available as a Supplemental material for the article [168] and its preprint at *arXiv:1706.08802 [nlin.PS]*.

5.4.3. Bifurcation diagram for bound pulse trains

A more detailed stability analysis of the bound state corresponding to the equilibrium **B1** is performed numerically using the path continuation software DDE-BIFTOOL [169] applied to the model equations (5.2.1). Note that the software does not allow to follow the bifurcation of synchronized solution to obtain the bound pulse train state. In order for DDE-BIFTOOL to converge to the bound pulse train solution, one should start with directly computed initial solution profile on a very fine grid (> 750 points). The bifurcation diagram showing the domain of stability of this bound state is presented in Fig. 5.4.6. Here, red line **P** corresponds to a subcritical pitchfork bifurcation from the in-phase synchronized

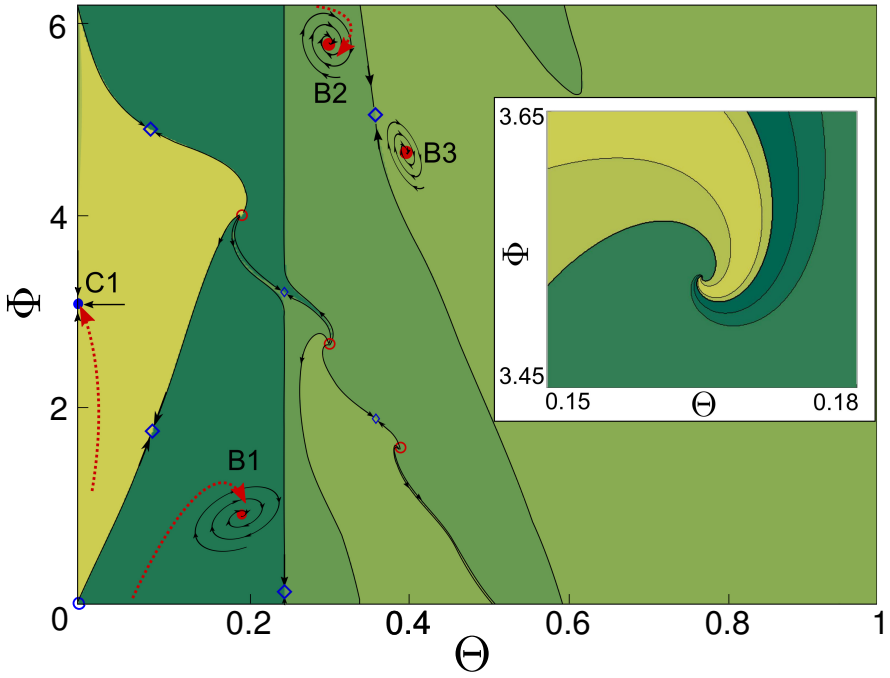

FIGURE 5.4.4. Stable equilibria and their basins of attraction on the phase plane of the reduced system (5.4.18) for coupling phase $\varphi = 3.0$. **C1** corresponds to the stable anti-phase synchronized solution. Equilibria **B1**, **B2**, and **B3** correspond to bound states with increasing time separation Θ, which have different phase shifts Φ between pulse intensity maxima. Inset: An example of the intertwining basins of attraction of five stable bound states in the vicinity of a spiral source for the reduced system (5.4.18) for $\varphi = 3.99$.

solution, whereas the blue **F** line corresponds to a fold bifurcation leading to the appearance of unstable bound state solutions. The dashed black line **T** shows the first torus bifurcation of pulse bound state solution which leads to a slight change of the pulse shapes from one pulse period to another, while the period of the pulsing remains the same.

5.4.4. Bound pulse trains for a ring of N mode-locked lasers

Our aim in this section is to present a reduced system describing bound pulse trains with arbitrary number of pulses N and to compare the results of the analysis of this system with numerical simulations. Let θ_j and ϕ_j be the time coordinate and phase of the mode-locked pulse in the j-th laser. Time separations and phase differences of the pulses in two adjacent lasers are denoted by $\Theta_j = \theta_{j+1} - \theta_j$ and $\Phi_j = \phi_{j+1} - \phi_j$ respectively. We assume that the total length of the bound pulse train is sufficiently shorter than the pulse repetition period. In this case, since the pulse interaction strength decays exponentially with the distance Θ, the interaction between the first and the last pulses can be neglected. It means that the first ($j = 1$) and the last ($j = N$) pulses are each interacting only with a

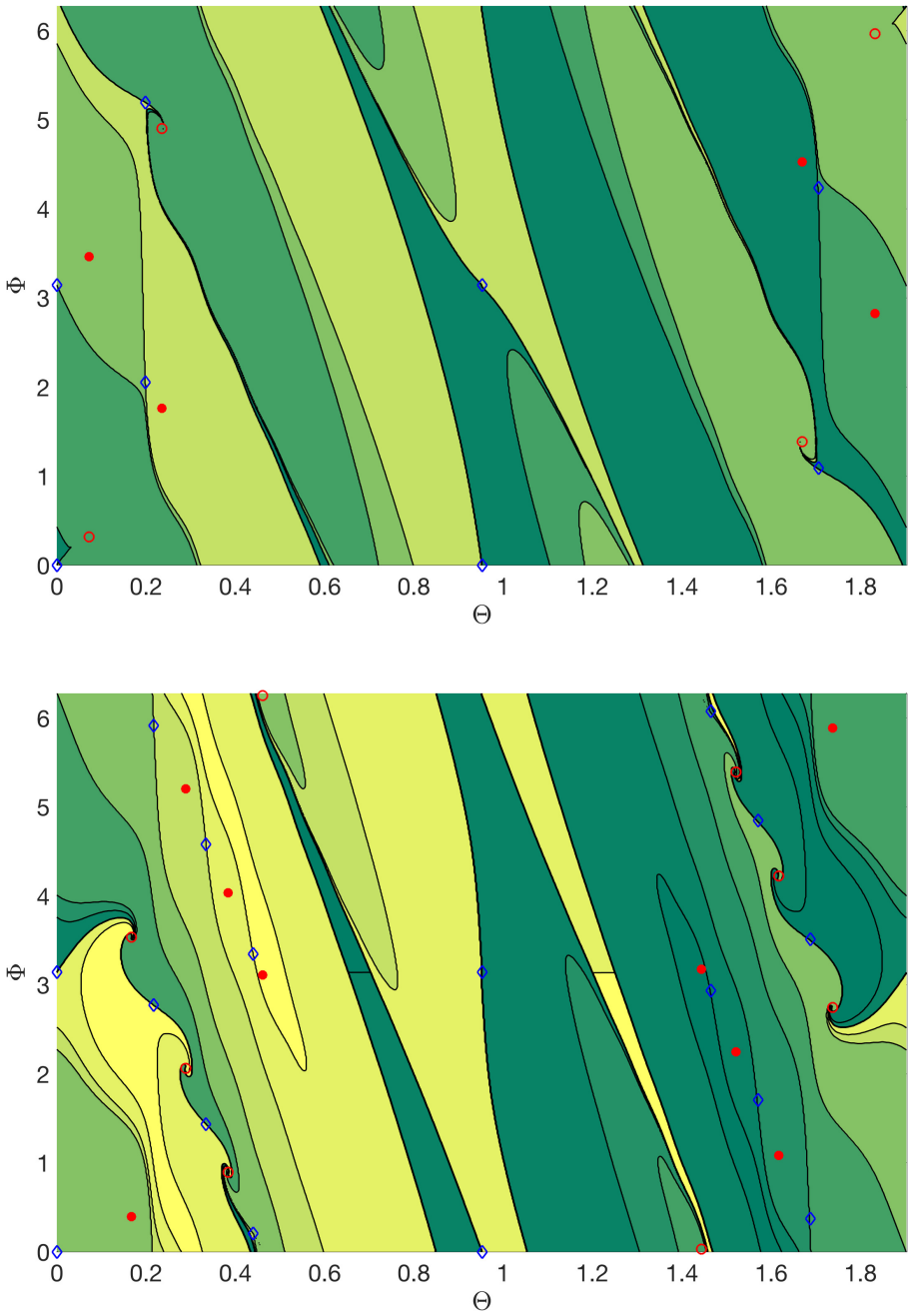

FIGURE 5.4.5. The equilibria and basins of attraction on the phase plane of the reduced system (5.4.18) for coupling phases $\varphi = 1.73$ on a top and $\varphi = 5.73$ on a bottom panel. Blue filled (empty) circles correspond to stable (unstable) nodes, red filled (empty) circles to stable (unstable) foci, whereas blue empty diamonds to saddles.

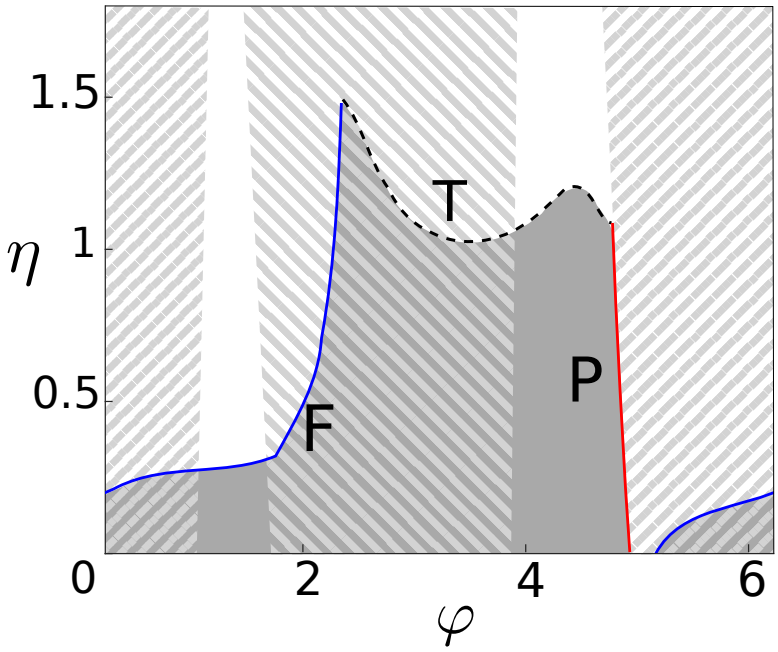

FIGURE 5.4.6. Bifurcation diagram for the bound state **B1** (cf. Fig. 5.4.4) in the plane (φ, η). Light gray area shows the stability domain of the bound state. Red line **P** corresponds to a subcritical pitchfork bifurcation of the in-phase synchronized solution, blue line **F** corresponds to a fold bifurcation, and dashed black line **T** indicates the first torus bifurcation. Left- and right-inclined hatching indicates the stability domains of in-phase and anti-phase synchronized solutions from Fig. 5.3.2.

single pulse ($j = 2$ and $j = N - 1$, respectively). Therefore, reduced equations describing the interaction of bound N-pulse train can be written in the form

$$\begin{aligned} p_{\psi,\xi}\dot{\Theta}_1 + q_{\psi,\xi}\dot{\Phi}_1 &= R_{\psi,\xi}(\Theta_2, \Phi_2) + R_{\psi,\xi}(-\Theta_1, -\Phi_1) - R_{\psi,\xi}(\Theta_1, \Phi_1), \\ p_{\psi,\xi}\dot{\Theta}_j + q_{\psi,\xi}\dot{\Phi}_j &= R_{\psi,\xi}(\Theta_{j+1}, \Phi_{j+1}) + R_{\psi,\xi}(-\Theta_j, -\Phi_j) - \\ &- R_{\psi,\xi}(\Theta_j, \Phi_j) - R_{\psi,\xi}(-\Theta_{j-1}, -\Phi_{j-1}),\ j = 2, \ldots, N-2, \\ p_{\psi,\xi}\dot{\Theta}_{N-1} + q_{\psi,\xi}\dot{\Phi}_{N-1} &= R_{\psi,\xi}(-\Theta_{N-1}, -\Phi_{N-1}) - R_{\psi,\xi}(\Theta_{N-1}, \Phi_{N-1}) - \\ &- R_{\psi,\xi}(-\Theta_{N-2}, -\Phi_{N-2}), \end{aligned} \tag{5.4.19}$$

where $p_{\psi,\xi}$, $q_{\psi,\xi}$, and $R_{\psi,\xi}$ are defined by (5.4.11)-(5.4.16). Note that since the right hand side of this system is block-diagonal, it can be easily resolved with respect to $\dot{\Theta}_j$ and $\dot{\Phi}_j$. For a bound pulse train, all $\dot{\Theta}_j$ and $\dot{\Phi}_j$ are equal to zero. It gives us $2(N-1)$ implicit equations for $2(N-1)$ variables $\Theta_j, \Phi_j,\ j = 1, \ldots, N-1$. We have solved reduced system of equations (5.4.19) for different $N = 2, \ldots, 11$ and fixed values of coupling parameters $\eta = 0.5$ and $\varphi = 4.0$. Figure 5.4.7(a,b) shows that maximal, minimal, and mean values of time separations Θ and phase differences Φ between the pulses in bound pulse trains do not change considerably with the number of lasers N. Therefore, qualitatively the phenomenon of bound

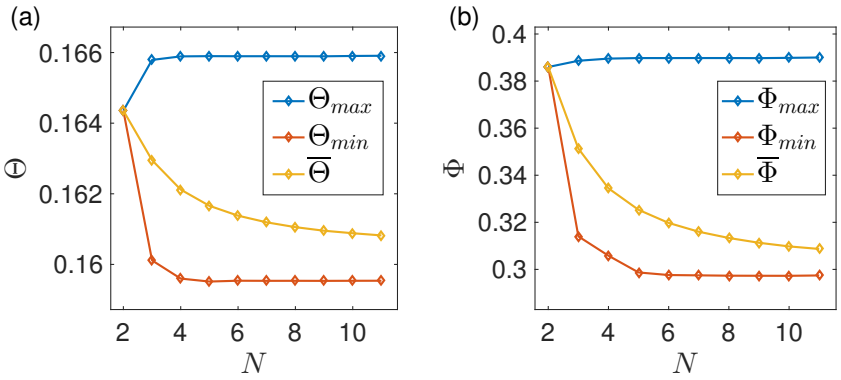

FIGURE 5.4.7. Maximal Θ_{max}, minimal Θ_{min}, and mean $\bar{\Theta}$ values of pulse time separations Θ (a) and maximal Φ_{max}, minimal Φ_{min}, and mean $\bar{\Phi}$ values of phase difference Φ in the bound pulse train solutions as functions of the number of lasers N. Coupling parameters: $\eta = 0.5$ and $\varphi = 4.0$. Other parameters have the same values as in the manuscript.

pulse train formation can be understood in terms of pairwise interaction between two lasers. The values obtained by solution of reduced system (5.4.19) are in agreement with the separations calculated by direct numerical integration of the model equations (5.2.1) for seven lasers, see Fig. 5.4.8.

5.5. Discussion

In this Chapter, we have investigated the dynamics in a ring of coupled pulse generators in a form of a ring of mode-locked lasers. First, the available amplitude synchronized solutions in the systems were described and their stability and bifurcations were investigated [168]. The mode-locked bound pulse train regimes bifurcating from the synchronized solutions were discovered. In these regimes trains of mode-locked pulses emitted by individual lasers are bound by local interaction, forming the closely packed pulse clusters. In the limit of small coupling strength asymptotic equations were derived governing the slow time evolution positions and phases of the interacting pulses in an array consisting of two lasers. The pulse separations and phase differences between the pulses in bound states as well as basins of attraction of different bound states calculated using this semi-analytical approach are in good agreement with the results of direct numerical simulations of the model equations (5.2.1). The stability and bifurcations of bound pulse train regime were studied numerically with the path-following technique.

The important feature of the newly found pulse bound states is that, in contrast to the pulse bound state operation regimes predicted and observed experimentally in fiber lasers [170, 171, 89, 172, 173, 174, 175, 176, 177, 178, 179, 180, 181, 182], this regime cannot exist in a solitary mode-locked laser. Interaction of pulses in a solitary mode-locked semiconductor laser was theoretically studied in [183]

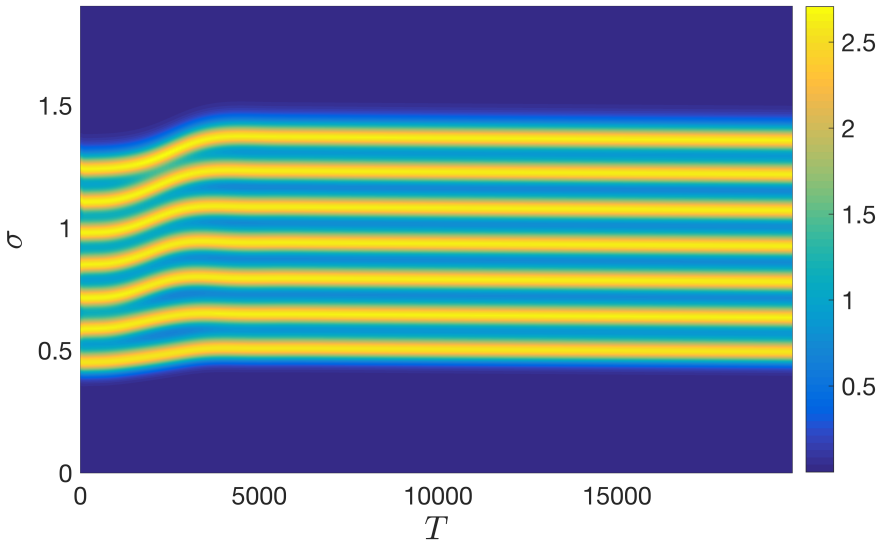

FIGURE 5.4.8. Space-time diagram of the bound pulse train regime in seven-laser array ($N = 7$) in coordinates (T, σ), where $\sigma = t \bmod \tau_0$ is the original fast time and $T = t/\tau_0$ the slow time ($\tau_0 = 1.9055$). Brighter colors indicate higher values of the sum of the laser intensities $\sum_{i=1}^{4} |A_i|^2$. Coupling parameters: $\eta = 0.5$ and $\varphi = 4.0$. Other parameters have the same values as in Fig. 1 of the manuscript.

and recently in [184], where it was shown that the repulsion of pulses due to the slow recovery of the carrier density in the gain medium usually results in generation of either one (fundamental mode-locking) or several equally spaced pulses (harmonic mode-locking) per cavity round trip time. On the contrary, in the same parameter domain the bound pulse train regime in a laser array is associated with the formation of closely packed in time bound states of coupled mode-locked pulses due to a balance between attraction and repulsion between the pulse trains emitted by individual lasers with the possibility to change the interval between the pulses via the variation of coupling phase parameter.

The bound states described in this Chapter have a similarity with rather well studied bound states of dissipative solitons in spatially extended systems, where multiple soliton clusters surrounded by a linearly stable homogeneous regime can be formed due to a similar mechanism of balancing between attraction and repulsion. However, unlike the bound states formed by dissipative solitons, the appearance of this new type of bound states is related to the presence of coupling between the neighboring lasers and it is impossible in a solitary passively mode-locked semiconductor laser, where zero intensity steady state is linearly unstable and pulse interaction is nonlocal and always repulsive. Furthermore, unlike the case of complex Ginzburg-Landau-type equations, the new bound pulse train regime can exhibit arbitrary phase differences between the pulses depending on

their time separation and correspond to a finite number of fixed points distributed non-equidistantly along the time axis. Since the physical mechanism of the bound state formation due to the coupling between neighboring lasers is quite general, it can be observed in other physical systems described by coupled sets of partial or delay differential equations, where pulse solutions are present. It leads to the conclusion that this phenomenon is generic and can be extended to other systems of spatially extended coupled pulse generators.

CHAPTER 6

Summary and Outlook

To conclude, in this Thesis, the dynamics in several types of spatially extended and coupled systems with delay was investigated, with the special emphasis on the behavior of localized structures and pulse solutions. The main results of the Thesis that address the questions and problems posed in the Introduction Chapter are:

- The effect of the delayed feedback on the spatially extended systems described by Ginzburg-Landau type equations was investigated. It was shown that the appearance of "tube" set of solutions is the universal phenomenon in the equations with large delay.
- The stability criteria were obtained for homogenous zero steady state and plane wave solutions in complex Ginzburg-Landau equation with delayed feedback.
- The influence of delayed feedback on the localized solutions in the laser with saturable absorber was investigated. An appearance of novel type of delay-induced modulational instability was demonstrated for the laser with saturable absorber, and cubic-quintic Ginzburg-Landau equation.
- The novel dynamical regime of bound pulse trains in the system of coupled pulse generators was observed and investigated analytically. A number of stable bound train solutions coexists with different amplitude synchronized solutions. The appearance of this new type of bound states is related to the presence of coupling between the neighboring lasers.
- Results were supported by path continuation with DDE-BIFTOOL as well as direct numerical simulation by the use of the package ODDTool which was developed for the purpose of this work.

It would be important to point out that the results of the Thesis are not singular and each of them resonates across other parts of the Thesis and other works in the scientific environment of nonlinear dynamics. The appearance of the tube of the delay induced modes demonstrated in this Thesis for different systems has a special impact, since it proves to be the universal phenomenon that extends to a wide class of solutions. The parametric description of the multitude of delay-induced solutions and their stability can serve for the analysis of large delay systems in general. Moreover, the newfound delay-induced modulational instability in PDEs is a universal phenomenon that can explain zigzagging soliton motion observed earlier experimentally. In addition, the results of analytical derivation of the appearance of bound pulses in systems of coupled mode-locked

lasers leads to believe that this phenomenon is fundamental for the systems of coupled pulse generators.

During the course of the work, the results were presented at a number of international conferences with mathematical and physical focus. The following papers were prepared for publication:

(1) M. Tlidi, A.G. Vladimirov, A. Pimenov, K. Panajotov, D. Puzyrev, S. Yanchuk, and S. Gurevich, *Delay Induced Instabilities of Cavity Solitons in Passive and Active Laser Systems.* Conference Paper: Conference on Lasers and Electro-Optics - International Quantum Electronics Conference, Optical Society of America, 2013, paper IG-P-12

(2) D. Puzyrev, S. Yanchuk, A.G. Vladimirov, and S.V. Gurevich, *Stability of plane wave solutions in complex Ginzburg-Landau equation with delayed feedback.* SIAM J. Appl. Dyn. Systems 13, 986-1009 (2014)

(3) A. G. Vladimirov, D. Puzyrev, S. Yanchuk, and S. V. Gurevich, *Instabilities of Laser Cavity Solitons Induced by Delayed Feedback.* Conference paper: European Conference on Lasers and Electro-Optics - European Quantum Electronics Conference, Optical Society of America, 2015, paper EF-P-4

(4) D. Puzyrev, A. G. Vladimirov, S. V. Gurevich, and S. Yanchuk, *Modulational instability and zigzagging of dissipative solitons induced by delayed feedback (Rapid Communication).* Phys. Rev. A 93, 041801(R) (2016)

(5) K. Panajotov, D. Puzyrev, A. G. Vladimirov, S. V. Gurevich, and M. Tlidi, *Impact of time-delayed feedback on spatiotemporal dynamics in the Lugiato-Lefever model.* Phys. Rev. A 93, 043835 (2016)

(6) D. Puzyrev, A. G. Vladimirov, A. Pimenov, S. V. Gurevich, and S. Yanchuk, *Pulse bound-state clusters in coupled mode-locked lasers.* Conference paper: European Conference on Lasers and Electro-Optics - European Quantum Electronics Conference, Optical Society of America, 2017, paper EF-2.4

(7) D. Puzyrev, A. G. Vladimirov, A. Pimenov, S. V. Gurevich, and S. Yanchuk, *Bound pulse trains in arrays of coupled spatially extended dynamical systems.* Phys. Rev. Lett. 119, 163901 (2017)

In addition, the numerical package ODDTool was used to perform numerical simulations for the following articles: [185, 186, 187, 188, 56].

The main results of this Thesis can be expanded to various physical models. Different methods, approaches and their combinations used in the Thesis can be helpful for the study of other dynamical systems with delay. For the further advancement of the results of this Thesis, one would propose the following possible outlook:

- The model of the mode-locked laser can be augmented by introducing the transversal spatial dimension. The coexistence of temporal localization and complex dynamical regimes in case of coupled oscillators suggests that it can serve as one of the staring points for the search for

three-dimensional localized light structures (laser bullets) in the spatially extended system.

- A desirable goal is to develop a general theoretical description of the appearance of the tube of delay-induced modes (external cavity modes) across different types of equations with large delay.
- As for the dynamics of localized structures in spatially distributed systems, the natural expansion of the results would be to increase the number of space dimensions and look for the behavior of different types of structures and patterns and their interactions. As for the control and stabilization of cavity solitons, more elaborate ways of delayed feedback control, e.g. including non-locality in space, increasing the number of delay times, or application of generalized Pyragas control can be foreseen.
- The ODDTool package would benefit from the text user interface (possibly in the form of scripts which generate the parameter file and C++ code for the right-hand side of equation) and/or introduction of graphical user interface. The other direction is parallelization for shared- and distributed- memory platforms, including GPU and hybrid computational units. Currently, there is an ongoing project on Python interface available at the link
  http://florianstelzer.eu/pyoddtool/.

Appendix A: ODDTool – Package for integration of delay ODEs and PDEs

This Appendix Chapter contains the description of software package for simulation of delay differential equations, which was created in Humboldt University of Berlin in collaboration with Leonhardt Luecken and Markus Kantner. The package is available under the link https://github.com/leoluecken/oddtool. We were motivated to create such a package by limited applicability of the existing ones (MATLAB solver `dde23`, Mathematica solver `NDSolve` and others) for the simulation of the dynamical systems with large delay times. Most of the existing tools were accumulating the whole solution interval in memory, while our tool gradually swaps the solution on the delay interval to disk, allowing to integrate the system for long time intervals. Another motivation was to create open-access software with respect to modern programming techniques, while most DDE solvers are not available in open access and have somewhat obsolete code. Our tool can be extended to deal with PDEs with delay by the appropriate discretization of the RHS of the equation and proved to be accurate and reliable. It can also be extended by introduction of small random fluctuation and small noise to the system.

7.1. Overview

ODDtool ("ODD" stands for "Ordinary Delay Differential equations") allows the integration of high dimensional delay differential equations involving many different or very large delays. In particular, spatio-temporal phenomena in systems with large delay can take place on a very slow timescale and require in an efficient way to deal with large amounts of data representing the solutions history. Up to date this was not achieved by the other DDE-solvers known to the authors. ODDtool has been used for simulations in the papers [185, 186, 187, 188, 56].

The header `ODDtool.h` provides an interface for the integration of delay differential equations with constant point delays. The class which implements the integration is called `ODD_integrator<CKStepper>` and possesses a method `integrate()` which generates solution data and writes it to output files.

The template parameter `CKStepper` denotes a class which implements the actual computation of integration steps. We have implemented Cash-Karp method [189] (the variation of 4-5 order embedded Runge-Kutta scheme) with adaptive time stepping via controlling the error between 4th and 5th order integration. The values of delayed variables are interpolated with 5th order Hermite polynomials [190].

Different integration and interpolation methods can be added by implementing different stepper and interpolator classes (which should be derived from the abstract class `ODD_Stepper` and `ODD_Interpolator`). This template design is inspired from the `Odeint` class, see [191, 192].

The following instructions assume that you are working on a Unix system with gcc4.9 or higher and the `boost` libraries installed[1]. Some extra adjustments may be needed to run the tool on different configuration.

7.2. Usage

Providing the right hand side

To use the integrator, you include the header `ODDtool.h` and provide the right hand side of the equation

$$\dot{x}(t) = f(p; t, x(t), x(t-\tau_1), ..., x(t-\tau_{n_\tau})) \in \mathbb{R}^N, \tag{7.2.1}$$

you wish to integrate. Here, the vector $p \in \mathbb{R}^{n_p}$ contains the system parameters, $t \in \mathbb{R}$ is a scalar value of the time, and $x(t-\tau_j) \in \mathbb{R}^N$ is the system state at time $t-\tau_j$. The function f must be implemented as a `C++` function with the following signature:

```
void f(double, const vector<double>&, ODD_delayed_values&, const
vector<double>&, vector<double>&)
```

Here, the type `ODD_delayed_values` is a data structure which contains the needed values $x_i(t-\tau_j)$. From an object `xd` of this type the value $x_i(t-\tau_j)$ is retrieved by the expression `xd[j][i]` (note that i and j are reversed in some sense). A call to `f(t, x, xd, p, result)` writes the value of f(`p;t,x,xd[0],...,xd[`n_τ`]`) to the vector `result`.

For instance, if you wish to integrate two delay-coupled Mackey-Glass systems

$$\dot{x}_1(t) = \frac{\sigma x_2(t-\tau)}{1+x_2(t-\tau)^n} - \gamma x_1(t), \tag{7.2.2}$$

$$\dot{x}_2(t) = \frac{\sigma x_1(t-\tau)}{1+x_1(t-\tau)^n} - \gamma x_2(t), \tag{7.2.3}$$

you could implement the right hand side function as:

```
void f(double t,...,vector<double>& result) {
   result[0] = p[0] * xd[0][1] / (1 + pow(xd[0][1], p[1]))
   - p[2] * x[0]; // (7.2.2)
   result[1] = p[0] * xd[0][0] / (1 + pow(xd[0][0], p[1]))
   - p[2] * x[1]; // (7.2.3)
}
```

where the parameters are σ =`p[0]`, n =`p[1]` and γ =`p[2]`, and the delayed terms are $x_1(t-\tau)$ =`xd[0][0]` and $x_2(t-\tau)$ =`xd[0][1]`.

[1]The appropriate boost library linking in the `Makefile` should be checked.

Providing parameters and delays

The parameters $p = (p_1, ..., p_{n_p})$ and the delays $\tau_1, ...\tau_{n_\tau}$ in (7.2.1) are specified in the parameter file `ODD_parameters.txt`. In this file, the user can as well control various parameters to the integration procedure such as starting time and ending time, desired tolerance, minimal and maximal stepwidth, etc. – see the file `ODD_default_parameters.txt` for further documentation. If a parameter is not provided by the user in `ODD_parameters.txt`, a default value specified in `ODD_default_parameters.txt` is used. The latter file should not be modified by the user.

To make the above example (7.2.2) and (7.2.3) work, assuming $\sigma = 2.2$, $n = 10$, $\gamma = 1$, $\tau = 20$, and that one wishes to integrate for $t \in [0, 100]$, the parameter file should contain the following lines:

```
N = 2
name = TwoMackeyGlass
p0 = 2.2
p1 = 10
p2 = 1
tau0 = 20
t_start = 0
t_end = 100
```

Here, the specification of the system's name is optional. However, it will influence the naming of the output files. The default value is `name = noname`.

Providing an initial history

The initial data for (7.2.1) can be provided in two ways. Either you define a function `hist(double t, vector<double>& result)` within the program similarly as you do for the right hand side function `f(...)`. For each t it should assign the value of the initial function to the vector `result`.

A second way to provide the history function is to store it in a table containing time points, the corresponding states of the system and the corresponding derivatives of the function. (The derivatives are required until a higher order Newton interpolation is implemented.) If you provide only one time point, the program treats the corresponding state point as a constant initial function (derivatives are not required in this case). The table of initial data can be provided in two ways: in separate files or in a single file. This is done via the parameter file `ODD_parameters.txt` by adding either a line

```
history_file = name_of_some_file.txt
```

or adding the lines

```
history_t_file = name_of_some_file.txt
history_x_file = name_of_some_other_file.txt
history_f_file = name_of_some_another_file.txt
```

In both cases each row corresponds to one time point, different components are separated by spaces. If all data is contained in a single file, one row should look like this:

$$\underbrace{992.88}_{t}\ \underbrace{5.10\ 8.74}_{x}\ \underbrace{71.69\ -21.91}_{f}$$

Building a program using `ODDtool`

If you wish to integrate the example above, you have to prepare the parameter file `ODD_parameters.txt`, and a file `main.cpp`, which includes `ODDtool.h` and contains (or includes) the definition of your right hand side function and the method `main()`, which constructs an instance of `ODD_integrator<CKStepper>` and calls `integrate()`. Further, you may want to include an explicit definition of a history function. Otherwise, you must provide files containing information about the history. The `C++` file might look like this:

```
// file main.cpp
#include "ODDtool.h"
using namespace std;

// user-supplied history function
void myHistory(double t, vector<double>& result) {
   result[0] = abs(cos(t)) + 1;
   result[1] = 1 + sin(t);
}

// Two coupled Mackey-Glass systems
void MG2Rhs(double t, const vector<double>& x, ODD_delayed_values&
xd, const vector<double>& p, vector<double>& result) {
   result[0] = p[0] * xd[0][1] / (1 + pow(xd[0][1], p[1]))
   - p[2] * x[0];
   result[1] = p[0] * xd[0][0] / (1 + pow(xd[0][0], p[1]))
   - p[2] * x[1];
}

int main() {
   // create an integrator
   ODD_integrator<CKStepper> integrator(MG2Rhs, myHistory);
   // start integration over time interval specified in parameter
   file (ODD_parameters.txt)
   integrator.integrate();
}
```

If you don't want to specify the history explicitly but prefer to provide it in a file, you can simply drop the corresponding argument in the constructor for the integrator and type instead:

```
ODD_integrator<CKStepper> integrator(MG2Rhs);
```

Finally, you compile an executable. To this end you copy your files to the base directory of a copy of oddtool and you type `make` to the command line. This should compile the executable `oddtool` in this directory. When you run the executable by typing `./oddtool`, files are created which contain the calculated solution.

Output

The output files generated by ODDtool are named `t.txt` (time steps), `x.txt` (solution file) and, optionally, `f.txt` (right hand side). They are contained in the local directory `system_name_data/`, if the system's name is specified as `name = system_name` in the file `ODD_parameters.txt`. Moreover, `integrate()` generates the files `system_name_temp/continuation_*.txt` containing information necessary to resume the integration from the last calculated point.

7.3. Application to partial differential equations with delay

In this Thesis, ODDTool package was used to simulate the partial differential equations with large delay. The package was shown to be reliable for such kind of problems, with sufficient computational speed and decent memory use. In the case of PDE, the spatial variable was discretized and periodic boundary conditions were introduced.

The initial function on the delay interval is given be discretization of the profile found either by the solution of the boundary value problem, previous simulation, or manually defined function (for example, one can use Gaussian as initial function for relaxation to a stable localized structure).

In this case, the definition of right hand side in the `main.cpp` file could look like the following:

```
// RHS for the PDE with delay (laser with saturable absorber)
void LK2delaysRhs(double t, const std::vector<double>& x,
ODD_delayed_values& xd, const std::vector<double>& p,
std::vector<double>& result) {

   double b1 = p[0]; double b2 = p[1]; double g0 = p[2];
   double a0 = p[3]; double Ig = p[4];
   int m = 400; int N = m*2; double L = 50.0;
   double dL = double(L/(m-1)); int i = 0;

   //Left BC (periodic)
   //Nonlinear term
   A = -1.0 + g0/(1.0+(x[0]*x[0]+x[1]*x[1])/Ig)
```

```
   - a0/(1.0+(x[0]*x[0]+x[1]*x[1]));

   result[0] = b1*(x[N-2]-2.0*x[0]+x[2])/(dL*dL)
   - b2*(x[N-1]-2.0*x[1]+x[3])/(dL*dL)
   + A*x[0] + eta*(cos(phi)*xd[0][0]-sin(phi)*xd[0][1]);
   result[1] = b2*(x[N-2]-2.0*x[0]+x[2])/(dL*dL)
   + b1*(x[N-1]-2.0*x[1]+x[3])/(dL*dL)
   + A*x[1] + eta*(cos(phi)*xd[0][1]+sin(phi)*xd[0][0]);

   for (i=2;i<N-2;i+=2) {
   A = -1.0 + g0/(1.0+(x[i]*x[i]+x[i+1]*x[i+1])/Ig)
   - a0/(1.0+(x[i]*x[i]+x[i+1]*x[i+1]));

   result[i] = b1*(x[i-2]-2.0*x[i]+x[i+2])/(dL*dL)
   - b2*(x[i-1]-2.0*x[i+1]+x[i+3])/(dL*dL)
   + A*x[i] + eta*(cos(phi)*xd[0][i]-sin(phi)*xd[0][i+1]);
   result[i+1] = b2*(x[i-2]-2.0*x[i]+x[i+2])/(dL*dL)
   + b1*(x[i-1]-2.0*x[i+1]+x[i+3])/(dL*dL)
   + A*x[i+1] + eta*(cos(phi)*xd[0][i+1]+sin(phi)*xd[0][i]);
   }

   // Right BC (periodic)
   A = -1.0 + g0/(1.0+(x[N-2]*x[N-2]+x[N-1]*x[N-1])/Ig)
   - a0/(1.0+(x[N-2]*x[N-2]+x[N-1]*x[N-1]));

   result[N-2] = b1*(x[N-4]-2.0*x[N-2]+x[0])/(dL*dL)
   - b2*(x[N-3]-2.0*x[N-1]+x[1])/(dL*dL)
   + A*x[N-2] + eta*(cos(phi)*xd[0][N-2]-sin(phi)*xd[0][N-1]);
   result[N-1] = b2*(x[N-4]-2.0*x[N-2]+x[0])/(dL*dL)
   + b1*(x[N-3]-2.0*x[N-1]+x[1])/(dL*dL)
   + A*x[N-1] + eta*(cos(phi)*xd[0][N-1]+sin(phi)*xd[0][N-2]);
}
```

The amount of RAM on ordinary PC was proven to be sufficient to integrate the one-dimensional PDE on sufficient space interval with large values of delay time (i.e. thousands of rotation period in case of CGLE). With the use of spectral methods, higher-dimensional PDEs can be integrated as well.

Appendix B: Additional theorems

8.4. Closed Range Theorem

To prove the Fredholm alternative for functional PDEs in Chapter 2, the following *Closed Range Theorem* (S. Banach, [193, 84, 85]) is used:

THEOREM 10. *(Closed Range Theorem). Let X and Y be Banach spaces, linear operator $T : X \to Y$ be closed with* $\mathrm{Dom}(T) \in X$ *dense in X. The dual spaces for X and Y are X' and Y' correspondingly and $T' : Y' \to X'$ is the dual operator of T. The kernel or null space of linear operator is defined by $N(T) = \{x \in X : Tx = 0\}$ and the range is $R(T) = \{Tx : x \in X\}$. Additionally, we denote $\langle x, x' \rangle = x'(x)$ for $x \in X$ and $x' \in X'$. Then the following propositions are equivalent:*

1.) *$R(T)$, the range of T, is closed in Y,*

2.) *$R(T')$, the range of T', is closed in X',*

3.) *$R(T) = N(T')^{\perp} = \{y \in Y : \langle x', y \rangle = 0$ for all $x' \in N(T')\}$,*

4.) *$R(T') = N(T)^{\perp} = \{x' \in X' : \langle x', y \rangle = 0$ for all $y \in N(T)\}$.*

8.5. Solvability condition for delay differential equations with periodic coefficients

Let us consider a non-homogeneous linear DDE in the form

$$\dot{x}(t) = A(t)\,x(t) + B(t)\,x(t-\tau) + f(t), \tag{8.5.1}$$

for $x(t), f(t) \in \mathbb{R}^n$, where matrices $A(t), B(t)$ and function $f(t)$ are continuous and periodic with period $\omega > \tau$.

The correspondent homogeneous system is

$$\dot{x}(t) = A(t)\,x(t) + B(t)\,x(t-\tau), \tag{8.5.2}$$

and the adjoint equation reads

$$\dot{y}(t) = -A^T(t)\,y - B^T(t+\tau)\,y(t+\tau). \tag{8.5.3}$$

The following Theorem [28] gives the solvability condition for system (8.5.1):

THEOREM 11. *(Solvability condition for DDE with periodic coefficients). If system (8.5.1) has periodic solutions of period ω, then $(y, f) = \int_0^{\omega} y(t) f(t) dt = 0$ for all periodic solution $y(t)$ of period ω of the adjoint system (8.5.3).*

Bibliography

[1] M. Cross and H. Greenside, *Pattern formation and Dynamics in nonequilibrium systems*, Cambridge Univ. Press, 2009.

[2] P. Ball, *The Self-Made Tapestry: Pattern Formation in Nature*, Oxford University Press, 2001.

[3] J. Kelso, *Dynamic Patterns: The Self-organization of Brain and Behavior*, A Bradford book, MIT Press, 1995.

[4] A. M. Turing, "The chemical basis of morphogenesis," *Philosophical Transactions of the Royal Society of London B: Biological Sciences* **237**(641), pp. 37–72, 1952.

[5] I. Prigogine and R. Lefever, "Symmetry breaking instabilities in dissipative systems. II," *The Journal of Chemical Physics* **48**(4), pp. 1695–1700, 1968.

[6] L. Debnath, *Nonlinear Partial Differential Equations for Scientists and Engineers*, Birkhäuser Boston, 2010.

[7] L. Caffarelli, F. Golse, Y. Guo, C. Kenig, A. Vasseur, X. Cabré, and J. Soler, *Nonlinear Partial Differential Equations*, Advanced Courses in Mathematics - CRM Barcelona, Springer Basel, 2012.

[8] L. Evans, *Partial Differential Equations*, Graduate studies in mathematics, American Mathematical Society, 2010.

[9] S. Bianchini, E. Carlen, A. Mielke, and C. Villani, *Nonlinear PDE's and Applications: C.I.M.E. Summer School, Cetraro, Italy 2008, Editors: Luigi Ambrosio, Giuseppe Savaré*, Lecture Notes in Mathematics, Springer Berlin Heidelberg, 2011.

[10] J. Russell, *Report on Waves: Made to the Meetings of the British Association in 1842-43*, 1845.

[11] D. D. J. Korteweg and D. G. de Vries, "XLI. on the change of form of long waves advancing in a rectangular canal, and on a new type of long stationary waves," *Philosophical Magazine* **39**(240), pp. 422–443, 1895.

[12] N. Akhmediev and A. Ankiewicz, *Dissipative Solitons: From Optics to Biology and Medicine*, vol. 751 of *Lecture Notes in Physics*, Springer Berlin / Heidelberg, 2008.

[13] H.-G. Purwins, H. U. Bödeker, and S. Amiranashvili, "Dissipative solitons," *Adv. in Phys.* **59**(5), pp. 485–701, 2010.

[14] A. W. Liehr, *Dissipative Solitons in Reaction Diffusion Systems. Mechanism, Dynamics, Interaction*, Springer Berlin/Heidelberg, 2013.

[15] C. Christov and M. Velarde, "Dissipative solitons," *Physica D: Nonlinear Phenomena* **86**(1), pp. 323 – 347, 1995. Chaos, Order and Patterns: Aspects of Nonlinearity - @'The Gran Finale@'.

[16] B. Kerner and V. Osipov, *Autosolitons: A New Approach to Problems of Self-Organization and Turbulence*, Fundamental Theories of Physics, Springer Netherlands, 2013.

[17] O. Lioubashevski, Y. Hamiel, A. Agnon, Z. Reches, and J. Fineberg, "Oscillons and propagating solitary waves in a vertically vibrated colloidal suspension," *Phys. Rev. Lett.* **83**, pp. 3190–3193, 1999.

[18] A. S. Mikhailov and K. Showalter, "Control of waves, patterns and turbulence in chemical systems," *Physics Reports* **425**(2-3), pp. 79 – 194, 2006.

[19] S. Barland, S. Coen, M. Erkintalo, M. Giudici, J. Javaloyes, and S. Murdoch, "Temporal localized structures in optical resonators," *Advances in Physics: X* **2**(3), pp. 496–517, 2017.

[20] C. Huygens and R. J. Blackwell, *Christiaan Huygens' the pendulum clock, or, Geometrical demonstrations concerning the motion of pendula as applied to clocks*, Iowa State University Press, Ames, 1986. xxxii, 182 p.

[21] M. Bennett, M. F. Schatz, H. Rockwood, and K. Wiesenfeld, "Huygens's clocks," *Proceedings of the Royal Society of London A: Mathematical, Physical and Engineering Sciences* **458**(2019), pp. 563–579, 2002.

[22] M. Kapitaniak, K. Czolczynski, P. Perlikowski, A. Stefanski, and T. Kapitaniak, "Synchronization of clocks," *Physics Reports* **517**(1), pp. 1 – 69, 2012. Synchronization of clocks.

[23] A. Pikovsky, M. Rosenblum, and J. Kurths, *Synchronization: A Universal Concept in Nonlinear Sciences*, Cambridge nonlinear science series, Cambridge University Press, 2001.

[24] Y. Kuramoto and D. Battogtokh, "Coexistence of coherence and incoherence in nonlocally coupled phase oscillators," *Nonlinear Phenom. Complex Syst.* **5**, p. 2002, 2002.

[25] D. M. Abrams and S. H. Strogatz, "Chimera states for coupled oscillators," *Phys. Rev. Lett.* **93**, p. 174102, 2004.

[26] E. Schmidt, "Über eine Klasse linearer funktionaler Differentialgleichungen," *Mathematische Annalen* **70**, pp. 499–524, 1911.

[27] J. Hale, *History of Delay Equations*, pp. 1–28. Springer Netherlands, Dordrecht, 2006.

[28] A. Halanay, *Differential Equations: Stability, Oscillations, Time Lags*, Mathematics in science and engineering, Academic Press, 1966.

[29] V. Kolmanovskii and A. Myshkis, *Introduction to the Theory and Applications of Functional Differential Equations*, Mathematics and Its Applications, Springer Netherlands, 1999.

[30] E. Schöll and H. Schuster, *Handbook of Chaos Control*, Wiley, 2008.

[31] S. A. Kashchenko, "The Ginzburg-Landau equation as the normal form for a second-order difference-differential equation with a large delay," *Computational Mathematics and Mathematical Physics* **38**, pp. 443–451, 1998.

[32] G. Giacomelli and A. Politi, "Relationship between delayed and spatially extended dynamical systems," *Phys. Rev. Lett.* **76**(15), pp. 2686–2689, 1996.

[33] S. Yanchuk and G. Giacomelli, "Spatio-temporal phenomena in complex systems with time delays," *Journal of Physics A: Mathematical and Theoretical* **50**(10), p. 103001, 2017.

[34] J. Hale and S. Lunel, *Introduction to Functional Differential Equations*, no. v. 99 in Applied mathematical sciences, Springer-Verlag, 1993.

[35] J.-P. Richard, "Time-delay systems: An overview of some recent advances and open problems," *Automatica* **39**, pp. 1667–1694, 2003.

[36] F. Atay, *Complex Time-Delay Systems: Theory and Applications*, Understanding Complex Systems, Springer Berlin Heidelberg, 2010.

[37] T. Erneux, J. Javaloyes, M. Wolfrum, and S. Yanchuk, "Introduction to focus issue: Time-delay dynamics," *Chaos: An Interdisciplinary Journal of Nonlinear Science* **27**(11), p. 114201, 2017.

[38] V. A. K. V. D. Goryachenko, S. L. Zolotarev, *Investigations of Nuclear Reactors Dynamics by Qualitative Methods*, Energoatomizdat, Moscow, 1988.

[39] J. Ruan, L. Li, and W. Lin, "Dynamics of some neural network models with delay," *Phys. Rev. E* **63**, p. 051906, 2001.

[40] M. C. Soriano, J. García-Ojalvo, C. R. Mirasso, and I. Fischer, "Complex photonics: Dynamics and applications of delay-coupled semiconductors lasers," *Rev. Mod. Phys.* **85**, pp. 421–470, 2013.

[41] Y. Kuang, *Delay Differential Equations: With Applications in Population Dynamics*, Mathematics in Science and Engineering, Elsevier Science, 1993.

[42] O. V. Popovych, S. Yanchuk, and P. A. Tass, "Delay- and coupling-induced firing patterns in oscillatory neural loops," *Phys. Rev. Lett.* **107**, p. 228102, 2011.

[43] M. Arriojas, Y. Hu, S.-E. Mohammed, and G. Pap, "A delayed Black and Scholes formula," *Stochastic Analysis and Applications* **25**(2), pp. 471–492, 2007.

[44] L. Appeltant, M. C. Soriano, G. Van der Sande, J. Danckaert, S. Massar, J. Dambre, B. Schrauwen, C. R. Mirasso, and I. Fischer, "Information processing using a single dynamical node as complex system," *Nature Commun.* **2**, p. 468, 2011. Article.

[45] L. Larger, A. Baylón-Fuentes, R. Martinenghi, V. S. Udaltsov, Y. K. Chembo, and M. Jacquot, "High-speed photonic reservoir computing using a time-delay-based architecture: Million words per second classification," *Phys. Rev. X* **7**, p. 011015, 2017.

[46] T. Dahms, P. Hövel, and E. Schöll, "Control of unstable steady states by extended time-delayed feedback," *Phys. Rev. E* **76**, p. 056201, 2007.

[47] P. Hövel and E. Schöll, "Control of unstable steady states by time-delayed feedback methods," *Phys. Rev. E* **72**, p. 046203, 2005.

[48] S. Schikora, P. Hövel, H.-J. Wünsche, E. Schöll, and F. Henneberger, "All-optical noninvasive control of unstable steady states in a semiconductor laser," *Phys. Rev. Lett.* **97**, p. 213902, 2006.

[49] B. Fiedler, V. Flunkert, M. Georgi, P. Hövel, and E. Schöll, "Refuting the odd-number limitation of time-delayed feedback control," *Phys. Rev. Lett.* **98**, p. 114101, 2007.

[50] B. Fiedler, S. Yanchuk, V. Flunkert, P. Hövel, H.-J. Wünsche, and E. Schöll, "Delay stabilization of rotating waves near fold bifurcation and application to all-optical control of a semiconductor laser," *Phys. Rev. E* **77**, p. 066207, 2008.

[51] Q. S. Li and H. X. Hu, "Pattern transitions induced by delay feedback," *The Journal of Chemical Physics* **127**(15), p. 154510, 2007.

[52] Y. N. Kyrychko, K. B. Blyuss, S. J. Hogan, and E. Schöll, "Control of spatiotemporal patterns in the gray–scott model," *Chaos: An Interdisciplinary Journal of Nonlinear Science* **19**(4), p. 043126, 2009.

[53] K. Pyragas, "Continuous control of chaos by self-controlling feedback," *Phys. Lett. A* **170**, p. 421, 1992.

[54] M. Bestehorn, E. V. Grigorieva, and S. A. Kaschenko, "Spatiotemporal structures in a model with delay and diffusion," *Phys. Rev. E* **70**, p. 026202, 2004.

[55] N. Akhmediev, B. Kibler, F. Baronio, M. Belic, W.-P. Zhong, Y. Zhang, W. Chang, J. M. Soto-Crespo, P. Vouzas, P. Grelu, C. Lecaplain, K. Hammani, S. Rica, A. Picozzi, M. Tlidi, K. Panajotov, A. Mussot, A. Bendahmane, P. Szriftgiser, G. Genty, J. Dudley, A. Kudlinski, A. Demircan, U. Morgner, S. Amiraranashvili, C. Bree, G. Steinmeyer, C. Masoller, N. G. R. Broderick, A. F. J. Runge, M. Erkintalo, S. Residori, U. Bortolozzo, F. T. Arecchi, S. Wabnitz, C. G. Tiofack, S. Coulibaly, and M. Taki, "Roadmap on optical rogue waves and extreme events," *Journal of Optics* **18**(6), p. 063001, 2016.

[56] M. Kantner, E. Schöll, and S. Yanchuk, "Delay-induced patterns in a two-dimensional lattice of coupled oscillators," **5**, p. 8522, 2015. Article.

[57] S. Heiligenthal, T. Dahms, S. Yanchuk, T. Jüngling, V. Flunkert, I. Kanter, E. Schöll, and W. Kinzel, "Strong and weak chaos in nonlinear networks with time-delayed couplings," *Phys. Rev. Lett.* **107**, p. 234102, 2011.

[58] L. Larger, B. Penkovsky, and Y. Maistrenko, "Virtual chimera states for delayed-feedback systems," *Phys. Rev. Lett.* **111**, p. 054103, 2013.

[59] A. Gjurchinovski, E. Schöll, and A. Zakharova, "Control of amplitude chimeras by time delay in oscillator networks," *Phys. Rev. E* **95**, p. 042218, 2017.

[60] S. V. Gurevich and R. Friedrich, "Instabilities of localized structures in dissipative systems with delayed feedback," *Phys. Rev. Lett.* **110**, p. 014101, 2013.

[61] L. Lugiato, F. Prati, and M. Brambilla, *Nonlinear Optical Systems*, Cambridge University Press, 2015.

[62] Y. Tanguy, T. Ackemann, and R. Jäger, "Characteristics of bistable localized emission states in broad-area vertical-cavity surface-emitting lasers with frequency-selective feedback," *Phys. Rev. A* **74**, p. 053824, 2006.

[63] M. Lichtner, V. Z. Tronciu, and A. G. Vladimirov, "Theoretical investigations of striped and non-striped broad area lasers with off-axis feedback," *IEEE J. Quant. Electron.* **48**, pp. 353–360, 2012.

[64] J. Wu, *Theory and Applications of Partial Functional Differential Equations*, Applied Mathematical Sciences, Springer New York, 1996.
[65] S. Guo and J. Wu, *Bifurcation Theory of Functional Differential Equations*, Applied Mathematical Sciences, Springer New York, 2013.
[66] A. C. Newell, *Nonlinear Wave Motion*, ch. Envelope Equations, pp. 157–163. American Mathematical Society, Providence, Rhode Island, 1974.
[67] A. Mielke, "The Ginzburg-Landau equation in its role as a modulation equation," in *Handbook of dynamical systems, Vol. 2*, pp. 759–834, North-Holland, Amsterdam, 2002.
[68] V. V. Afanasjev, N. N. Akhmediev, and J. M. Soto-Crespo, "Three forms of localized solutions of the quintic complex Ginzburg-Landau equation," *Physical Review E* **53**(2), pp. 1931 – 1939, 1996.
[69] C. C. Travis and G. F. Webb, "Existence and stability for partial functional differential equations," *Trans. Amer. Math. Soc.* **200**, pp. 395–418, 1974.
[70] I. Segal, "Non-linear semi-groups," *Annals of Mathematics* **78**(2), pp. 339–364, 1963.
[71] W. Fitzgibbon, "Semilinear functional differential equations in banach space," *Journal of Differential Equations* **29**(1), pp. 1 – 14, 1978.
[72] M. E. Parrott, "Linearized stability and irreducibility for a functional differential equation," *SIAM Journal on Mathematical Analysis* **23**(3), pp. 649–661, 1992.
[73] F. E. Browder, "Non-linear equations of evolution," *Annals of Mathematics* **80**(3), pp. 485–523, 1964.
[74] H. R. Henríquez, "Regularity of solutions of abstract retarded functional differential equations with unbounded delay," *Nonlinear Analysis: Theory, Methods & Applications* **28**(3), pp. 513 – 531, 1997.
[75] S. G. Ruan and J. Wu, "Reaction-diffusion equations with infinite delay," *Canad. Appl. Math. Quart* **2**(4), pp. 485–550, 1994.
[76] M. Wolfrum, S. Yanchuk, P. Hövel, and E. Schöll, "Complex dynamics in delay-differential equations with large delay," *Eur. Phys. J. Special Topics* **191**, pp. 91–103, 2010.
[77] M. Lichtner, M. Wolfrum, and S. Yanchuk, "The spectrum of delay differential equations with large delay," *SIAM J. Math. Anal.* **43**, pp. 788–802, 2011.
[78] J. Sieber, M. Wolfrum, M. Lichtner, and S. Yanchuk, "On the stability of periodic orbits in delay equations with large delay," *Discrete Contin. Dyn. Syst. A* **33**, pp. 3109–3134, 2013.
[79] S. Yanchuk and M. Wolfrum, "Instabilities of equilibria of delay-differential equations with large delay," *in Proceedings of the ENOC-2005, Eindhoven, Netherlands, 7-12 August* , 2005.
[80] R. M. Corless, G. H. Gonnet, D. E. G. Hare, D. J. Jeffrey, and D. E. Knuth, "On the Lambert W function," *Advances in Computational Mathematics* **5**, pp. 329–359, 1996.
[81] D. Turaev, A. G. Vladimirov, and S. Zelik, "Chaotic bound state of localized structures in the complex Ginzburg-Landau equation," *Phys. Rev. E* **75**,

p. 045601, 2007.
[82] A. G. Vladimirov, G. V. Khodova, and N. N. Rosanov, "Stable bound states of one-dimensional autosolitons in a bistable laser," *Phys. Rev. E* **63**, p. 056607, 2001.
[83] R. M. Arkhipov, T. Habruseva, A. Pimenov, M. Radziunas, S. P. Hegarty, G. Huyet, and A. G. Vladimirov, "Semiconductor mode-locked lasers with coherent dual-mode optical injection: simulations, analysis, and experiment," *J. Opt. Soc. Am. B* **33**, pp. 351–359, 2016.
[84] K. Yosida, *Functional analysis*, Diegrundlehren der mathematischen wissenschaften, Springer-Verlag, 1978.
[85] W. Rudin, *Functional Analysis*, International series in pure and applied mathematics, McGraw-Hill, 2006.
[86] M. C. Cross and P. C. Hohenberg, "Pattern formation outside of equilibrium," *Rev. Mod. Phys.* **65**, pp. 851–1112, 1993.
[87] I. S. Aranson and L. Kramer, "The world of the complex Ginzburg-Landau equation," *Rev. Mod. Phys.* **74**, pp. 99–143, 2002.
[88] J. M. Soto-Crespo, N. Akhmediev, and V. V. Afanasjev, "Stability of the pulselike solutions of the quintic complex Ginzburg-Landau equation," *J. Opt. Soc. Am. B.* **13**, pp. 1439–1449, 1996.
[89] N. Akhmediev, A. Ankiewicz, and J. M. Soto-Crespo, "Stable soliton pairs in optical transmission lines and fiber lasers," *J. Opt. Soc. America B* **15**, pp. 515–523, 1998.
[90] P. Grelu and N. Akhmediev, "Group interactions of dissipative solitons in a laser cavity: the case of 2+1," *Opt. Express* **12**, pp. 3184–3189, 2004.
[91] M. Matsumoto, H. Ikeda, T. Uda, and A. Hasegawa, "Stable soliton transmission in the system with nonlinear gain," *IEEE/OSA Journal of Lightwave Technology* **13**, pp. 658–665, 1995.
[92] A. G. Vladimirov, S. V. Fedorov, N. A. Kaliteevskii, G. V. Khodova, and N. N. Rosanov, "Numerical investigation of laser localized structures," *Journal of Optics B: Quantum & Semiclassical Optics* **1**, pp. 101–106, 1999.
[93] K. Staliunas, R. Herrero, and G. J. de Valcárcel, "Arresting soliton collapse in two-dimensional nonlinear Schrödinger systems via spatio-temporal modulation of the external potential," *Phys. Rev. A* **75**, p. 011604(R), 2007.
[94] O. Thual and S. Fauve, "Localized structures generated by subcritical instabilities," *J. Phys. (France)* **49**, pp. 1829–1833, 1988.
[95] Y. S. Kivshar and G. Agrawal, *Optical Solitons: From Fibers to Photonic Crystals*, Elsevier Science, 2003.
[96] M. Tlidi, A. Vladimirov, D. Pieroux, and D. Turaev, "Spontaneous motion of cavity solitons induced by a delayed feedback," *Phys. Rev. Lett.* **103**, p. 103904, 2009.
[97] W. v. Saarloos and P. C. Hohenberg, "Fronts, pulses, sources and sinks in generalized complex Ginzburg-Landau equations," *Physica D* **56**, pp. 303–367, 1992.
[98] W. Just, B. Fiedler, M. Georgi, V. Flunkert, P. Hövel, and E. Schöll, "Beyond the odd number limitation: A bifurcation analysis of time-delayed

feedback control," *Phys. Rev. E* **76**, p. 026210, 2007.

[99] H. Erzgräber and W. Just, "Global view on a nonlinear oscillator subject to time-delayed feedback control," *Physica D Nonlinear Phenomena* **238**, pp. 1680–1687, 2009.

[100] G. Brown, C. Postlethwaite, and M. Silber, "Time-delayed feedback control of unstable periodic orbits near a subcritical Hopf bifurcation," *Physica D: Nonlinear Phenomena* **240**, pp. 859–871, 2011.

[101] C. M. Postlethwaite, G. Brown, and M. Silber, "Feedback control of unstable periodic orbits in equivariant Hopf bifurcation problems," *Phil. Trans. Royal Soc. A* **371**(1999), p. 20120467, 2013.

[102] J. M. Soto-Crespo and L. Pesquera, "Analytical approximation of the soliton solutions of the quintic complex Ginzburg-Landau equation," *Phys. Rev. E* **56**(6), pp. 7288–7293, 1996.

[103] K. A. Montgomery and M. Silber, "Feedback control of traveling wave solutions of the complex Ginzburg-Landau equation," *Nonlinearity* **17**, pp. 2225–2248, 2004.

[104] C. M. Postlethwaite and M. Silber, "Spatial and temporal feedback control of traveling wave solutions of the two-dimensional complex Ginzburg-Landau equation," *Physica D: Nonlinear Phenomena* **236**, pp. 65–74, 2007.

[105] S. Yanchuk and M. Wolfrum, "A multiple time scale approach to the stability of external cavity modes in the Lang-Kobayashi system using the limit of large delay," *SIAM J. Appl. Dyn. Syst.* **9**, pp. 519–535, 2010.

[106] D. V. Ramana Reddy, A. Sen, and G. L. Johnston, "Dynamics of a limit cycle oscillator under time delayed linear and nonlinear feedbacks," *Physica D: Nonlinear Phenomena* **144**, pp. 335–357, 2000.

[107] G. Giacomelli, F. Marino, M. A. Zaks, and S. Yanchuk, "Coarsening in a bistable system with long-delayed feedback," *EPL (Europhysics Letters)* **99**, p. 58005, 2012.

[108] S. Yanchuk and P. Perlikowski, "Delay and periodicity," *Phys. Rev. E* **79**, p. 046221, 2009.

[109] J. Mørk, B. Tromborg, and J. Mark, "Chaos in semiconductor lasers with optical feedback: theory and experiment," *IEEE J. Quantum Electron.* **28**, pp. 93–108, 1992.

[110] T. Heil, I. Fischer, W. Elsäßer, and A. Gavrielides, "Dynamics of semiconductor lasers subject to delayed optical feedback: The short cavity regime," *Phys. Rev. Lett.* **87**, p. 243901, 2001.

[111] V. Rottschäfer and B. Krauskopf, "The ECM-backbone of the Lang-Kobayashi equations: A geometric picture," *Internat. J. Bifur. Chaos* **17**, pp. 1575–1588, 2007.

[112] K. Green, B. Krauskopf, F. Marten, and D. Lenstra, "Bifurcation analysis of a spatially extended laser with optical feedback," *SIAM Journal on Applied Dynamical Systems* **8**(1), pp. 222–252, 2009.

[113] P. V. Paulau, D. Gomila, T. Ackemann, N. A. Loiko, and W. J. Firth, "Self-localized structures in vertical-cavity surface-emitting lasers with external feedback," *Physical Review E* **78**(1), p. 016212, 2008.

[114] P. Nestler, E. Schöll, and F. Tröltzsch, "Optimization of nonlocal time-delayed feedback controllers," *Computational Optimization and Applications* **64**, pp. 265–294, 2016.

[115] N. N. Rosanov, *Spatial Hysteresis and Optical Patterns*, Springer, Berlin, 2002.

[116] H. Vahed, F. Prati, M. Turconi, S. Barland, and G. Tissoni, "Periodic and chaotic solitons in a semiconductor laser with saturable absorber," *Philosophical Transactions of the Royal Society of London A: Mathematical, Physical and Engineering Sciences* **372**(2027), 2014.

[117] M. G. Clerc, A. Petrossian, and S. Residori, "Bouncing localized structures in a liquid-crystal light-valve experiment," *Phys. Rev. E* **71**, p. 015205, 2005.

[118] F. Arecchi, S. Boccaletti, and P. Ramazza, "Pattern formation and competition in nonlinear optics," *Physics Reports* **318**(1-2), pp. 1–83, 1999.

[119] O. Lioubashevski, H. Arbell, and J. Fineberg, "Dissipative solitary states in driven surface waves," *Phys. Rev. Lett.* **76**, pp. 3959–3962, 1996.

[120] D. J. B. Lloyd, C. Gollwitzer, I. Rehberg, and R. Richter, "Homoclinic snaking near the surface instability of a polarisable fluid," *Journal of Fluid Mechanics* **783**, pp. 283–305, 2015.

[121] H. Rotermund, S. Jakubith, A. Von Oertzen, and G. Ertl, "Solitons in a surface reaction," *Phys. Rev. Lett.* **66**(23), pp. 3083–3086, 1991.

[122] M. Suzuki, T. Ohta, M. Mimura, and H. Sakaguchi, "Breathing and wiggling motions in three-species laterally inhibitory systems," *Phys. Rev. E* **52**, pp. 3645–3655, 1995.

[123] S. Barland, M. Giudici, G. Tissoni, J. R. Tredicce, M. Brambilla, L. Lugiato, F. Prati, S. Barbay, R. Kuszelewicz, T. Ackemann, W. J. Firth, and G.-L. Oppo, "Solitons in semiconductor microcavities," *Nature Photonics* **6**, p. 204, 2012.

[124] A. Pimenov, A. G. Vladimirov, S. V. Gurevich, K. Panajotov, G. Huyet, and M. Tlidi, "Delayed feedback control of self-mobile cavity solitons," *Phys. Rev. A* **88**, p. 053830, 2013.

[125] L. A. Lugiato and R. Lefever, "Spatial dissipative structures in passive optical systems," *Phys. Rev. Lett.* **58**, pp. 2209–2211, 1987.

[126] A. Suchkov, "Effect of inhomogeneities on operation regime of solid-state lasers," *Sov. Phys. JETP* **22**(5), p. 1026, 1966.

[127] A. Vladimirov, N. Rozanov, S. Fedorov, and G. Khodova, "Bifurcation analysis of laser autosolitons," *Quantum Electronics* **27(11)**, pp. 949–952, 1997.

[128] A. Vladimirov, N. Rozanov, S. Fedorov, and G. Khodova, "Stability analysis of laser autosolitons," *Quantum Electronics* **28(1)**, pp. 55–57, 1998.

[129] A. G. Vladimirov, S. V. Fedorov, N. A. Kaliteevskii, G. V. Khodova, and N. N. Rosanov, "Numerical investigation of laser localized structures," *Journal of Optics B: Quantum and Semiclassical Optics* **1**(1), p. 101, 1999.

[130] D. Puzyrev, S. Yanchuk, A. Vladimirov, and S. Gurevich, "Stability of plane wave solutions in complex Ginzburg–Landau equation with delayed feedback," *SIAM Journal on Applied Dynamical Systems* **13**(2), pp. 986–1009, 2014.

[131] T. Ackemann, Y. Noblet, P. Paulau, C. McIntyre, P. Colet, W. Firth, and G.-L. Oppo, "Frequency and phase locking of laser cavity solitons," in *Spontaneous Symmetry Breaking, Self-Trapping, and Josephson Oscillations*, B. A. Malomed, ed., *Progress in Optical Science and Photonics* **1**, pp. 49–87, Springer Berlin Heidelberg, 2013.

[132] Z. Wu and W. Michiels, "Reliably computing all characteristic roots of delay differential equations in a given right half plane using a spectral method," *Journal of Computational and Applied Mathematics* **236**(9), pp. 2499 – 2514, 2012.

[133] G. Iooss and D. Joseph, *Elementary Stability and Bifurcation Theory*, Undergraduate Texts in Mathematics, Springer New York, 2013.

[134] A. Luo and J. Sun, *Complex Systems: Fractionality, Time-delay and Synchronization*, Nonlinear Physical Science, Springer Berlin Heidelberg, 2011.

[135] P. V. Paulau, D. Gomila, P. Colet, M. A. Matías, N. A. Loiko, and W. J. Firth, "Drifting instabilities of cavity solitons in vertical-cavity surface-emitting lasers with frequency-selective feedback," *Phys. Rev. A* **80**, p. 023808, 2009.

[136] A. Scroggie, W. Firth, G. McDonald, M. Tlidi, R. Lefever, and L. Lugiato, "Pattern formation in a passive Kerr cavity," *Chaos, Solitons & Fractals* **4**(8), pp. 1323 – 1354, 1994. Special Issue: Nonlinear Optical Structures, Patterns, Chaos.

[137] W. J. Firth, G. K. Harkness, A. Lord, J. M. McSloy, D. Gomila, and P. Colet, "Dynamical properties of two-dimensional Kerr cavity solitons," *J. Opt. Soc. Am. B* **19**, pp. 747–752, 2002.

[138] F. Leo, S. Coen, P. Kockaert, S.-P. Gorza, P. Emplit, and M. Haelterman, "Temporal cavity solitons in one-dimensional Kerr media as bits in an all-optical buffer," *Nature Photonics* **4**(7), pp. 471–476, 2010.

[139] D. Turaev, A. G. Vladimirov, and S. Zelik, "Long-range interaction and synchronization of oscillating dissipative solitons," *Phys. Rev. Lett.* **108**, p. 263906, 2012.

[140] K. Panajotov and M. Tlidi, "Spontaneous motion of cavity solitons in vertical-cavity lasers subject to optical injection and to delayed feedback," *The European Physical Journal D* **59**, pp. 67–72, 2010.

[141] K. Panajotov and M. Tlidi, "Chaotic behavior of cavity solitons induced by time delay feedback," *Opt. Lett.* **39**, pp. 4739–4742, 2014.

[142] C. Godey, I. V. Balakireva, A. Coillet, and Y. K. Chembo, "Stability analysis of the spatiotemporal Lugiato-Lefever model for Kerr optical frequency combs in the anomalous and normal dispersion regimes," *Phys. Rev. A* **89**, p. 063814, 2014.

[143] P. Parra-Rivas, D. Gomila, M. A. Matías, S. Coen, and L. Gelens, "Dynamics of localized and patterned structures in the Lugiato-Lefever equation determine the stability and shape of optical frequency combs," *Phys. Rev. A* **89**, p. 043813, 2014.

[144] M. Tlidi, P. Mandel, and R. Lefever, "Localized structures and localized patterns in optical bistability," *Phys. Rev. Lett.* **73**, pp. 640–643, 1994.

[145] A. G. Vladimirov, J. M. McSloy, D. V. Skryabin, and W. J. Firth, "Two-dimensional clusters of solitary structures in driven optical cavities," *Phys. Rev. E* **65**, p. 046606, 2002.

[146] W. Chang, J. M. Soto-Crespo, P. Vouzas, and N. Akhmediev, "Spiny solitons and noise-like pulses," *J. Opt. Soc. Am. B* **32**, pp. 1377–1383, 2015.

[147] D. Puzyrev, A. G. Vladimirov, S. V. Gurevich, and S. Yanchuk, "Modulational instability and zigzagging of dissipative solitons induced by delayed feedback," *Phys. Rev. A* **93**, p. 041801, 2016.

[148] K. Panajotov, D. Puzyrev, A. G. Vladimirov, S. V. Gurevich, and M. Tlidi, "Impact of time-delayed feedback on spatiotemporal dynamics in the Lugiato-Lefever model," *Phys. Rev. A* **93**, p. 043835, 2016.

[149] D. Botez and D. R. Scifres, eds., *Diode Laser Arrays*, no. 14 in Cambridge Studies in Modern Optics, Cambridge University Press, 2008.

[150] A. F. Glova, "Phase locking of optically coupled lasers," *Quantum Electronics* **33**(4), p. 283, 2003.

[151] H. E. Hagemeier and S. R. Robinson, "Field properties of multiple coherently combined lasers," *Appl. Opt.* **18**, pp. 270–280, 1979.

[152] V. V. Likhanskii and A. P. Napartovich, "Radiation emitted by optically coupled lasers," *Soviet Physics Uspekhi* **33**(3), p. 228, 1990.

[153] R.-d. Li and T. Erneux, "Preferential instability in arrays of coupled lasers," *Phys. Rev. A* **46**, pp. 4252–4260, 1992.

[154] R.-d. Li and T. Erneux, "Bifurcation to standing and traveling waves in large arrays of coupled lasers," *Phys. Rev. A* **49**, pp. 1301–1312, 1994.

[155] G. Kozyreff, A. G. Vladimirov, and P. Mandel, "Global coupling with time delay in an array of semiconductor lasers," *Phys. Rev. Lett.* **85**, pp. 3809–3812, 2000.

[156] G. Kozyreff, A. G. Vladimirov, and P. Mandel, "Dynamics of a semiconductor laser array with delayed global coupling," *Physical Review E* **64**, p. 016613, 2001.

[157] A. Jechow, M. Lichtner, R. Menzel, M. Radziunas, D. Skoczowsky, and A. Vladimirov, "Stripe-array diode-laser in an off-axis external cavity: Theory and experiment," *Optics Express* **17**, pp. 19599–19604, 2009.

[158] S. Sivaramakrishnan and H. Winful, "Subharmonic anti-phase dynamics in coupled mode-locked semiconductor lasers," *Optics Letters* **42**, pp. 4905–4908, 2017.

[159] A. G. Vladimirov and D. Turaev, "Model for passive mode locking in semiconductor lasers," *Phys. Rev. A* **72**, p. 033808, 2005.

[160] M. Golubitsky, I. Stewart, and D. G. Schaeffer, *Singularities and Groups in Bifurcation Theory. Volume II*, vol. 69 of *Applied Mathematical Sciences*, Springer-Verlag, New-York, 1988.

[161] S. Yanchuk and M. Wolfrum, "Destabilization patterns in chains of coupled oscillators," *Phys. Rev. E* **77**(2), p. 026212, 2008.

[162] O. D'Huys, R. Vicente, T. Erneux, J. Danckaert, and I. Fischer, "Synchronization properties of network motifs: Influence of coupling delay and symmetry," *Chaos* **18**(3), p. 037116, 2008.

[163] L. M. Pecora and T. L. Carroll, "Master stability functions for synchronized coupled systems," *Physical Review Letters* **80**(10), p. 2109, 1998.
[164] L. M. Pecora and M. Barahona, "Synchronization of oscillators in complex networks," *Chaos and Complexity Letters* **1**(1), pp. 61–91, 2005.
[165] N. Rebrova, G. Huyet, D. Rachinskii, and A. G. Vladimirov, "Optically injected mode-locked laser," *Phys. Rev. E* **83**, p. 066202, 2011.
[166] B. A. Malomed, "Bound solitons in the nonlinear Schrödinger–Ginzburg-Landau equation," *Phys. Rev. A* **44**, pp. 6954–6957, 1991.
[167] V. V. Afanasjev, B. A. Malomed, and P. L. Chu, "Stability of bound states of pulses in the Ginzburg-Landau equations," *Phys. Rev. E* **56**, pp. 6020–6025, 1997.
[168] D. Puzyrev, A. G. Vladimirov, A. Pimenov, S. V. Gurevich, and S. Yanchuk, "Bound pulse trains in arrays of coupled spatially extended dynamical systems," *Phys. Rev. Lett.* **119**, p. 163901, 2017.
[169] K. Engelborghs, T. Luzyanina, and D. Roose, "Numerical bifurcation analysis of delay differential equations using DDE-BIFTOOL," *ACM Trans. Math. Softw.* **28**, pp. 1–21, 2002.
[170] N. Akhmediev and A. Ankiewicz, *Solitons, Nonlinear Pulses and Beams*, Chapman and Hall, London, 1997.
[171] P. Grelu and N. Akhmediev, "Dissipative solitons for mode-locked lasers," *Nature Photonics* **6**, pp. 84–92, 2012.
[172] P. Grelu, F. Belhache, F. Gutty, and J.-M. Soto-Crespo, "Phase-locked soliton pairs in a stretched-pulse fiber laser," *Opt. Lett.* **27**, pp. 966–968, 2002.
[173] D. Y. Tang, B. Zhao, D. Y. Shen, C. Lu, W. S. Man, and H. Y. Tam, "Bound-soliton fiber laser," *Phys. Rev. A* **66**, p. 033806, 2002.
[174] N. H. Seong and D. Y. Kim, "Experimental observation of stable bound solitons in a figure-eight fiber laser," *Opt. Lett.* **27**, pp. 1321–1323, 2002.
[175] L. M. Zhao, D. Y. Tang, X. Wu, D. J. Lei, and S. C. Wen, "Bound states of gain-guided solitons in a passively mode-locked fiber laser," *Opt. Lett.* **32**, pp. 3191–3193, 2007.
[176] J. H. Lin, C. W. Chan, H. Y. Lee, and Y. H. Chen, "Bound states of dispersion-managed solitons from single-mode Yb-doped fiber laser at net-normal dispersion," *IEEE Photonics Journal* **7**, pp. 1–9, 2015.
[177] A. Zavyalov, R. Iliew, O. Egorov, and F. Lederer, "Dissipative soliton molecules with independently evolving or flipping phases in mode-locked fiber lasers," *Phys. Rev. A* **80**, p. 043829, 2009.
[178] B. Ortaç, A. Zaviyalov, C. K. Nielsen, O. Egorov, R. Iliew, J. Limpert, F. Lederer, and A. Tünnermann, "Observation of soliton molecules with independently evolving phase in a mode-locked fiber laser," *Opt. Lett.* **35**, pp. 1578–1580, 2010.
[179] X. Wu, D. Tang, X. Luan, and Q. Zhang, "Bound states of solitons in a fiber laser mode locked with carbon nanotube saturable absorber," *Optics Communications* **284**(14), pp. 3615 – 3618, 2011.
[180] X. L. Li, S. M. Zhang, Y. C. Meng, Y. P. Hao, H. F. Li, J. Du, and Z. J. Yang, "Observation of soliton bound states in a graphene mode locked

erbium-doped fiber laser," *Laser Physics* **22**(4), pp. 774–777, 2012.
[181] L. Gui, X. Xiao, and C. Yang, "Observation of various bound solitons in a carbon-nanotube-based erbium fiber laser," *J. Opt. Soc. Am. B* **30**, pp. 158–164, 2013.
[182] V. Tsatourian, S. V. Sergeyev, C. Mou, A. Rozhin, V. Mikhailov, B. Rabin, P. S. Westbrook, and S. K. Turitsyn, "Polarisation dynamics of vector soliton molecules in mode locked fibre laser," *Scientific Reports* **3**, p. 3154, 2013.
[183] M. Nizette, D. Rachinskii, A. Vladimirov, and M. Wolfrum, "Pulse interaction via gain and loss dynamics in passive mode locking," *Physica D: Nonlinear Phenomena* **218**(1), pp. 95 – 104, 2006.
[184] P. Camelin, J. Javaloyes, M. Marconi, and M. Giudici, "Electrical addressing and temporal tweezing of localized pulses in passively-mode-locked semiconductor lasers," *Phys. Rev. A* **94**, p. 063854, 2016.
[185] S. Yanchuk, L. Lücken, M. Wolfrum, and A. Mielke, "Spectrum and amplitude equations for scalar delay-differential equations with large delay," *Discrete Contin. Dyn. Syst. A* **35**(1), pp. 537–553, 2015.
[186] V. Klinshov, L. Lücken, D. Shchapin, V. Nekorkin, and S. Yanchuk, "Multistable jittering in oscillators with pulsatile delayed feedback," *Phys. Rev. Lett.* **114**, p. 178103, 2015.
[187] S. Yanchuk and G. Giacomelli, "Pattern formation in systems with multiple delayed feedbacks," *Phys. Rev. Lett.* **112**, p. 174103, 2014.
[188] V. Klinshov, L. Lücken, D. Shchapin, V. Nekorkin, and S. Yanchuk, "Emergence and combinatorial accumulation of jittering regimes in spiking oscillators with delayed feedback," *Phys. Rev. E* **92**, p. 042914, 2015.
[189] J. R. Cash and A. H. Karp, "A variable order runge-kutta method for initial value problems with rapidly varying right-hand sides," *ACM Trans. Math. Softw.* **16**, pp. 201–222, 1990.
[190] F. Hildebrand, *Introduction to Numerical Analysis: Second Edition*, Dover Books on Mathematics, Dover Publications, 2013.
[191] B. Schäling, *The Boost C++ Libraries:*, XML Press, 2011.
[192] W. Press, *Numerical Recipes 3rd Edition: The Art of Scientific Computing*, Cambridge University Press, 2007.
[193] S. Banach and F. Jellett, *Theory of Linear Operations*, Dover Books on Mathematics Series, Dover Publications, 2009.

Selbständigkeitserklärung

Ich erkläre, dass ich die Dissertation selbständig und nur unter Verwendung der von mir gemäß § 7 Abs. 3 der Promotionsordnung der Mathematisch-Naturwissenschaftlichen Fakultät, veröffentlicht im Amtlichen Mitteilungsblatt der Humboldt-Universität zu Berlin Nr. 126/2014 am 18.11.2014 angegebenen Hilfsmittel angefertigt habe. Ich habe mich nicht anderwärts um einen Doktorgrad im Promotionsfach Mathematik beworben und besitze keinen Doktorgrad im Promotionsfach Mathematik. Die Promotionsordnung der Mathematisch-Naturwissenschaftlichen Fakultät, veröffentlicht im Amtlichen Mitteilungsblatt der Humboldt-Universität zu Berlin Nr. 126/2014 am 18.11.2014, habe ich zur Kenntnis genommen.

Dmitry Puzyrev

Berlin, den 7. Februar 2018